UC-25
LBL-16612
c.1

Lawrence Berkeley Laboratory

UNIVERSITY OF CALIFORNIA

Materials & Molecular Research Division

1 1983
LBL LIBRARY

PHASE TRANSFORMATIONS AND THE DEVELOPMENT OF MAGNETIC COERCIVITY IN SAMARIUM-COBALT BASED PERMANENT MAGNET ALLOYS

L.K. Rabenberg
(Ph.D. Thesis)

September 1983

For Reference

Not to be taken from this room

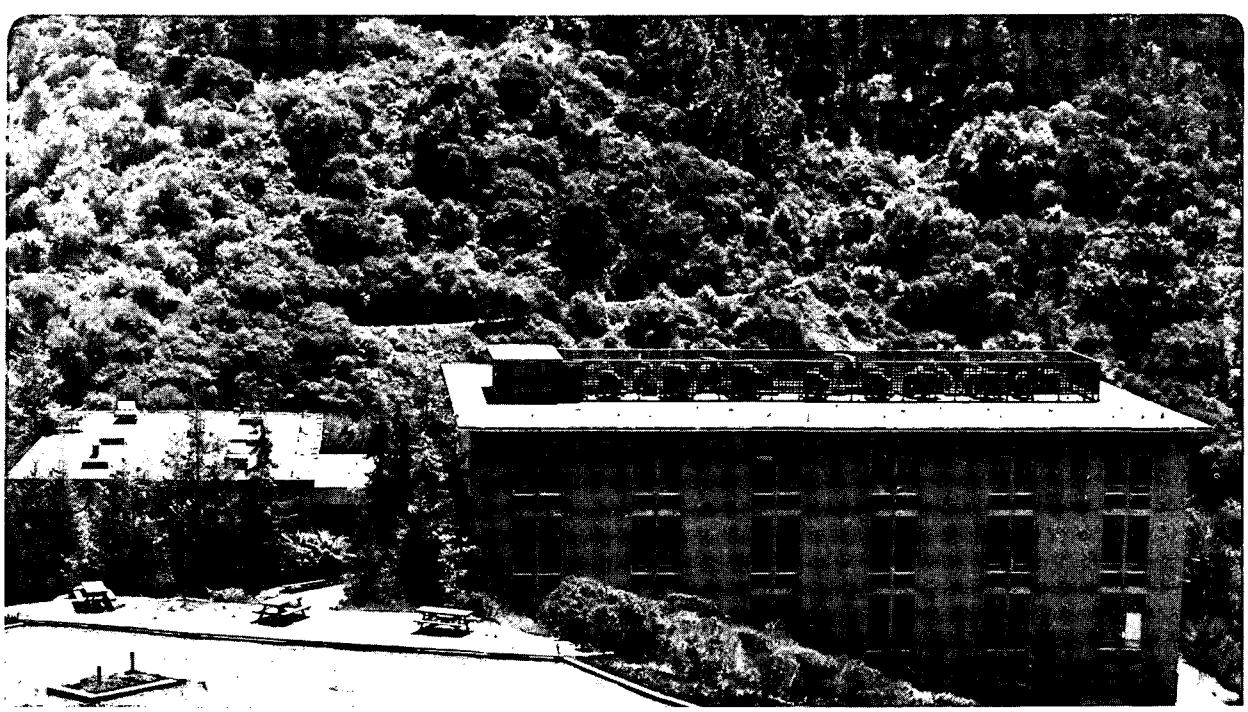

LBL-16612
c.1

Prepared for the U.S. Department of Energy under Contract DE-AC03-76SF00098

DISCLAIMER

This document was prepared as an account of work sponsored by the United States Government. While this document is believed to contain correct information, neither the United States Government nor any agency thereof, nor the Regents of the University of California, nor any of their employees, makes any warranty, express or implied, or assumes any legal responsibility for the accuracy, completeness, or usefulness of any information, apparatus, product, or process disclosed, or represents that its use would not infringe privately owned rights. Reference herein to any specific commercial product, process, or service by its trade name, trademark, manufacturer, or otherwise, does not necessarily constitute or imply its endorsement, recommendation, or favoring by the United States Government or any agency thereof, or the Regents of the University of California. The views and opinions of authors expressed herein do not necessarily state or reflect those of the United States Government or any agency thereof or the Regents of the University of California.

LBL-16612

PHASE TRANSFORMATIONS AND THE DEVELOPMENT OF MAGNETIC COERCIVITY IN SAMARIUM-COBALT BASED PERMANENT MAGNET ALLOYS

Llewellyn Kay Rabenberg
Ph.D. Thesis

Lawrence Berkeley Laboratory
University of California
Berkeley, California 94720

September 1983

TABLE OF CONTENTS

I.ABSTRACT

II.INTRODUCTION.....1

A.Opening Remarks.....1

B.Background Material.....5

1.Plan of Attack.....5

2.Rare Earth-Transition Metal Phases.....6

3.Crystallography.....8

4.Permanent Magnet Phases.....14

5.Anisotropy.....16

6.Microstructures.....18

7.Summary.....24

C.Aims and Approach.....25

III.EXPERIMENTAL.....29

A. Alloys.....29

B. Transmission Electron Microscopy and Microanalysis.....31

C. Specimen Preparation.....32

D. Microstructural Quantification.....34

IV.RESULTS.....37

A.Plan of Attack.....37

B.Macroscopic Magnetic Data.....38

C.Microstructures.....40

D.Microanalyses.....46

E.Comparisons and Correlations.....48

F.Origin of the Cellular Structure.....50

G.Origin of the Z Phase Plates.....57

H.Summary.....59

V.DISCUSSION.....61

A.Plan of Attack.....61

B.Microstructural Development.....62

1.Plan of Attack.....62

2.Nucleation of the Cellular Structure.....63

3.Growth of the Cellular Structure.....74

4.Nucleation and Growth of the Z Phase Plates..80

5.Twinning.....85

6.Redistribution of Transition Elements.....86

7.Summary.....91

C.Comparisons to Related Alloys.....92

1.Plan of Attack.....92

2.Variable Sm Content.....92

3.Variable Fe Content.....95

4.Variable Zr Content.....97

5.Summary.....98

D.Alloy Improvements.....99

1.Plan of Attack.....99

2.Coercivity Improvements.....99

3.Saturation Magnetization Improvements.....103

VI.SUMMARY.....106

VII.ACKNOWLEDGEMENTS.....110

VIII.REFERENCES.....112

IX.TABLES.....116

X.FIGURE CAPTIONS.....123

XI.FIGURES.....138

PHASE TRANSFORMATIONS AND THE DEVELOPMENT OF MAGNETIC COERCIVITY IN SAMARIUM-COBALT BASED PERMANENT MAGNET ALLOYS

Llewellyn Kay Rabenberg

Ph.D. Materials Science and Mineral Engineering Department

Gareth Thomas

Professor Gareth Thomas
Committee Chairman

This work was supported by the Director, Office of Energy Research, Office of Basic Energy Sciences, Materials Science Division of the U. S. Department of Energy under contract No. DE-AC-03-76SF00098 and by an Atlantic Richfield Foundation Fellowship.

ABSTRACT

An experimental investigation of the microstructures of precipitation-hardening samarium-cobalt based magnets has been undertaken in order to determine the nature of the

microstructural features critical for the development of high intrinsic coercivity in these permanent magnet alloys. In alloys aged near peak coercivity, three microstructural features are commonly observed. The bulk of the material consists of a modulated structure of twinned rhombohedral $Sm_2(CoCuFeZr)_{17}$ with thin layers of hexagonal $Sm(CoCuFeZr)_5$ developed on the six crystallographically equivalent pyramid planes. A Zr-rich phase having a structure related to that of $SmCo_3$ forms as thin, coherent plates on the basal planes of the modulated structure. The modulated structure results from precipitation of 1:5 from supersaturated solution in 2:17; this precipitation reaction occurs concurrently with an allotropic transformation of the parent 2:17 phase. The thin plates nucleate at interfaces in the modulated structure and grow by a Zr diffusion limited dislocation mechanism. Aging these alloys at temperatures high enough for diffusion of Sm through the lattice results in coarsening of the modulations. In order to develop the coercivity, a low temperature aging process must be performed to allow Cu and Fe to partition into the $Sm(CoCuFeZr)_5$ and the $Sm_2(CoCuFeZr)_{17}$ phases, respectively. This increases the differences in their respective magnetic domain wall energies, increasing the barrier to domain wall propagation, resulting in higher intrinsic coercivity. Thus, the results of this investigation imply that high intrinsic coercivity in two-phase SmCo based permanent magnet alloys will occur if the microstructure consists of a continuous, coherent two-phase dispersion with maximal chemical differentiation between the two phases.

INTRODUCTION

This thesis presents the results of an experimental investigation of the physical metallurgy of samarium-cobalt based permanent magnet alloys. SmCo magnets consist of a coherent dispersion of two crystallographically similar intermetallic compounds, both of which are noncubic, ferromagnetic, and highly anisotropic. The maximum magnetic coercivity of these alloys is limited by the ease of irreversible migration of ferromagnetic domain walls through the dispersion of the two intermetallic phases. The ease of migration in turn depends on the sizes, shapes, and overall distribution of the two phases. A fine-scale, coherent distribution of the two phases arises naturally as the result of phase transformations specific to the system. Thus, magnetic coercivity in this system depends most directly on those factors which influence growth patterns and the resulting sizes and shapes of the two phases, but less directly on the phase transformation which influence the distribution of the two phases.

Interest in samarium-cobalt alloys arises primarily from their outstanding permanent magnet characteristics. For the two-phase magnets considered in this investigation, energy product [$(BH)_{MAX}$] values exceeding 30 MGOe [1] have been obtained; the corresponding value for Alnico type magnets is approximately 8.5 MGOe [2]. Thus, for equal volumes of material, the SmCo magnet

stores 3.5 times as much energy in its magnetic fields. Technological interest and applications follow immmediately from this fact.

SmCo magnets represent an unusual metallurgical system; they are composed completely of intermetallic compounds. This is in contrast with the more conventional metallurgical systems which consist almost entirely of terminal solid solutions. The useful SmCo phases are noncubic and highly anisotropic; the resultant easy axis of magnetization is fundamental to the hard magnetic characteristics. Phase transformations in this system also have a directional character; substitutions and shear mechanisms are confined to a single crystallographic plane. Thus, SmCo is a member of an unconventional, and therefore poorly understood area of metallurgy; scientific interest in this system derives from that fact.

Rare earth-cobalt magnet science and technology has generally been approached in one of two ways. Industrial research and development has followed a largely trial-and-error approach, varying compositions and thermal treatments, always building on previous successes. This has led to many advances as the alloys have become increasingly complex; magnets having optimal $(BH)_{MAX}$ now are commonly four- or five-component systems composed of 2 or more phases. On the other hand, academic labs have generally followed the practice of synthesizing individual intermetallic compounds and recording the response of their magnetic parameters to variations in the levels of ternary substituents. Of particular interest is the development of magnetic anisotropy and how it is

influenced by lattice substitutions. The literature contains a great deal of information [3] about anisotropy and other characteristics of rare earth-cobalt based intermetallics with very few reports of which phases and compositions actually occur in useful magnets.

This investigation has followed an intermediate course, studying the interactions of phases and components in an industrial magnet system, remaining cognizant of the effects of composition on the properties of the individual intermetallic phases. The results of this investigation should serve to reconcile the somewhat disparate aspects of the same materials system. Rare earth-cobalt magnets are here treated as an interesting, if unconventional, metallurgical system.

This thesis itself is arranged following the pattern taken by the actual laboratory investigations. Rare earth permanent magnets are a mature technology, involving in practice, multicomponent, multiphase alloys and sophisticated thermal processing. A section of the introductory material involves a literature review of rare earth-cobalt crystallography and technology; this should serve to introduce the reader to the problem, establish the properties and crystallography of the various intermetallics, and in so doing, motivate the research reported in the later sections. The experimental results describe the microstructure and magnetic properties, especially intrinsic coercivity, and their response to thermal aging. The roles of the various components in the two- or three-phase structures are delineated; the magnetic coercivity is interpreted in terms of

the interaction of domain walls with the polyphase structures. The final area of experimental work establishes the nature of the phase transformations which are responsible for the useful, uniform, two-phase dispersion. The results of this investigation are strictly valid for these alloys and these phases, but similar transformation products are observed in related alloys; the results are probably more general - they have direct implications for technological advancement.

At this point, it is appropriate to add a few words about the scope and limitations of this thesis. First of all, samarium-cobalt is not a substance one would likely choose for a study of fundamental metallurgical phenomenon; one normally would choose a simpler, more familiar, easier-to-work-with system. SmCo is a technological system; while it exhibits phenomena of scientific interest, the motivation for study is essentially practical. This is reflected in this work; the results sought and reported here are the broad, if somewhat coarse, patterns of microstructure and phase transformations of an alloy system. Specifics, such as accurate values of kinetic data, lattice parameters, or even exact transformation temperatures for individual alloys will not appear here; these composition-dependent parameters may be important in actual production of specific alloys, but they are not necessary for an understanding of the overall behavior. Furthermore, the complexity of the alloys and their relative unfamiliarity preclude measurement of such data. However, one can and should be fairly detailed about crystallography; the patterns of microstructural development are fun-

damentally constrained by the crystal lattices. The crystallography is common to a wider class of alloys; it is the commonalities in crystallography which supports the idea that the results reported here are somewhat more general. Finally, even though these are magnetic alloys, no attempt will be made to tutor the reader on the physics of magnetism. A common knowledge of magnetism and the technical hysteresis loop will be assumed throughout.

Background Material.

It is the purpose of this section to introduce the reader, especially the technically-trained non-expert, to the subject of rare earth-cobalt permanent magnets. This is a subject which seems to involve many terms and concepts only rarely encountered elsewhere, if at all. For example, such terms as "dumbbell sites" or "rhombohedral two-seventeen" are not in the lexicons of the average metallurgist even though they are conceptually simple and basic to the present discussion. This presents special problems in presentation as these terms and others have to be redefined for each audience. Fortunately, in a tract of this magnitude, it is possible to take time to carefully introduce all the concepts so that subsequent discussion may proceed unhindered and with a minimum of confusion. It is hoped that this section will serve this purpose.

Many aspects of rare earth-cobalt science and technology

have been reviewed in the literature. The reader is urged to consult reviews by Gupta [4] on phase relationships, Wallace and Narasimhan [3] on magnetic properties and Asti and Deriu [5] and Wallace et al. [6] on magnetocrystalline anisotropy for a more nearly complete treatment. It is the purpose of this section to introduce the concepts; complete details will not appear here.

This section will be arranged in what seems to be a logical sequence, from general principles of rare earth-transition metal systems to specifics of practical magnet alloys. The first section will introduce the reader to the rare earth-transition metal intermetallic compounds and phase diagrams. Several phases occur in many RE-TM binaries which are important for permanent magnet applications; their structures and crystallography will be briefly outlined. The rationale for considering $SmCo_5$ and Sm_2Co_{17} as permanent magnets will appear, followed by a brief discussion of the effects of ternary additions to $SmCo_5$ and Sm_2Co_{17} on their magnetocrystalline anisotropy. Practical permanent magnets are structure-dependent; the final segment will give a literature review of microstructural studies of practical permanent magnets.

Rare Earth-Transition Metal Phases. Rare earth-cobalt magnets are formed of combinations of intermetallic compounds of stoichiometry $(RE)(TM)_5$ (denoted 1:5)* or $(RE)_2(TM)_{17}$ (denoted 2:17) [In this thesis, "1:5" and "2:17" will be used to denote intermetallics having these ratios of their rare earth to transition metal sites. That is, this form will be used in a general

sense to refer to simple binary compounds such as Sm_2Co_{17}, as well as more complicated phases involving substitutions of rare earths, transition metals, or both. For example, $Sm_2(CoCuFe)_{17}$, $(SmGd)_2Co_{17}$, and $(SmNd)_2(CoCuZr)_{17}$ could all be special cases of "2:17". Conversely, "$SmCo_5$" should be taken to mean binary samarium-cobalt$_5$] Here RE denotes one or more rare earth elements and TM denotes one or more transition metals of (usually) the first period of the periodic table viz. Cr, Mn, Fe... These two phases occur in the majority of the RE-TM binary systems. [2,4] They are crystallographically similar; one might think of 2:17 as an ordered substitution on the 1:5 lattice. This leads to extensive mutual solid solubility which has important consequences for alloy and microstructure formation. Of somewhat lesser importance are two more closely related intermetallic compounds of stoichiometry $(RE)_2(TM)_7$ and $(RE)(TM)_3$. Many of these phases, especially those containing Fe, Co, or Ni are magnetically ordered at low temperatures. The large magnetocrystalline anisotropy of some of these noncubic phases provides the basis for their use as permanent magnets.

Of all the RE-TM binary systems, the SmCo system is the most important. Figure 1 reproduces a published binary SmCo phase diagram.[4] It is typical of many RE-TM systems having several intermetallic compounds and a cascade of peritectics near the Co-rich end of the diagram. The phases of primary interest for magnets are Sm_2Co_{17}, $SmCo_5$, Sm_2Co_7, and $SmCo_3$. Of particular interest here is the large region of mutual solid solubility at high temperatures for the 1:5 and 2:17 phases. Note also that

the 1:5 phase is believed to decompose into 2:17 and 2:7 phases below 750 ^{o}C by a eutectoid reaction. This transformation is not well documented as the kinetics seem to be very slow. Many commercial magnets are made from binary $SmCo_5$; although technically metastable, it is possible to retain this phase at typical operating temperatures.

Significantly, the 1:5 phase does not occur in the SmFe system, although this binary, shown in Figure 2, is similar in general appearance to the SmCo system [2]. 1:5 phases are, however, common to the RECu, RENi, and RECo systems.

For phases of 2:17, 1:5, 2:7, and 1:3 stoichiometries, trivalent rare earth elements can generally be freely substituted for each other without major changes in phase stability. This would be expected from the similarity of the phase diagrams. (See, for example Nesbitt and Wernick [2]).

Crystallography. All the phases of interest here are crystallographically related to the $RECo_5$ structure. A perspective view of the conventional unit cell of this structure appears in Figure 3. The lattice is primitive hexagonal (P6/mmm) and the crystal structure, commonly referred to as $CaCu_5$ type ($D2_d$) consists of one formula unit per primitive cell (three formula units per conventional cell). This is a layered structure; planes of RE and Co atoms alternate with planes containing only Co atoms. The RE atoms have the configuration of atoms in a close-packed plane but with Co atoms at intermediate positions

[1/3<10$\bar{1}$0>]. The configuration of atoms in the Co planes is similar to that of atoms in the close-packed planes of fcc or hcp metals, except for periodic absences. (See Figure 6, lower half.)

In order to obtain 2:17 stoichiometry, one third of the RE atoms must be removed and replaced by pairs of Co atoms. These Co atom pairs are aligned along the crystallographic c-axis; they are commonly referred to as "dumbbell" sites. These sites are normally ordered in one of two different patterns giving rise to two commonly observed forms of the 2:17 phases. The hexagonal 2:17 (H2:17) and rhombohedral 2:17 (R2:17) structures are depicted in Figures 4 and 5. H2:17 ($P6_3/mmc$, Th_2Ni_{17} prototype structure) consists of ...ABABAB... stacking of the mixed planes along [0001]. The mixed planes of the R2:17 ($R\bar{3}m$, Th_2Zn_{17} prototype structure) are arranged in an ...ABCABCABC... type stacking sequence. As implied by the stacking sequences, the c-axis parameter of H2:17 is approximately twice that of the 1:5 phase; in the case of R2:17, the c-axis approximately triples. Heavy rare earth (atomic #$\geq$64 = Gd) 2:17 compounds are found primarily in the H2:17 form; light rare earths, in the R2:17 form. Sm_2Co_{17} has been reported to take the R2:17 form, but rapid quenching techniques can retain the H2:17 form. There is some evidence [7,8] that the stable form of Sm_2Co_{17} at high temperature (T_{-} >1250°C) is the H2:17 form. A brief summary of useful data for binary SmCo 1:5, H2:17, and R2:17 phases appears in Table 1.

While the crystal structures of the two 2:17 forms as depicted in perspective drawings such as Figures 4 and 5 seem complicated and somewhat formidable, these structures in fact

have a close analogy with common hcp and fcc crystal structures. Within a given mixed plane, the dumbbell sites are in the same configuration as atoms are in the close-packed planes of hcp and fcc metals; the dumbbell sites have six-fold in-plane symmetry and coordination (Figure 6). Just as it is only a change in stacking sequence of atom planes which converts fcc to hcp (...ABCABCABC... stacking transforms to ...ABABABAB... stacking), so it is only a change in stacking sequence of dumbbell sites which distinguishes R2:17 from H2:17. Just as large numbers of polytypic structures can be generated by more elaborate stackings of atomic close-packed planes, so it is conceivable that 2:17 stoichiometry can be retained in a large number of different structures corresponding to elaborate stackings of dumbbell sites. In terms of Ramsdell's [9] notation for polytypes, R2:17 and H2:17 would be denoted 1R and 2H respectively; the same can be said for fcc and hcp structures. Figures 7 and 8 schematically depict the 1:5, R2:17, and H2:17 structures as well as several other polytypes. Because of the close analogy between fcc and hcp and R2:17 and H2:17, many of the concepts of stacking faults and fcc (rhombohedral) twinning are directly applicable to the 2:17 phases. This analogy does break down due to the fact that there are atomic positions between the dumbbell sites within the mixed planes and layers of Co sites between the mixed planes. This, in principle, allows the possibility of ...AAA... stacking (or, at least, ...AA.. type faulting), although it has never been observed.

The RCo_3 and R_2Co_7 phases are also structurally related to

the $RECo_5$ phase. [10,11] If a RE atom replaces a Co atom in the mixed plane for every third layer of the 1:5 structure, the 2:7 stoichiometry results; if the substitution occurs every second layer, the composition shifts to 1:3 stoichiometry. Since the RE atom is too large for this site, the adjacent RE atoms are displaced slightly along the c-axis to accommodate it. The vacancies in the Co layers likewise shift to give the necessary volume. Here also, relative positions of the substitutions can produce various polytypes, the simplest cases having hexagonal (2H, $P6_3/mmc$) or rhombohedral (1R, $R\bar{3}m$) symmetry. Figures 9, 10, 11, and 12 give schematic drawings of these structures. Many concepts derived from stackings of close-packed planes can also be applied to these structures. Both binary $SmCo_3$ (1:3) and Sm_2Co_7 (2:7) have been reported to have rhombohedral symmetry with ~2.4 nm (6(0.4nm)) and ~3.6 nm (9(0.4nm)) c-axis repeats, respectively [10,11].

In some RECo systems, at least one phase of composition between 2:7 and 1:5 is known to exist.[12] This 5:19 phase can be formed from the 1:5 phase by substitutions of a RE atom for a Co atom every four mixed planes. Rhombohedral and hexagonal forms are conceivable; their c-axis parameters would be approximately 4.8 and 3.2 nm, respectively. Thus, the 1:2, 1:3, 2:7, and 5:19 form a sequence of structures having successively larger unit cells; Khan [13] has described such a sequence in terms of the following formula:

$$RE(TM)_x; \qquad x=(5n+4)/(n+2)$$

Members of this sequence with n>3 would lie between 5:19 and 1:5; in fact 1:5 can be thought of as the limiting structure for n infinite. No 5:19 phase has been reported in the SmCo system; it is not known what stabilizes such structures and why they appear in some systems and not in others.

The structures having RE content greater than the 1:5 compounds have been shown to crystallize in structures following a simple sequence; it has never been documented, but a similar sequence is conceivable for RE concentrations less than the 1:5 phases. Replacement of RE atoms with pairs of Co atoms at every third position generates 2:17 from 1:5. A similar replacement every sixth position would generate 5:32 stoichiometry; it could take on a variety of hexagonal and rhombohedral structures. The extension to 8:47, 11:62...$RE(TM)_x$, $x=(15n+2)/(3n-1)$ is obvious. n infinite again corresponds to the 1:5 phase. None of these hypothetical structures have been documented; these compositions are only known to exist through point defects in the 1:5 and 2:17 compositions.

The reciprocal structure of 1:5 is also primitive hexagonal; it is depicted along with the corresponding reciprocal structures for the perfect 2:17 structures in Figures 13 and 14. A schematic drawing of the reciprocal structure for the rhombohedral form of the 1:3 phase appears in Figure 15.

Since all the above phases are structurally related, it is possible for various combinations of them to occur coherently within a single crystal with very little mismatch. As noted in

Figures 4 and 5, the 2:17 unit cells are conventionally defined such that:

$$[11\bar{2}0]_{1:5} \;//\; [10\bar{1}0]_{2:17}$$
$$(0001)_{1:5} \;//\; (0001)_{2:17}.$$

This is the usual hexagonal-rhombohedral orientation relationship; the apparent rotation of coordinates is only a consequence of choosing unit cells of highest symmetry. On the other hand, the 1:3 and 2:7 phases are related to the 1:5 directly:

$$[10\bar{1}0]_{1:5} \;//\; [10\bar{1}0]_{2:7} \;//\; [10\bar{1}0]_{1:3}$$
$$(0001)_{1:5} \;//\; (0001)_{2:7} \;//\; (0001)_{1:3}$$

Even though these phases have identical space groups as the 2:17 phases, lattice parameter changes dictate this lack of rotation. Because of this fact, the two situations can be distinguished when they occur coherently with the 1:5 phase.

The 2:17 phases are, at least conceptually, ordered forms of the 1:5 phase; the usual group theoretical relations [14] regarding the number of ordered variants are applicable. The 1:5 phase (space group P6/mmm) has 6/mmm point group, order 24. Ordering to produce the R2:17 reduces the symmetry to $R\bar{3}m$, point group $\bar{3}m$, order 12. Thus, there are 24/12 = 2 orientation variants of the R2:17 with respect to the 1:5 lattice. The H2:17 structure has $P6_3/mmc$ space group; its point group 6/mmm is equal to that of the 1:5 structure; there is, accordingly, only one H2:17 orienta-

tion variant in the 1:5 structure. Similar remarks apply to the R1:3, R2:7, H1:3, and H2:7 phases. The number of translational variants is given by the ratio of the volumes of the primitive cells of the ordered and disordered phases [14]. [Neglect small parameter changes accompanying ordering.] For R2:17, this gives three translational variants per orientational variant, or a total of 6 variants. H2:17 has only two translational variants. In terms of stacking sequences, the number of translational variants corresponds to the crystallographic multiplicity of sites for initial substitution at the onset of ordering. That is, for the ...ABCABC... stacking sequences, there are three positions which can be chosen as "A"; the "B" and "C" positions are then determined. Experimentally, one readily discerns orientational variants in diffraction experiments; a direct space approach (i. e. imaging rather than diffraction) is necessary to distinguish translational variants (unless a suitable signal can be obtained from the interfaces between translational variants).

Permanent Magnet Phases. An effective permanent magnet must possess a combination of high saturation magnetization, M_s, reasonably high Curie temperature, T_c, and some form of (preferably uniaxial) magnetic anisotropy. The possibility that some rare earth cobalt phases might meet these criteria was first suggested in 1966 when Hoffer and Strnat [15] reported the

presence of large magnetocrystalline anisotropy in YCo_5 and Y_2Co_{17}. Even though yttrium is not one of the rare earths, nor does it have a magnetic moment, its chemical similarity to the trivalent rare earths immediately hinted that high magnetocrystalline anisotropy might be present in some of the ferromagnetic $RECo_5$ and RE_2Co_{17} phases. This has indeed proved to be true.

Of the 1:5 phases, those containing heavy rare earths (atomic #≥64 = Gd) do not have large M_s because the rare earth ions are magnetically ordered antiparallel to the Co ions. The M_s value of these ferrimagnets is only the difference between the Co and RE contributions. $CeCo_5$, $LaCo_5$, and $NdCo_5$ do not have high M_s because of the low magnetic moment of the RE ions; Pm does not occur in nature, and divalent Eu does not form a $EuCo_5$ phase. Thus, attention quickly centers on $SmCo_5$, which does have a very large uniaxial magnetocrystalline anisotropy, high Curie temperature, and reasonable M_s. In practice, many commercial magnets are single phase, grain-oriented $SmCo_5$; of all magnets, they exhibit the highest intrinsic coercivity.

By increasing the Co content in these alloys, the M_s increases; the RE_2Co_{17} phases would therefore seem to be desirable. However, the anisotropy of the 2:17 compounds is weaker than that of the 1:5 phases, and it often favors basal plane magnetization, rather than the more desirable uniaxial (c-axis) magnetization. Sm_2Co_{17} is the only binary 2:17 with high M_s and uniaxial anisotropy at room temperature, but its anisotropy is not so strong as that of $SmCo_5$. Thus, its theoretical coercivity is

not so high. In practice, 2:17 magnets also contain many crystallographic defects which tend to serve as reverse magnetic domain nucleation sites, further reducing ${}_iH_c$. [17] Sm_2Co_{17} has not proved to be an effective permanent magnet.

Anisotropy. In order to make use of the higher M_s of Sm_2Co_{17} over that of $SmCo_5$, many attempts have been made to understand and, if possible, improve its magnetocrystalline anisotropy. Recently Callen [18] has simply and elegantly summarized data on $(RE)_2(CoFe)_{17}$ systems; Wallace et al. [6] have reviewed attempts to improve magnetocrystalline anisotropy for many 2:17 systems through chemical substitutions. Magnetocrystalline ansiotropy in 2:17 can be thought of as the resultant of the various anisotropies of the four Co sublattices and the RE sublattice(s). In binary Sm_2Co_{17}, Er_2Co_{17}, Tm_2Co_{17}, and Yb_2Co_{17}, the rare earth contribution favors uniaxial (c-axis) anisotropy; the rare earth component of the other 2:17's favors planar anisotropy. In all cases the Co sublattices as a whole favor magnetization perpendicular to the c-axis. Because of the different temperature dependences of the magnetization of the several sublattices, the rare earth anisotropy dominates at low temperatures and 2:17's containing Sm, Er, Tm, Yb are uniaxial as the temperature approaches absolute zero. As temperature increases, the rare earth component of anisotropy decreases faster than the Co component, ultimately resulting in Co dominance at high temperature. Sm_2Co_{17} is the only case of the above four for which the transi-

tion is well above room temperature.

The Co contribution to magnetocrystalline anisotropy in the 2:17's can be further resolved into contributions from the four separate Co sublattices. [6] For the case of Y_2Co_{17}, Inomata [19] calculates that those Co atoms lying in the mixed planes, but not on the dumbbell Co sites tend to favor axial magnetization. The remaining sites favor planar magnetization with by far the largest contribution arising from the dumbbell sites. The net effect is that the Co sites as a whole favor magnetization perpendicular to the c-axis. The fundamental origins of the magnetocrystalline anisotropy in the 2:17's does not seem to be well understood; it continues to be an area of scientific as well as technological interest.

The fact that Co gives a detrimental contribution to magnetocrystalline anisotropy in Sm_2Co_{17} immediately suggests a potential means of improving the overall anisotropy of the structure. Substitution of almost any transition element for Co should weaken the negative Co anisotropy, giving a net improvement to the overall system, although it would probably detrimentally effect the M_s value of the alloy. Any element which substitutes for Co preferentially at the dumbbell sites would be the most beneficial. This has in fact proved to be true; many elements have been substituted for Co and the anisotropy of the $Sm_2(CoTM)_{17}$ generally does increase for small concentrations of the substitutional component. Of the various substituents, Fe has the advantage of resulting in the smallest decrease in M_s, but it is not the most effective for anisotropy increase; Zr, Hf,

Ti, and V are all more efficient than Fe in improving the anisotropy of $Sm_2(Co)_{17}$ ternaries, but their limited solubilities severely restrict the total amount that can be added. Mn is similar to Fe in beneficial effects to anisotropy; Cu is not so effective, but gives surprisingly little loss in M_s. The remarkable effects of substituents on magnetocrystalline anisotropy has been variously attributed to selective substitution at the dumbbell sites [19,20] and to general overall band structure effects.[21] Explanation and understanding of these effects is sketchy at best; obviously the problem is not theoretically transparent and experimental determination of site occupation of substituents (e.g. a few Fe atoms at Co sites) is also not a trivial matter.

Microstructures. Improvement of anisotropy field for a specific phase improves its potential for high intrinsic coercivity, H_c, and its potential for permanent magnet applications, but, in practice, H_c may instead be limited due to other considerations. Improvements in anisotropy result in increased resistance to change in magnetization direction by coherent domain rotation, but the magnetization may still change direction by the migration of magnetic domain walls. In that case, H_c may be limited either by the difficulty of nucleating new reverse domains, or by the difficulty of propagating domain walls through the material. If intrinsic coercivity depends on the resistance

to nucleation of reverse domains; the material will exhibit a concave-upward virgin magnetization curve [16] as well as a very square demagnetization curve; (Figure 16) in both cases, the magnitude of applied field increases until an appropriate domain nucleates. This domain can then grow rapidly, reorienting the magnetic moments throughout the entire specimen, giving a sudden change in the hysteresis loop. If domain wall pinning is the dominant effect, (i.e. it is very difficult for a domain wall to propagate), one generally observes a concave-downward virgin magnetization curve and a demagnetization curve which has a slow dropoff from remanence followed by a decrease to zero following a path of lower slope (Figure 16b). Both of these processes have played a role in SmCo magnet technology.

For simple binary $SmCo_5$, intrinsic coercivity is limited by the nucleation of reverse domains at defects and especially at grain boundaries. The grain boundary is a termination of the lattice; anisotropy and, consequently, the energy expenditure in reorientation of magnetization are not so large near such a discontinuity. A grain boundary may also be a discontinuity in the directions of magnetization if adjacent grains do not have parallel c-axes; this situation produces demagnetization fields which act to favor reverse domain nucleation. Thus, to form an excellent $SmCo_5$ magnet, large, crystallographically perfect, and very well oriented grains are essential.

Stoichiometric Sm_2Co_{17} has too small an anisotropy field to be seriously considered as a permanent magnet, but, even so, its coercivity is limited by the nucleation of reverse domains.

Besides grain boundaries, reverse nucleation may also occur in the 2:17 structures at stacking faults and twins; at such regions the lattice is interrupted and there can be local changes in symmetry with the possibility of locally lower magnetic anisotropy.[22]

There have been many attempts to improve the intrinsic coercivity of RECo magnets by precipitation in order to pin the magnetic domain walls. Thus, a reverse domain wall, once nucleated, is stopped, and complete magnetic reorientation is avoided. Much of the work based on the 1:5 system has been reviewed by Nesbitt and Wernick [2]. These authors show that additions of $SmCu_5$ to $SmCo_5$ can, with suitable heat treatment, improve intrinsic coercivity. Small additions of Fe to this system are useful to minimize loss of M_s and $(BH)_{MAX}$ which inevitably accompanies Cu substitution. Microstructural examination has led Hofer [23] to believe that the $SmCo_5$-$SmCu_5$ system decomposes spinodally; he explains enhancement of magnetic coercivity of this alloy system in terms of pinning of magnetic domain walls at the fine-scale decomposition product. Fidler and co-workers [24,25,26,27] have reported several investigations of heterogeneous precipitation processes in $SmCo_5$ magnets. Smeggil _et al._ [28] and Fidler [29] discussed aspects of the 1:5 to 2:7 plus 2:17 eutectoid decomposition reaction.

Shifts in composition from the 1:5 stoichiometry toward higher Co concentrations result in 2:17 precipitates in a 1:5 matrix, or 1:5 precipitates in a 2:17 matrix. Livingston [30] has discussed the types of precipitation and their

effectiveness as domain wall pinning sites for various compositions between 1:5 and 2:17. Microstructural studies of such magnets include many examples of optical metallographic characterization,[31-38] but electron microscope investigations, when available, generally indicate the presence of a fine-scale, coherent precipitation which is unlikely to be detected using optical techniques. Various magnet alloys have been characterized by transmission electron microscopy and diffraction, but due to the complexity of the alloys, there have been few systematic studies. Leamy and Green [39] detected fine, coherent, equiaxed 2:17 particles in the 1:5 matrix for a $Ce(Co_{73}Cu_{17}Fe_{10})_{5.2}$ alloy. Livingston [30] characterized magnets of nominal compositions $Sm(Co_{85}Cu_{10}Fe_5)_{5.8}$, $Sm(Co_{73}Cu_{14}Fe_{12}Ti_1)_{6.7}$, $Ce(Co_{73}Cu_{14}Fe_{12}Ti_1)_{6.3}$, and $Sm(Co_{74}Cu_{13}Fe_{13})_{7.8}$,aged to optimum coercivity. In another study, Livingston and Martin [40] followed the evolution of a single $Sm(Co_{80}Cu_{15}Fe_5)_{7.0}$ alloy from initial precipitation to the extremely over-aged condition. Melton and Perkins [41] followed similar evolution in $Sm(Co_{65}Cu_{35})_{5.6}$ and $Sm(CO_{84}Cu_{16})_{6.9}$. Melton and Nagel [42] also studied alloys $Sm(Co_{87}Cu_{13})_{7.5}$ and $Sm(Co_{87}Cu_{13})_{7.8}$. Yoneyama *et al.* [37] and Mishra and Thomas [43] have characterized optimally aged $Sm(Co_{67}Cu_{10}Fe_{21}Zr_1)_{7.4}$

Although there are few, if any, systematic studies of microstructure and magnetic properties, the cited references and others are a significant body of work, and some trends can be identified. Compositions near the 1:5 and 2:17 stoichiometries tend to form precipitates on heterogeneities (*e.g.* dislocations,

stacking faults, and grain boundaries); the resultant wall pinning is ineffective. Cu tends to favor continuous precipitation reactions, especially far from stoichiometry, giving much more effective domain wall pinning. This is the motivation for introducing Cu into many of these alloys. Fe maintains high M_s, and $(BH)_{MAX}$; it does not seem to be associated with any pronounced metallurgical effect. Zr, Ti, and Hf are not understood from microstructural work; their beneficial effects on ${}_iH_c$ are attributed to increases they bring to the magnetocrystalline anisotropy of the 2:17 phase. From all the above, the best combination of ${}_iH_c$ and $(BH)_{MAX}$ seems to involve a fine, coherent, two-phase structure having rhomboid particles of 2:17 (~75 nm in size) surrounded by thin films of 1:5 stoichiometry (8-10 nm thick). The two phases are totally coherent, mismatch being accommodated by elastic strain of both phases without discrete interfacial dislocations. This "cellular"* structure occurs for compositions in the $Sm(CoTM)_{6.8}$ to $Sm(CoTM)_{8.0}$ range, where TM includes Cu and possibly other elements, and seems to be very effective for pinning magnetic domain walls.

The origin of the cellular structure in the best two-phase magnets has not been dealt with in the literature. It has been observed by several experimentalists and presumed to be necessary

---

*Not to be confused with "cellular" as applied to discontinuous precipitation products.

for domain wall pinning, but no author has addressed the question of the type of nucleation event, and consequently, the conditions required to generate uniform, continuous precipitation. There seems to be widespread acceptance of the desirability of the cellular morphology, but, historically, its formation was simply an accident, and it has not yet been explained.

Scientifically, the question of nucleation is intriguing. It is not obvious whether the reaction which generates the cellular morphology should be thought of as a clustering or as an ordering process. Whether it is one or the other hinges on the degree of order of the dumbbell/Sm sites at high temperatures where these alloys are presumably single-phase.

If the dumbbell/Sm sites are ordered, then the excess Sm due to off-stoichiometry is present as point defects on the lattice. If that is the case, then, cooling across the solubility limits should result in clustering of excess Sm to form 1:5 precipitates. The initiation of such clusters might follow either of the two conventional processes. If the system is stable with respect to long-range fluctuations, the precipitation process may occur by short-range statistical fluctuations leading to clustering and the formation of the SmCo equivalent of GP zones and subsequent growth into 1:5 particles. Alternately, it is conceivable that the system may become absolutely unstable at quench temperatures, and spinodal decomposition of the Sm and the dumbbell sites might occur. Spinodal decomposition is intuitively appealing because the end produce is a modulated structure - a microstructural characteristic commonly associated with spinodal

decomposition. However, modulated structures are not necessarily due to spinodals. [44]

On the other hand, it is conceivable that the dumbbell/Sm sites are completely disordered at high temperatures. Then it is possible that ordering to form R2:17 could occur. This reaction would take the system from the supersaturated 1:5-type structure to the ordered R2:17, generating the usual growth antiphase boundaries. After the ordering occurs, the excess Sm would be ejected from the lattice to form 1:5 precipitates on the antiphase boundaries. This could conceivably generate the cellular structure, but the question of nucleation remains. The classical Landau-Lifshitz criteria [45,46] imply that this reaction (P6/mmm to R$\bar{3}$m) can not be second order. It <u>is</u> possible to construct a third order invariant of the R2:17 reciprocal lattice vectors to form one of the 1:5's. Thus, this must be a first order transition, and the activation barrier for nucleation remains. To distinguish the possible phase transformation types it would be desirable to have a high temperature single crystal x-ray diffraction experiment, but the usual homogenize and quench experiments may be valid for a system requiring diffusion of Sm and Co dumbbell pairs.

<u>Summary</u>. This section has given a brief introduction to the subject of rare earth-cobalt permanent magnets. The magnetic properties of these alloys depend on factors ranging from the effects of point substitutions on the magnetic properties of

intermetallic compounds to the sizes and distributions of these compounds in a magnet. It is an alloy system where metallurgical effects such as nucleation and growth of precipitates as well as solid state physics phenomena such as magnetocrystalline anisotropy are coupled to form a wide range of physical properties.

Aim and Approach of this Investigation

SmCo, like most permanent magnet alloys, can be simply characterized in terms of a few magnetic parameters such as $(BH)_{MAX}$ or H_c, but the numerical values of these macroscopic magnetic properties are the results of a complex and poorly understood interplay of atomistic and microstructural factors. Specifically, for the SmCo system, macroscopic magnetic behavior depends on the compositions and relative proportions of the 1:5 and 2:17 phases, their sizes and distributions. Any other phase would also be expected to play a significant role. In practice, SmCo magnets are not equilibrium structures; all the above parameters depend on their thermal history.

In trying to understand the origins of magnetic properties, one can always resort to a few general principles, such as 1) M_s depends primarily on composition for a given phase; it is relatively insensitive to microstructure, 2) ${}_iH_c$ is always sensitive to microstructure, but the mechanism - domain wall pinning or reverse domain nucleation - influences the type of

dependence, 3) $(BH)_{MAX}$ is a combination of M_s and ${}_iH_c$. However, in practice every magnet alloy system is different and any new system must be duly characterized if its behavior is to be understood. So it is with SmCo.

The present generation of SmCo magnets is the result of an evolutionary process in which increasingly sophisticated magnets were produced by successive modifications of existing ones. This process began with the $SmCo_5$ magnets; additions of Cu and Fe were found to be favorable, but the resulting $Sm(CoCuFe)_5$ alloys did not have high M_s ($4\pi M_s$=9500 G) nor high $(BH)_{MAX}$ (16 MGOe). Sm_2Co_{17} has higher M_s ($4\pi M_s$=12000 G), but lower ${}_iH_c$; anisotropy could be improved by adding Fe or Mn, but the result was still unsatisfactory. Finally, intermediate compositions were examined. $Sm(CoCu)_{7.5}$ was found to have higher ${}_iH_c$ than the 2:17's and still retain higher M_s than the 1:5's. Subsequent modifications have established an optimum $(BH)_{MAX}$ in the range $Sm(CoCuFeZr)_{7.2-7.5}$. As the alloy compositions were becoming more complex, so were the heat treatments. Thermal processing for the modern two-phase magnets involves homogenizing, quenching, aging, and step-aging. Thus, the best [highest $(BH)_{MAX}$] magnets available are five-component systems, SmCoCuFeZr, of overall stoichiometry 1:7.4. They are formed from magnetically grain-oriented powders, homogenized, quenched, aged, and step-aged.

The development of SmCo magnets has been very successful. From a typical $SmCo_5$ $(BH)_{MAX}$ value of 16 MGOe, a largely trial-and-error approach has produced magnets in the 33 MGOe range - a two-fold increase. However, scientific understanding has not kept

pace with this development. The roles of the several elements in these complex alloys are obviously not understood, but even such fundamentals as the role(s) of substituents within a single intermetallic phase are still in dispute. For example, the effectiveness of Fe in increasing the magnetocrystalline anisotropy of $Sm_2(CoFe)_{17}$ has been variously attributed to preferential site occupation, [19,20] or cooperative band structure effects, [21] or both; experimental verification is unavailable. The role of domain wall pinning hints strongly at the role of microstructure in the development of excellent magnets. The few (relative to the large number of alloys and processing parameters) microstructural studies have not been systematic; only a few general ideas can be distilled from them. The action of Zr (and related elements Hf and Ti) in contemporary alloys is completely obscure; one can only say that these elements are known to be beneficial. The lack of scientific understanding of the rare earth-cobalt permanent magnets seems to have limited their development; there have been no reported advances in $(BH)_{MAX}$ values in the past four years. The trial-and-error approach seems to have located a local maximum in composition/processing space; it will require either a fortunate accident or a better understanding of the system to produce further advances.

Further advances in $(BH)_{MAX}$ ar not unreasonable to expect; the theoretical* maximum $(BH)_{MAX}$ value based on the M_s of

---

*Theoretical $(BH)_{MAX} = (B_s)^2/4 = (4\pi M_s)^2/4$

$Sm_2(CoFeMn)_{17}$ magnets is 49 MGOe [47] which is still well above that of the present generation of magnets.

This thesis describes the results of an experimental investigation of the development of microstructure and magnetic coercivity in contemporary SmCo-based magnets. The approach has been to characterize the microstructure of a series of the best available magnets - the five-component $Sm(CoCuFeZr)_{7.4}$ alloys - and to correlate it with the observed coercivities and energy products. The evolution of the domain wall pinning sites and the role(s) of Zr are two stated, primary objectives. They are pursued by studying alloys of differing Zr concentrations subjected to a large number of different thermal treatments. The results of these experiments will be discussed, both as they apply to these specific alloys and as they are apply to related RECo magnets.

EXPERIMENTAL

Alloys.

In order to study the evolution of the microstructure and its effects on magnetic coercivity, and the role(s) of Zr in these processes, alloys have been chosen which vary the level of Zr substitution, holding all other components (save Co) constant; these alloys have been subjected to a large number of heat treatments. The alloys for this study have nominal compositions in wt% 25.5 Sm, 15 Fe, 8 Cu, 1.5 or 3.0 Zr, remainder Co. [$Sm(Co_{67.4}Fe_{21.3}Cu_{10.0}Zr_{1.3})_{7.43}$ and $Sm(Co_{65.8}Fe_{21.5}Cu_{10.1}Zr_{2.6})_{7.37}$] The heat treatments fall into two major classes: 1) those involving an isothermal aging process, and 2) those involving an isothermal aging process plus a step-aging procedure. A third alloy containing no Zr [25.5 Sm, 15 Fe, 8 Cu, Co = $Sm(Co_{69}Fe_{21}Cu_{10})_{7.5}$] has been included to determine more generally the nature of the phase transformations in this system.

All the alloys and magnetic property data for this study have been prepared by TDK Electronics Research and Development Laboratory as part of a systematic optimization process. [1,37,48] Their procedures are as follows. Component metals, Sm, Co, Fe, and Cu, all with purities exceeding 99.5 wt% and ferrozirconium were melted together in an induction furnace under

Ar atmosphere. Favorable c-axis grain alignment was effected by first crushing and pulverizing the as-cast ingots in a jet mill and then simultaneously applying in orthogonal directions, both a 10 kOe magnetic field and a 1.5 ton/cm^2 mechanical pressure. The resulting grain-oriented green compacts were sintered for one hour at temperatures between 1150 and 1250 ^{o}C in Ar atmosphere. After sintering the specimens were solution treated for 1 hour between 1100 and 1220 ^{o}C, then quenched in Ar atmosphere. All heat treatments involved an 850 ^{o}C isothermal aging for various time periods; "step-aged" alloys were subsequently cooled directly from 850 to 400 ^{o}C at 1-2 degrees per minute and then aged at 400 ^{o}C for 10 hours. All treatments were terminated by an Ar atmosphere quench. An automatic recording fluxmeter and pulse magnetizer were used to measure magnetic properties and magnetize specimens respectively.

Besides the TDK procedures described in the previous paragraph, specimens were heat treated as needed to characterize the system completely. Specimens were abraded on 600 grit SiC paper, sonicated in n-heptane, wrapped in a Ta foil as O_2 getter, and encapsulated in evacuated silica glass capsules. Temperature control was monitored by a chromel-alumel thermocouple adjacent to the capsule. Heat treatments were terminated by quenching (10^3 degrees per second) the capsule into water at room temperature without breaking it. Sequential treatments were done without removing the specimen from the capsule. For phase transformation studies, alloys were homogenized for one hour at temperatures between 1160 and 1235 ^{o}C and quenched; aging

followed the TDK practice of 850 ^{o}C, but only for 20 minutes.

Transmission Electron Microscopy and Microanalysis.

Transmission electron microscopy (TEM) and related microanalytical techniques have been used throughout this investigation. In general, conventional diffraction contrast imaging conditions [bright field (BF), dark field (DF), and weak beam (WB)] were appropriate to characterize the morphology of the precipitates. Selected area diffraction (SAD) was invaluable for determining which phases were present. Imaging was accomplished using Philips 301 and Philips 400 electron microscopes. Phase contrast structure imaging was done on a Siemens 102, all microscopes were operated at 100 kV.

Microdiffraction and microanalysis were accomplished using the Philips 400 scanning transmission electron microscope in the TEM mode. In this configuration, an electron probe of 40 nm nominal size is formed on the specimen via the condensor system. This probe is small enough to form single crystal rhombohedral 2:17 diffraction patterns in optimally-aged alloys, but it is not small enough to detect segregation of constituents among the several phases. The 1:5 material is typically 8 nm thick; even using a 4 nm STEM probe was ineffective due to problems of beam broadening in the foil and accurate placement of the probe on the 1:5 material. To avoid these problems, specimens were over-aged

for 100 hours at 960 °C. This coarsened the microstructure such that the microanalysis could be easily done in the TEM configuration. Because such a structure is not truly representative of a useful microstructure, it is not expected to have the same compositions as the useful alloys. Thus, quantitative analyses were not appropriate and were not attempted.

Specimen Preparation.

Electron transparent foils for TEM examination were prepared by ion beam milling techniques. Specimens supplied by TDK were in the form of small plates of approximate dimensions 10 mm x 15 mmm x 0.3 mm. Generally the specimens were grain-aligned such that the crystallographic c-axis (the direction of easy magnetization) lay in the plane of the plate. These brittle plates were simply broken into fragments ~ 0.2 cm in size; one surface of each fragment was cleaned using successively finer SiC papers until a significant layer (perhaps 0.1 mm) of the surface was removed and a 600 grit surface remained. This clean surface was then polished using a common metal polish, leaving a specular finish; some 600 grit scratches remained. This was not done to obtain a metallographic finish, but to produce a smooth surface so that subsequent ion beam milling would produce a smaller wedge angle. The metal polish was removed using n-heptane and acetone and the fragment was cemented to a glass slide using heat setting wax. To do this, the slide was placed on a hotplate; at the softening temperature (~ 60 °C), the wax was melted onto

the slide and the fragment was placed polished-side-down in the wax; it was held tightly against the slide until the wax reset. The fragment was then thinned on SiC paper using sequentially finer grit sizes until it began to break up on 600 grit paper. After polishing this side with the metal polish, optical microscopy revealed that the specimen was typically reduced to 35 -50 microns thickness. The fragments were removed from the glass slide by reheating; the wax residue was eliminated by rinsing in boiling ethanol. At this stage, specimens were typically less than 1 mm in any dimension, thinned to 30-50 microns; this is essentially the limit where the present author could no longer manipulate them reliably with tweezers and magnets. Specimens were deliberately made this small to minimize the detrimental effects of ferromagnetism in the specimen on the electron microscope imaging. These fragments were placed on Cu support rings, the sizes of which were chosen to fit the individual fragments. The support ring was first coated with epoxy; all excess was carefully eliminated to leave a very thin, uniform, film. The fragment was then dropped onto the ring, and a hotplate was used to set the epoxy, being careful not to let the support ring adhere to its support, but being sure that the fragment remained securely fastened to the support ring. (Many potential foils were lost at this juncture.) For ion beam milling, it was usually necessary to sandwich the effective support ring and fragment between two more rings. This was done to protect the Cu support ring which mills faster than the SmCo; failure to do so could result in loss of foil due to loss of support ring. Ion

beam milling was done using an Ar ion beam, accelerated through 6 -10 kV, impinging on the specimen at approximately 20 degrees to the specimen surface. Specimen currents of ~ 20 microamps per gun at 6 kV would result in perforation in 12-20 hours. The foils were commonly perforated at many points. It is not certain why this was so, but it is suspected that the 600 grit scratches on both sides of the fragment before ion milling caused a surface waviness to occur after milling. There was no evidence to suspect preferential milling of a specific phase as a great number of specimens were examined and the results were always mutually consistent.

Microstructural Quantification.

Microstructural parameters were quantified as systematically as possible by measurements made on TEM micrographs and diffraction patterns. Images were generally recorded in the $\langle 1\bar{1}00\rangle_{1:5}$ and $\langle 11\bar{2}0\rangle_{1:5}$ orientations. This allowed determination of the cell size, the 1:5 habit plane, the 1:5 cell wall thickness, the density of R2:17 twins, and the density of the thin plates of a new phase. The c/a ratio was routinely obtained from SAD patterns in both symmetric orientations. The degree of regularity of the cellular structure was duly noted; other features, such as grain boundaries, were noted when observed.

Quantitative measurements of microstructural features are expected to vary widely in accuracy as well as in statistical confidence due to the nature of the TEM examination process.

Attempts were made to minimize the inherent subjectivity of the TEM examination by photographing the first area of the specimen encountered which was simultaneously sufficiently electron transparent and oriented appropriately such that the two poles of interest could be reached by tilting. After the photographs were recorded, the foil was scanned to obtain a subjective determination of whether the photographed volume was representative or not. Measurements on the micrographs were done in the usual ways. The number of intercepts of cell walls with a length of line perpendicular to the cell walls on the micrographs was used to estimate the average cell size. Lines were taken parallel to the c-axis to determine the twin thickness and the average plate density. To determine the inclination of the 1:5 cell walls from the basal planes, as many measurements as possible were taken from straight sections of cell walls and the results were averaged. This was a highly subjective measurement, as each cell wall had to be judged for straightness and its actual position estimated. The 1:5 cell wall thickness could only be measured from DF micrographs in which the foil was in the symmetric $\langle 1\bar{1}00 \rangle_{1:5}$ orientation and the 2:17 reflections were allowed to contribute to the image. This DF technique is the only way to separate the effects of structure factor contrast from lattice strain contrast. The clear structure factor contrast of the DF image allows the 1:5 material to be clearly delineated as dark bands between the light 2:17 particles. Error arises in this measurement in that the projection of the 1:5 cell walls is normally ~ 2 mm wide at the usual 50,000 to 100,000 x magnifica-

tion ranges; the limit of human visual resolution is a significant part of 2 mm; thus, without extreme photographic enlargement, measurement errors are sure to occur. In all these cases, statistical confidence is limited by the number of measurable features within the area of the micrographs; for the cell wall thickness and the cell size, this is probably not restrictive, but for the twin thickness, the plate density, and the habit plane inclination, situations occurred where the number of features was so small that there could be very little confidence in it. Nevertheless, in no cases were the results in contradiction with those of a similar alloy; by examining a series of alloys and occasionally repeating specific cases, the level of confidence of the group as a whole is much better than any individual measurement.

RESULTS

The experimental results will be presented in the order they were obtained. The magnetic property data obtained by TDK [47] in their search for optimal properties among a large number of alloys will be presented first. These data are closely related to the main work of this investigation and serve to broaden and corroborate the data from the microstructrural characterization. Of all their data, those which are the most closely related to this work are the result of a study of the effect of post-sintering heat treatments and Zr content on the intrinsic coercivity; the microstructures generated by these alloys and heat treatments are here characterized by transmission electron microscopy and diffraction (TEM). Several features are common to the microstructures of these alloys; they have been characterized by imaging and diffraction techniques as well as by energy dispersive x-ray spectroscopy (EDXS). The effects of alloy composition and heat treatment on the microstructures and coercivities are determined by routine measurements on many micrographs. Correlations between structure and properties are presented in an attempt to establish the optimum microstructure for coercivity. The phase transformations which are instrumental in the development of the useful two-phase structure are characteristic of this system; the results of experiments to determine their nature will close this section.

Macroscopic Magnetic Data

The approach taken by TDK to systematically search for optimal alloys was to begin with a single alloy system Sm(CoCuFe) and vary the concentration of each individual component, holding the others save Co constant. Once the optimal value for a given alloy compositional variable was established, that component was fixed and another component was varied. This was done for all the components within restricted ranges in hopes of finding an optimal alloy. It should be noted that this approach, if only completed once, will not necessarily reach the optimum for the ranges investigated; an iterative routine would be necessary to accomplish this with certainty. However, these data were obtained after years of experience with these alloys and their best magnet is probably very nearly optimal.

Shifting the Sm to transition metal ratio shifts the ratio of the volume fractions of the two major phases. In the range of interest, a higher Sm concentration results in a larger volume fraction of the 1:5 material. Figure 17 presents the results of varying the Sm content on the intrinsic coercivity (${}_iH_c$) and the squareness of the demagnetization curve. The loop squareness is quantified somewhat arbitrarily by the value of H for which the demagnetization curve falls to 0.9 B_R. The data is recorded for Sm concentrations between 23 and 26.5 wt% [$Sm(CoFeCuZr)_{8.48}$ - $Sm(CoFeCuZr)_{7.0}$] The levels of the other elements are in wt% 15 Fe, 3 Zr, 6 or 8 Cu, and remainder Co. As noted, data for alloys which were isothermally aged for one hour at 850 ^oC, with and

without a final step-aging treatment, appear in the figure. The compositions in this range essentially cover the regime in the pseudobinary phase diagram for which one would expect 1:5 precipitates in a 2:17 matrix.

If the Sm concentration is maintained at an intermediate level, the ratio of the volumes of the 1:5 to 2:17 material will remain constant and it will be possible to investigate the effects of the other elements as they substitute for Co. Figures 18 and 19 show the intrinsic coercivity of a series of 25.5 wt% Sm alloys as functions of Fe, Cu, and Zr content. Again, all the alloys have been subjected to aging, and aging followed by step-aging, treatments. The data in these figures constitutes a significant body of empirical information about alloys in the system. The apparent trends resulting from changes in the several compositional variables will be relied on to interpret the micrographs.

The main thrusts of this investigation are to establish the effects of Zr and heat treatment on microstructure and coercivity for the highest coercivity two phase magnets. Figure 20 summarizes the macroscopic measurements most directly related to the objective of this investigation. In this figure, ${}_iH_c$ is plotted as a function of aging time at 850 ^oC for two alloys - 1.5 and 3.0 wt% Zr. Some alloys were simply aged at 850 ^oC for time as given on the abscissa and quenched; some alloys were aged at 850 ^oC for times given by the x-axis and step-aged to 400 ^oC and quenched. The coercivity improvements from step-aging are dramatic. The effect of Zr concentration is paradoxical; the 3

wt% Zr alloy achieves highest coercivity when step-aged, but lowest when not step-aged. This, in itself, points to strong effects of microstructures and compositions of the phases.. It establishes that the effects of heat treatment and the role(s) of Zr are inextricably related.

Microstructures.

In alloys aged near peak coercivity, four microstructural features are generally present. A coherent "cellular" structure of 1)hexagonal 1:5 cell walls (~8 nm thick) and 2)rhombohedral 2:17 cell interiors (50 - 100 nm in size) is always observed. The R2:17 particles generally occur in 3)two twin-related variants. 4)Occasionally superimposed on the cellular structure are thin plates of a third phase.

Figure 21a is a TEM micrograph taken at a $\langle 1\bar{1}00\rangle_{1:5}$ pole (c-axis in the plane of the foil) in which all four features are present and visible. The corresponding SAD is included as Figure 21b. Indexing of the SAD pattern is consistent with a combination of hexagonal 1:5 and rhombohedral 2:17 phases; no hexagonal 2:17 spots are observed. From the diffraction information, the usual hexagonal/rhombohedral orientation relation is found to apply:

$$(0001)_{1:5} \;//\; (0001)_{R2:17}$$

$$[11\bar{2}0]_{1:5} \;//\; [1\bar{1}00]_{R2:17}$$

The high intensity spots in the SAD are common to both cellular phases; they appear as stars due to the shape effect of, or lattice strain associated with, the 1:5 cell walls. The actual image contrast of the cellular structure is due to lattice strain which arises because of the misfit of the two coherent phases as well as the contrast due to differences in the structure factors of the two phases. The lattice mismatch is reflected in the slight splitting of the diffraction spots in the higher order reflections.

The twinning within the R2:17 cells is visible in the Figure 21a as bands of alternating intensity running perpendicular to the common c-axis; in the SAD (Figure 21b), there are two rhombohedral patterns corresponding to the two variants. As mentioned in the background material, one expects two twin-related variants of the rhombohedral phase when it occurs as an ordering on the hexagonal lattice; this is found to be true for all alloys studied - a hint that the cell interior phase truly has rhombohedral symmetry. The interfaces between twins lying on the basal planes can be variously described as twin boundaries or as nonconservative antiphase boundaries; for this situation, the two are entirely equivalent. The basal plane twinning is expected to be completely chemically conservative, and therefore is not expected to arise in an attempt to accommodate off-stoichiometry.

The thin plates, visible in Figure 21a as linear features running across the image from upper left to lower right are responsible for the faint streaking in the $[0001]^*$ direction and

the faint spots at 0.8 inverse nm in the SAD pattern. These plates lie on the common basal plane of the 1:5/2:17 cellular structure; their broad faces are totally coherent with both major phases. Subsequent analyses show them to be a new phase, enriched in Zr with respect to the major phases. They have been dubbed the "Z" phase.

Because many of the features in these structures lie on the crystallographic basal planes, it is most convenient to view the foils in orientations which allow the basal planes to be imaged edge-on. Thus, most images included here are from foils oriented such that the c-axis lies perpendicular to the electron beam. The crystals can be rotated about the c-axis; two high symmetry poles occur, separated by 30 degrees rotation. Figure 22 was taken along a symmetric $\langle 10\bar{1}0\rangle_{1:5} = \langle 11\bar{2}0\rangle_{2:17}$ orientation. This is generally the most useful orientation, as the 2:17 reflections are distinct from the 1:5 reflections (see Figure 23), and it is therefore possible to image the 2:17 regions in dark field. The cell walls are nearly edge-on in this orientation. A 30 degree rotation about the c-axis brings the specimen to the $\langle 11\bar{2}0\rangle_{1:5} = \langle 10\bar{1}0\rangle_{2:17}$ orientation. In this reciprocal lattice section, all the 2:17 spots superimpose with those of the 1:5 (Figure 24) Figure 25 shows the same area of the foil as was shown in Figure 22, but oriented such that the electron beam follows the other high symmetry direction. The specimen imaged in Figures 22 and 25 is a 3% Zr alloy, aged 3 hours at 850 ^{o}C and step-aged. ${}_iH_c$ = 24 kOe. In both images the usual features appear. Since this is a high Zr alloy, there is a correspondingly high volume fraction of

the Z phase plates running across the images. The cells are relatively small, approximately 65 nm. The SAD's (Figures 22b and 25b) also follow the usual pattern; there are bright spots common to all phases and streaking parallel to the reciprocal c-axis due to the Z phase plates. The 1:5 spots appear as stars in both sections; because of the 6 crystallographically equivalent habit planes, the 1:5 spots take the form of 12-pointed stars in reciprocal space.

The 1:5 cell walls tend to lie on the $\{0\bar{1}11\}_{R2:17}$, but do not seem to be rigidly confined to this orientation. Mistakes are commonly observed, both in inclination with respect to the basal plane and in rotation about the c-axis. In Figure 22, most cell walls are nearly edge-on and they lie at approximately 60 degrees to the basal plane (30 degrees from the c-axis) as would be expected for $\{1\bar{1}01\}_{R2:17}$ in this orientation, but close inspection reveals some walls which are significantly deviated from the 60 degree norm. In Figure 26, the structure is viewed along the c-axis. Although many of the cell walls do lie perpendicular to the $\langle 11\bar{2}0\rangle_{1:5} = \langle 1\bar{1}00\rangle_{2:17}$ in this projection, there is significant deviation from this pattern. This suggests that the habit plane is not a rigidly established crystallographic feature; there is a reduction in energy associated with this morphology, but it is not a large effect.

The twinning of the R2:17 material is always observed, although there is large variability in its frequency. Figure 27 shows an example of one of the more highly twinned structures. This is a low Zr alloy and the foil orientation (see inset SAD)

is such as to emphasize the contrast of the twins. The foil is oriented such that one R2:17 orientational variant is in a much better configuration for strong diffraction than the other, heightening the structure factor contrast between the two. It can be clearly seen that the twinning is a feature of the 2:17 cell interiors only, as the 1:5 material is often a discontinuity in contrast. In a sense, the 1:5 material plays the role of non-basal plane antiphase boundaries. As a disordered phase, it can account for the stacking shifts between translational variants which would normally require an antiphase boundary, without showing the usual contrast effects associated with antiphase boundaries. The R2:17 stacking simply loses its identity at the 1:5 and starts again after ~8 nm. On the other hand, the basal plane must be a very low energy position for twinning (non-conservative antiphase boundaries), as the density of such faults is very high, even in the presence of the 1:5 material.

The Z phase plates occur in most of the alloys after they have developed a well-defined cellular structure. They are always extremely thin; if they are not imaged edge-on, they show fringe contrast akin to that expected for stacking faults. Edge-on, they appear to have a finite thickness, which usually appears to be ~ 2 nm, but occasionally thicker, ~6 nm. The upper half of Figure 28 is an example of a micrograph from an alloy with a high density of the Z phase plates. They appear as bands running horizontally across the image. (The c-axis is vertical.) Streaking in the SAD has been used to form the DF image of Figure 28b; the plates reverse contrast, indicating that they are, in fact,

responsible for the streaking.

A series of experiments was performed in order to determine the structure of the Z phase. Using an alloy with a high volume fraction of the Z phase, SAD's were recorded in the $\langle 10\bar{1}0\rangle_{1:5}$ = $\langle 11\bar{2}0\rangle_{2:17}$ and the $\langle 11\bar{2}0\rangle_{1:5}$ = $\langle 10\bar{1}0\rangle_{2:17}$ poles. (The lower halves of Figures 22 and 25). In these SAD's, streaking due to the thinness of the plates makes it impossible to infer the complete reciprocal lattice. A structure image of such an alloy in a $\langle 10\bar{1}0\rangle_{1:5}$ = $\langle 11\bar{2}0\rangle_{2:17}$ symmetric orientation appears in Figure 29. The Z phase plates image as 0.8 nm fringes running in bands, roughly vertically. The $\{10\bar{1}1\}$ planes of the R2:17 matrix are also imaged; the two twin-related variants occur as families of fringes at approximately 60 degrees to the Z phase fringes. The usual strain contrast due to coherency misfit between the 1:5 and 2:17 superimposes large, slowly varying oscillations in the background intensity. A similar image, taken along $\langle 11\bar{2}0\rangle_{1:5}$ = $\langle 10\bar{1}0\rangle_{2:17}$ also reveals 0.8 nm fringes inside the Z phase plates. (Figure 30). In this image, only the 0.8 nm fringes running diagonally across the image are resolved. Thus, 0.8 nm fringes occur in both orientations, just as 0.8 inverse nm reflections occur along c^* in both orientations. These reflections are real; they cannot be due to hexagonal 2:17 material, as this would not form a spot at 0.8 inverse nm along c^* in the $\langle 11\bar{2}0\rangle_{1:5}$ = $\langle 10\bar{1}0\rangle_{2:17}$ orientation.

To eliminate the streaking in the SAD's, an alloy was coarsened by overaging for 100 hours at 960 ^{o}C. The resulting microstructure was extremely coarsened, the 1:5 and 2:17 phases

having lost coherency and the Z phase plates having become up to 30 nm thick. An example of such a coarsened Z phase plate in a 1:5 matrix appears in Figure 31. The $\langle 11\bar{2}0\rangle_{1:5}$ SAD shows a pattern of weaker spots which can be indexed as a twinned rhombohedral phase having c~2.4 nm and a~0.5 nm. The reciprocal lattice of this phase is therefore very similar to the reciprocal lattice of the binary $SmCo_3$ phase (Figure 15) which has space group $R\bar{3}m$. The orientation relationship between the Z phase and the parent 1:5 phase is:

$$[0001]_{1:5} \;//\; [0001]_Z$$
$$[11\bar{2}0]_{1:5} \;//\; [11\bar{2}0]_Z$$

The spots in the pattern correspond to two twin-related variants; the faint line at the center of the image of the coarsened plate is presumably the twin interface. Some spot splitting in the higher orders in the SAD indicates that the a-axis parameter of the Z phase is smaller than that of the 1:5 phase. The c-axis parameter of the Z plate is also slightly smaller than six times the 1:5 c-axis parameter.

Microanalysis.

H_c depends on the chemical compositions of the individual phases as well as on their sizes and distributions. To truly characterize the system, it is necessary to know where the tran-

sition metal substituents, Fe, Cu, and Zr are situated in this three phase structure. A series of experiments using the microanalytical capabilities of a (scanning) transmission electron microscope were performed in an attempt to analyze the structure, or, at least, to detect partitioning of Cu, Fe, and Zr among the three phases.

The ideal of a complete quantitative analysis of the three phases had to be abandoned because the particles at peak aging are too small. The 1:5 cell walls are approximately 8 nm thick; the Z phase plates are approximately 2.4 nm thick. In principle, the nominally 4 nm electron probe in the Philips 400 (S)TEM should resolve the cell walls, but not the Z phase plates. In practice, not even the cell walls were resolved; no chemical segregation between the 1:5 and the 2:17 could be reproducibly detected. This was due to a number of experimental problems. In general it was impossible to be sure of accurate positioning of the probe on the cell walls. In most TEM images, the 1:5 cell walls are evidenced by the presence of strain contrast lobes which very often do not lie at the position of the cell wall itself. Lack of tilt capabilities in STEM/microanalysis configuration of the instrument prevents accurate determination of the relationship between image contrast and position of the cell wall, and, therefore, accurate probe placement. For thick areas of the foil, the beam broadens, considerably reducing resolution; but for thin areas of the foil, the cell structure is nearly invisible. Overall, there is generally a layer of ion-damaged material on the specimen surface. Finally, the characteristic x-

rays from Sm L lines lie in the same energy range as the K lines of Fe and Co, confusing the energy dispersive spectra. All these problems mitigated against accurate microanalytical characterization of the 1:5/2:17 cellular structures.

An alternate policy of simply establishing the tendencies of the system toward partitioning was adopted. A specimen was overaged, giving coarsened, incoherent, 1:5, 2:17, and Z phases. A micrograph of such a specimen appears in Figure 32. For a Z phase plate in a 2:17 matrix, it could be established that the Z phase is highly enriched in Zr with respect to the matrix. (Figure 33). Comparing the coarsened 1:5 with the coarsened 2:17, Cu was found to favor the 1:5 while the Fe went to the 2:17. (Figure 34). The Zr was also more highly concentrated in the 1:5 than in the 2:17 phase. These are qualitative trends; although quantitation would be possible for a coarsened alloy, it would not have any more impact for the understanding of the useful, peak coercivity magnets. Thus, quantitation was not attempted.

Comparisons and Correlations.

All the alloys studied have some common features, as described above, but the relative density of these features depends on composition and heat treatment. Many of the alloys whose intrinsic coercivity data appear in Figure 20 were examined in the TEM and several measurements were routinely made. The results of these measurements are summarized in Tables 2-5 and

certain aspects appear in Figures 35, 36, and 37. This data was measured and recorded in order to establish which microstructural features are critical for optimal intrinsic coercivity.

A review of the data in Table 2-5 and Figures 35, 36, and 37 quickly reveals several trends which are not obvious from an analysis of a single alloy. In general, magnets with 3% Zr have smaller cells (shorter wavelength modulations) than do the magnets with 1.5% Zr for similar thermal treatments. Since the 1:5 cell walls have nearly constant thickness for well-developed cellular structures, the 3% Zr alloys have a larger volume fraction of the 1:5 material. Furthermore, the 1:5 cell walls in the low Zr magnets are more often curved and more disordered than the walls in the high Zr magnets. Alloys of 3% Zr have more and thicker Z phase plates, but fewer twin interfaces than do the 1.5% Zr alloys. Step-aging does not change cell size nor Z phase density.

Attempts to correlate intrinsic coercivity with specific microstructural features have not been successful. When ${}_iH_c$ is plotted against cell size, Z phase spacing, or c/a ratio, as in Figures 35, 36, and 37, no simple correlation is obvious. The other microstructural parameters which might be expected to play a role in coercivity, such as the 1:5 cell wall thickness, or the angle of inclination of the 1:5 cell wall with the basal plane, are actually insensitive to heat treatment once the cell structure is established. These relatively constant features obviously can not explain the large changes in coercivity which can be obtained by effective thermal processing.

One feature which does have some relationship with coercivity is the density of the Z phase plates. Figure 38 is essentially a repeat of Figure 20 in which markers have been placed along the curves at the time when large numbers of Z plates nucleate. In three of the four cases, a large number of Z plates appears just before the rise in coercivity. These plates are Zr-enriched; the fact that they have some correlation with coercivity provides the connection between the Zr content, microstructure, and coercivity.

Origin of the Cellular Structure.

The 1:5/2:17 modulated structure originates in a complex nucleation and growth process; its uniformity is the result of several features specific to the system. The processing routines used to produce these two-phase magnets always involve a high temperature homogenize-and-quench treatment, followed by aging to develop the structure. Similar heat treatments performed in the course of this investigation show that the high temperature phase in these alloys is neither of those which exist at the 850 ^{o}C aging temperature. Instead, experiments indicate that the Zr-containing alloys transform to the hexagonal form of the 2:17 as they dissolve all the 1:5 at high temperatures. Thus, an allotropic phase transformation must occur in the parent 2:17 material as the temperature is raised to the solutionizing temperature. During quenching, there is a

driving force for the reverse transformation (from H2:17 to R2:17) as well as for the precipitation of excess Sm as 1:5. Neither transformation goes to completion during the quench; the quenched-in state is thus an unstable mixture of both forms of 2:17 with a supersaturation of 1:5. Subsequent thermal activation results in a cellular modulated structure by the simultaneous inhomogeneous shuffle transformation in the 2:17 and clustering of the excess Sm to form the 1:5 cell walls. The details of these processes will be presented in the next few paragraphs.

Alloys containing 0, 1.5, and 3 wt% Zr were solutionized and quenched from various temperatures (1060 $^{o}C<T<1235$ ^{o}C) in order to freeze-in the high temperature form of the alloy. The results of these homogenize-and-quench experiments are summarized in Table 6. For the Zr-containing alloys, it was easy to find a predominantly H2:17 structure. This was not achieved in the case of the Zr-free alloy. Repeated attempts to homogenize this alloy always resulted in a two-phase mixture of R2:17 and a long period superstructure of the R2:17. The 1:5 seemed to be completely dissolved, but the hexagonal form of the 2:17 was not observed at any temperature in this alloy.

Figure 39 shows an example of a Zr-containing (1.5 wt% Zr) alloy, homogenized at 1200 ^{o}C, and quenched. Figure 39, upper half, shows the usual, clean structure in a symmetric BF image; the only contrast in this image arises from bend and thickness variations in the field of view. The only indication that this is not a perfect, single phase material is the "texture" in the DF image (Figure 39b). The SAD pattern, enlarged and indexed in

Figure 40, is much more revealing. The overall pattern is H2:17 with streaking through the 2:17 reflections; the maximum streak intensity occurs at the R2:17 positions. The fact that the H2:17 reflections are discrete spots indicates that the bulk of the material is H2:17. Faulting of the H2:17 locally generates R2:17, thus, it is not surprising that the intensity maxima occur at the R2:17 positions.

Although the streaking in the SAD pattern is intense, it is very difficult to obtain adequate electron microscope images of the real space features causing the streaks. Only in certain DF configurations could these R2:17 platelets be imaged at all. Figure 39b is an example of such an image, taken using the portion of the streak at the R2:17 position; the specimen was tilted to enhance intensity at that position.

As indicated in Table 6, the 3 wt% Zr alloy behaved similarly. Homogenizing for one hour at 1194 ^{o}C and quenching also produced a faulted H2:17 structure.

At 850 ^{o}C, the familiar 1:5/2:17 cellular structure very quickly grows out of the faulted H2:17 material. Figure 41 shows an example of the 1.5 % Zr alloy, homogenized at 1200 ^{o}C for one hour, and aged at 850 ^{o}C for 20 minutes. Already, after only 20 minutes, the excess Sm has coalesced into a well-defined cellular pattern. The cell interiors, however, have not completely transformed to R2:17. Figure 42 shows the same area in various diffracting conditions; as usual, for g = $(0001)_{1:5}$, the twinning and faulting is in contrast. Evidence that some H2:17 still exists comes from the SAD (enlarged and indexed in Figure 43)

where the H2:17 spots are still distinct; the streaking has become much more concentrated at the R2:17 positions.

The same mechanism for the formation of the cellular structure operates in the case of the Zr-free alloy, but the details are different. Instead of forming a faulted H2:17 after quenching from high temperature, the alloy forms a long period modulation of the R2:17 structure. Figure 44 gives an example of such a structure; in this particular area of the foil, the stacking is completely modulated, but many faults occur. On the other hand, many regions of these foils showed two phases - the clean R2:17 as well as the modulated phase. Figure 45 shows two views of the same region of the foil, oriented along two different crystallographic poles. The broad band at the center of the lower image is R2:17 as indicated by the inset micro-diffraction pattern. As noted in Table 6, none of the attempts to homogenize the Zr-free alloy was successful; there was always a two-phase structure after quenching. It is not known if this is due to a two-phase region at high temperatures or if the time/temperature combination was not sufficient to allow complete homogenization. Nevertheless, even these two-phase structures were effective in producing the cellular morphology. Figure 46 shows a micrograph of a Zr-free alloy, aged at 1210 ^{o}C for 1 hour, quenched, and aged at 850 ^{o}C for 20 minutes. Figures 46B,C, and D are a series of DF's from the same area. In these images, the 1:5 strain contrast lobes seem to occur preferentially at faults and disruptions of the coarsely twinned R2:17; the particles are elongated along the matrix pyramid planes. Figure

47 is an image of a different region of the specimen; here the structure is completely modulated. It is believed that this arises from an area which was completely transformed to the long period structure at elevated temperatures. Quenching and aging caused a uniform transformation of the long period modulation into a new type of modulation - the cellular structure. Although this case is not so clear-cut, it must be concluded that phase transformations in the parent phase are responsible for the uniform precipitation of the 1:5 to form the cellular morphology.

The structure of the long period phase is a nearly periodic faulting/twinning of the R2:17 structure. The diffraction patterns corresponding to Figure 45 are enlarged and indexed in Figures 48 and 49. In Figure 48, the R2:17 reflections are accompanied by satellites which very rapidly reduce in intensity through higher orders. They are very faint at higher orders, but they do seem to fall at positions corresponding to a fourfold multiplication of the 1.2 nm R2:17 lattice parameter (an approximately 4.8 nm spacing). The fact that the intensity drops off with the order of the reflection indicates that the modulation is not a perfect 4.8 nm stacking. If that were true, it would generate spots of equal intensity along this line in reciprocal space; such a structure would properly be called a polytype. Instead, this long period phase seems to have much in common with what has been referred to as a crystal having "uniformly mixed" antiphase boundaries. [49,50] That is, twins occur in the R2:17 structure every 2, 3, 4, 5, or 6 unit cells in a random sequence such that the average twin is 4 unit cells

thick. Besides being a mixture of several different twin sizes, faults and disruptions commonly occur; they are evidenced by terminating fringes in Figure 44 and Figure 45b. The fact that this structural modulation is only a twinning of the 2:17 - that is, a quasi-periodic rearrangement in the pattern of stacking of mixed planes - is seen by examining the $\langle 11\bar{2}0\rangle_{1:5}$ SAD (Figure 50) and the corresponding image, Figure 46a. In this orientation, there is no evidence for the modulation except for extremely fine streaking along $[0001]^*$. This indicates that the basic 0.4 nm structural unit is not perturbed by the modulation in the stacking sequences. If the stacking modulation were accompanied by a corresponding compositional or strain modulation, it would be reflected in this pattern as a similar row of spots along $[0001]^*$. The faint streaking is the only indication of such a modulation; if it exists at all, it is surely a small effect. By combining the information in Figures 48 and 49, it is possible to construct a schematic diagram of the reciprocal structure of the long period phase (Figure 50). Alternatively, the long period may be represented by a stacking sequence of the type:

```
...CABCABCABCABABCABCABCACBACBACBACBACBACBABCABCABC...
          4          3          5          2
```

- a quasi-periodic rearrangement in the arrangement of the mixed planes.

A further confirmation of the structure of the long period phase is given in Figure 51. This figure presents the results of

a laser optical diffraction analysis of a micrograph taken from the long period phase. Using a single R2:17 reflection and its associated satellites, a DF image was formed; bright structure factor contrast is therefore expected from all regions of the specimen having that orientation variant. Because there is a quasi-periodic mixing of orientation variants, a quasi-periodic image results. Visual inspection of such an image hints at local variations in the fringe spacings. Using the micrograph as a diffraction grating for a 2 mm diameter He-Ne laser beam produced patterns of spots of various spacings. The best measurement of these laser reflections gives fringe spacings in the ratios of 1:3, 1:4, 1:4.5 and other poorly defined positions. This pattern of small rational numbers supports the idea that the long period structure is composed of blocks of R2:17, twinned almost regularly, such that the orientation repeats itself on an average of every 4.8 nm.

In all cases, the same mechanism of nucleation operates. The R2:17 is not stable at high temperatures and high excess Sm concentrations; it transforms to other forms at high temperatures. The resulting reverse structural transformation is accompanied by an expulsion of excess Sm from the 2:17 in the form of the cellular modulation.

Origin of the Z Phase Plates.

It is as yet impossible to give a complete description of the nucleation and growth of the Z phase plates, but their known characteristics can be presented and will serve to fuel speculation in the next section. The Z plates are very long, with extreme aspect ratios; only rarely were terminations encountered in the peak-aged alloys. They do not appear until the cell structure is developed; the actual time of their appearance seems to be controlled primarily by the Zr content of the alloy (see Figure 38). Once nucleated, they must grow very rapidly along the common basal planes to achieve such an extreme aspect ratio. Their density is not significantly affected by step-aging treatments; presumably they do not nucleate and grow significantly at temperatures below 850 ^{o}C.

The Z phase plates seem to be heterogeneously nucleated at interfaces. Figure 52 is a micrograph of a region of a 1.5 wt% Zr alloy, aged 40 hours at 850 ^{o}C in which a 1:5 particle appears to have lost coherency and thickened to several times its original size. Within the field of view, especially visible in the WB image (Figure 52b) are several Z phase plates which seem to terminate at the semicoherent 1:5/2:17 interface. These Z plates are associated with shifts in the images of the interfacial dislocations. Some plates proceed straight through the particle. One might speculate that these plates were present well before the particle began to lose coherency while the plates which terminate at the interface nucleated there.

Another example of heterogeneous nucleation of the Z phase appears in Figure 53. A discontinuously coarsened Z plate lies at a grain boundary in this image. It is semicoherent with the lower grain (inset microdiffraction pattern); the grain boundary lies roughly parallel to the basal plane of the lower grain at this point. Within the lower grain, but just adjacent to the boundary is a very high density of Z phase plates. It appears that the semicoherent interface between the grain boundary allotriomorph and the matrix is a much more efficient site for Z phase precipitation. The incoherent interface between the adjacent grain and the Z phase particle seems instead to have facilitated the discontinuous coarsening of the grain boundary particle, allowing it to consume the plates in the near vicinity of the grain boundary. In either side of the grain boundary, the 1:5/2:17 cellular structure does not seem to be affected; the cellular structure extends to the boundary. Thus the Z phase seems to nucleate and grow discontinuously at grain boundaries and interfaces of the continuously nucleated 1:5/2:17 cellular structure.

Summary of Results.

The structure of the $Sm(CoCuFeZr)_{7.4}$ permanent magnets is modulated in three dimensions due to two different types of precipitation. $Sm(CoCuFeZr)_5$ precipitates form a nearly periodic array of continuous films on the pyramid planes of the twinned rhombohedral $Sm_2(CoCuFeZr)_{17}$ matrix. The precipitates lie on crystallographically equivalent $\{10\bar{1}1\}_{2:17}$ planes, resulting in a three dimensional modulation in which rhomboid-shaped 2:17 particles are surrounded by thin walls of the 1:5 material. This is normally a totally coherent structure. After the 1:5/2:17 cellular modulations are developed, a third phase, the "Z" phase, precipitates as thin plates lying on the common basal planes. This phase is Zr-enriched; it has a reciprocal lattice similar to that of the rhombohedral $SmCo_3$ phase, and is coherent with the 1:5 and 2:17 phases. At advanced stages of precipitation, these thin plates occur regularly in the cellular structure, generating a quasi-periodic modulation along the common c-axis.

The sizes, distributions, and chemical compositions of these three phases in this multiply modulated microstructure are subject to manipulation by thermal processing. In general, the cellular structure coarsens uniformly during aging, but magnets with 3 wt% Zr have shorter wavelength modulations than do the 1.5 wt% Zr alloys for equal heat treatments. The high Zr magnets have more and thicker Z phase plates but fewer twin interfaces than do the low Zr magnets. Step-aging does not change the cell size nor the Z phase plate density. Due to differences in solubility

limits, Cu tends to segregate to the 1:5 phase. The 2:17 phase is enriched in Fe, and Zr is concentrated in the Z phase as well as in the 1:5 phase.

Analysis of the microstructures of various magnets reveals no single microstructural parameter which always correlates with coercivity. Zr additions aid coercivity, but only if the alloy is step-aged. In the majority of the cases, appearance of the Z phase plates in the microstructure accompanies a dramatic rise in coercivity. This is a clue to the development of coercivity, but since this behavior is not always observed, the presence of Z plates cannot by themselves be simply responsible for changes in intrinsic coercivity. Coercivity undoubtedly depends on several interacting parameters.

Homogenize-and-quench treatments show that the structure of the Zr-containing magnets at high temperatures is the hexagonal rather than the rhombohedral form of the 2:17. The 1:5 seems to dissolve completely in the H2:17 at high temperatures, as the as-quenched structures are very uniform. The as-quenched structures of the Zr-free alloy always shows a two-phase distribution of R2:17 and a quasi-periodically modulated R2:17. This long period structure serves the same purpose as the H2:17 structure; by eliminating excess Sm during reverse transformation to the R2:17, these high temperature structures indirectly generate the uniform 1:5/2:17 cellular structure.

DISCUSSION

In order to understand the relationships between composition, microstructure and coercivity for these two-phase magnets, one must consider the system as a whole. It is well established that intrinsic coercivity depends on domain wall pinning in these alloys, but no single microstructural feature has been identified which is universally well-correlated with coercivity. Instead, coercivity seems to depend on several parameters, all of which evolve continuously during heat treatment. Thus, to understand coercivity, it is necessary to be cognizant of the processes involved in microstructural development; in that mode, one can construct a fairly clear picture of how these alloys function.

In what follows, the development of the multiply modulated microstructure will be presented and the development of intrinsic coercivity will be discussed. The roles of Zr as well as the other substitutional elements will be clearly delineated. The concepts obtained from this investigation will be used to interpret coercivity data for related alloys; similar microstructures have recently been observed by other investigators; their results are in general agreement with the results of this investigation and add an air of generality to the present discussion. Finally, it must be remembered that SmCo magnets are basically a technological system; several directions for future research, as well as possible alloy improvements based on the

ideas derived from this work will conclude this discussion.

Microstructural Development.

As in all precipitation hardening systems, a two-phase structure evolves from some sequence of nucleation and growth processes. In this case there are two distinct nucleation processes: 1) 1:5 material in the form of cell walls is produced by the breakdown of the high temperature forms of 2:17 and 2) the Z phase plates nucleate in the well-developed cellular structure. Assuming the 1:5/2:17 cellular structure has nucleated (a situation found to be true in all alloys after very short 850 ^{o}C aging times), two further processes must occur before a high coercivity magnet is obtained. The cells must grow to a size which will allow effective domain wall pinning, and the transition elements, Cu, Fe, Co,and Zr must redistribute themselves among the three phases. While the same nucleation event seems to be common to all the alloys, the varying extents of growth and redistribution of the transition metals distinguishes the individual alloys.

This section begins with a discussion of the phase transformations leading to the nucleation events and then considers the growth of the cells and the Z phase plates. The twinning of the R2:17 is reconsidered. The final step in the development of a high coercivity microstructure is the redistribution of the transition metals on the two major phases; this subsection concludes with a discussion of these processes.

Nucleation of the Cellular Structure. Probably the most remarkable feature of these alloys is the persistence of the 1:5/2:17 cellular morphology. This useful structural modulation has been found to grow out of several different as-quenched structures. Each case is slightly different, but all as-quenched structures have three features in common. 1)They are all based on 2:17 stoichiometry, 2)they all have some degree of structural disorder, and 3)they are all supersaturated with Sm. Because the end product - the cellular morphology - is the same in all cases, it is probable that the common features of the as-quenched structures are essential for the production of the 1:5/2:17 modulation. This section will consider how these as-quenched structures transform to the useful, coherent cellular structure.

The common features of the as-quenched structures suggest two different mechanisms for the formation of the cellular modulations. The faulting and stacking disruptions in the 2:17 might serve as heterogeneous nucleation sites for the 1:5 precipitation; anisotropic growth of the 1:5 nuclei might then result in the cellular morphology. Alternatively, it is possible to consider the as-quenched structures as fundamentally unstable, driven far from equilibrium by the quench; the cellular structure might then result as the system struggles to regain equilibrium as efficiently as possible. The next few paragraphs consider what might have happened in the quench to generate the observed structures, then the experimental evidence concerning the above

transformation mechanisms will be discussed.

It is important to be certain that the as-quenched structures reflect the state of the material in equilibrium at the homogenization temperature and that the observed structures are not themselves products of some transformation. Secondly, the atomistics of the nucleation mechanism should be examined to see if there is any justification for the intuitively pleasing idea that defects in the 2:17 catalyze the 1:5. These subjects will be examined in the next few paragraphs.

Without doing a high temperature single crystal x-ray diffraction experiment, it is impossible to be absolutely certain that the 2:17 phase is hexagonal at high temperatures, but there are strong indications that this is the case. If any of the transformations in this system are of second or higher order, they might occur during quenching as they would need no discrete nucleation event. Alternatively, an athermal process such as a martensitic transformation might be responsible for the observed as-quenched structures. These possibilities must be considered briefly.

The possibility of a higher order transformation can be eliminated by systematically applying the Landau and Lifshitz symmetry rules [45,46] for second order transitions as well as noting some experimental observables. All reactions between the observed phases in this system are:

1:5 <——> H2:17, R2:17, long period phase

H2:17 <——> R2:17, long period phase

R2:17 <——> long period phase

It was noted in the introductory material that transitions between the 1:5 and the R2:17 can not be second order. In terms of Khachaturyan's [46] concept of static concentration waves, an ordering of dumbbell sites on a 1:5 structure to form R2:17 occurs by the increase in amplitude of concentration waves of the wave vector

$$1/3\langle 22\bar{4}1\rangle_{1:5}$$

Higher order transitions are forbidden if it is possible to form third-order invariants of these ordering vectors. That is, if three vectors of the type $1/3\langle 22\bar{4}1\rangle$ can be combined to form a fundamental 1:5 reciprocal lattice vector, no second order transitions can occur. For this case, an obvious third order invariant can be formed:

$$3(1/3)\langle 22\bar{4}1\rangle_{1:5} = \langle 22\bar{4}1\rangle_{1:5}$$

which is a fundamental 1:5 reciprocal lattice vector. Since this is the case, no higher order transitions can occur which effect this type of ordering. The same can be said for transitions between 1:5 and H2:17. The agrument is essentially the same. The ordering vectors for ordering on 1:5 to form H2:17 are:

$$1/3\langle 22\bar{4}0\rangle_{1:5} \text{ and } 1/3\langle 44\bar{8}3\rangle_{1:5}.$$

Forming third-order invariants:

$$(3)(1/3)\langle 22\bar{4}0\rangle_{1:5} = \langle 22\bar{4}0\rangle_{1:5}$$

$$(3)(1/3)\langle 44\bar{8}3\rangle_{1:5} = \langle 44\bar{8}3\rangle_{1:5}$$

Both products are obviously fundamental 1:5 reciprocal lattice vectors. Thus, symmetry precludes higher order transitions between these two phases. Second order reactions between 1:5 or R2:17 and the long period phase cannot be eliminated by symmetry arguments; the ordering vectors for the long period are slightly shifted from the special points [46]; integral multiples of these ordering vectors will not likely form fundamental reciprocal lattice vectors. However, both 1:5 and R2:17 have been observed coexisting with the long period phase (Figures 48 and 47, respectively); these experimental observations serve to preclude second order transitions for reactions involving these phases. Furthermore, the H2:17 and R2:17 have also been observed in contact; the same idea applies to transformations between these two. Lifshitz [45] has also noted that second order reactions in hexagonal systems change the volume of the unit cells by a factor of either 3 or 6; for H2:17 to R2:17 the factor is 1.5. The H2:17 to long period transition can also be dealt with on this score. Thus, there does not seem to be any possible second order transitions between any of these phases.

The experimental observations also do not support the possibility of a martensitic transformation as generating the H2:17 or long period structures. Such transformations normally

involve some homogeneous distortion of the lattice with or without an inhomogeneous shuffle of atoms on the lattice. No evidence of lattice distortion has been observed, neither as distortions in the diffraction patterns, nor as lattice strain contrast near interfaces of any martensitic packets. In fact, the constancy of the Co sublattice is a striking feature of both the long period structure and the H2:17/R2:17 as-quenched structures. The quasi-periodic twinning of the R2:17 to form the long period is strictly confined to the dumbbell/Sm sublattices; it must occur by inhomogeneous shuffling of the Sm atoms and the dumbbell Co pairs with no long range disruption of the Co framework. The smallest atomic jump distance associated with such a shuffle process is the Sm-Sm nearest neighbor distance (~ 0.5 nm); no fractional positions for the Sm atoms are allowed. Thus, it seems highly likely that the first impression is correct; H2:17 is stable at high temperatures and high Sm contents, and no phase transformations have started and gone to completion during the quench.

If it is accepted that the Zr-containing alloys are H2:17 at high temperatures, it must be agreed that they decompose to form R2:17 and 1:5 during quenching and aging. Two types of reaction paths are conceivable: 1) The H2:17 transforms by an inhomogeneous shuffle mechanism to the R2:17, followed by nucleation and growth of 1:5. 2) The 1:5 nucleates either as small, discrete regions of excess Sm atoms or as long-range compositional fluctuatiions on the H2:17 structure; the remaining near-stoichiometric regions between regions of excess Sm shuffle

from H2:17 to R2:17. Both processes are conceivable and have some basis in experiment. It is also possible that these processes happen simultaneously. Cooling rates and relative driving forces will probably dictate which reaction path is preferred, but they will be individually examined here.

Stoichiometric H2:17 can be transformed to R2:17 by the passage of $1/3\langle 11\bar{2}0\rangle_{1:5}$ dislocations through the lattice on alternating mixed planes. These dislocations are perfect 1:5 dislocations, but partial dislocations in the 2:17 lattices. In the 2:17's, this mechanism is analogous to the transformation of hcp elemental Co to fcc elemental Co by passage of Schockley partial dislocations. A schematic of this process appears in Figure 54. As sketched in the figure, such dislocations strain the lattice; they would be visible for certain diffraction conditions in TEM images. They are not observed.

Since there is no evidence for the dislocation mechanism of the H2:17 to R2:17 transformation, one must consider other possibilities. R2:17 could conceivably nucleate as a small, not necessarily planar, region of stacking disorder and grow in all directions by shuffle of Sm and dumbbell sites at its interface with the parent H2:17. This type of nucleation event might be expected to occur at translational antiphase boundaries of the H2:17 or at local regions of excess Sm in this nonstoichiometric alloy. If the alloy were stoichiometric, the R2:17 nuclei would grow until they impinged on each other, generating growth antiphase boundaries in the R2:17 material. However, these alloys are not stoichiometric; excess Sm must be ejected from the R2:17

by diffusion ahead of the interface. When these particles impinge, they remain separated by the 1:5 material (the excess Sm); the interfaces remain diffuse, and the cellular structure appears immediately.

The alternative reaction path involves clustering of Sm in H2:17, leaving depleted, near stoichiometric regions which are free to shuffle to form R2:17. Assuming that the excess Sm is truly dissolved in the H2:17 at high temperatures, quenching might cause non-equilibrium clustering of Sm, forming the SmCo equivalent of GP zones. Aging would then be expected to generate well-defined regions of 1:5 at the GP zones. If the undercooling during quenching is extreme, the system may reach the point of absolute instability with respect to finite fluctuations. At that point, the transformation would no longer be restricted to distinct nucleation sites, but would occur as a cooperative phenomenon, and the resulting anisotropic spinodal decomposition of the Sm and dumbbell sites on their sublattice into a cellular modulation would serve to generate areas enriched in Sm which could form 1:5 regions in the H2:17. The remaining H2:17 would shift to compositions nearer to exact stoichiometry; a small shuffle would generate R2:17. The 1:5 particles would again fall into their role as diffuse interfaces between the several R2:17 and H2:17 variants. In this case, the cell structure would also be observed, but it would be the manifestation of the instability of the system with respect to long-range compositional fluctuations.

The experimental evidence for these processes is somewhat

contradictory. The uniformity and persistence of the cellular modulations are strong points in favor of the spinodal mechanism. However, if such a cooperative phenomenon is operating, it must be occurring without regard for the distinction between H2:17 and R2:17. In other words, the long-range Sm concentration waves must be forming despite the fact that the fundamental structure alternates on a finer scale between the two forms of 2:17. This can be seen from the fact that that the as-quenched Zr-containing alloys show diffraction evidence of regions of R2:17 (Figures 39 and 40) well before a cellular structure appears. The presence of R2:17 this early in the process would seem to favor the first reaction path: H2:17 goes to R2:17, followed by precipitation of 1:5 at the interfaces. On the other hand, close examination of Figures 41 and 42 shows that some of the H2:17 remains after 20 minutes at 850 ^{o}C, even though the 1:5 is well partitioned into a cellular structure. The H2:17 platelets in the cell interiors are only slowly removed by aging at temperatures below 850 ^{o}C. These results favor the second proposed transformation path: Sm composition varies either locally or as long-range oscillations in such a way as to form 1:5 and the remaining material shuffles from H2:17 to R2:17.

A complete description of these transformations during quenching at rates and temperatures similar to those used here probably should involve a combination of the two reaction paths described above. There is a driving force for clustering of excess Sm and for transformation of H2:17 to R2:17, both of which are effected by diffusion of the same two species - the Sm atoms

and the Co dumbbells. The actual mechanism of diffusion of these species through the Co sublattice framework is not known, but it seems reasonable to expect that the atomic interchanges allowing the Sm to move into clusters could also result in rearrangement of the dumbbell sites. Thus, the two reaction paths could be expected to proceed simultaneously.

Regardless of which path is initiated first, experimental evidence suggests that the complete shuffle of H2:17 to R2:17 is the slower process. The 1:5 cell walls are well-formed long before the H2:17 disappears completely. Thus, one might suspect that the driving force for Sm clustering is much greater than that for rearrangement of the dumbbells.

The fact that the 1:5 cell walls form an extended interface at the R2:17 antiphase boundaries is reminiscent of phenomena expected near a tricritical point. [52,53] At such a special point, it is expected that the disordered phase should completely wet the antiphase boundaries of the ordered phase. Thus, the cellular structure which consists of disordered 1:5 on the antiphase boundaries of ordered 2:17 would be a thermodynamically equilibrated structure, and its persistence would be easily accounted for. However, neither theory nor experiment support such a view. Theoretically, a tricritical point must be disallowed because all higher order transitions have been excluded by symmetry arguments and experimental observations. Experimentally, the cell structure is observed to coarsen with thermal activation; it evidently is not an equilibrium structure. Thus, one must conclude that this is simply a system which accommodates

off-stoichiometry by precipitation at antiphase boundaries and that the cellular structure is only a transitional feature in a long, slow approach to an equilibrium two-phase structure.

Regardless of the actual nucleation mechanism, the pyramid habit of the 1:5 is probably the result of an attempt to minimize elastic misfit strain energy. Livingston and Martin [40] pointed out that the misfit between the two lattices, at least in the case of the binary SmCo, is lowest for pyramidal planes. The spacing between mixed planes along the c-axis is greater for the R2:17 than it is for the 1:5. On the other hand, the distance between the Sm sites in the basal planes is larger for the 1:5 than it is for the 2:17 compound. For these reasons, Livingston and Martin hypothesized that the least misfit would lie at an intermediate position - at a plane having its normal somewhere between the c-axis and the basal plane. The electron diffraction patterns obtained in the course of this investigation support this hypothesis; the relative misfits along the $[0001]^*$ and the $\langle 1\bar{1}00\rangle^*$ and $\langle 11\bar{2}0\rangle^*$ are as expected. Careful examination of the SAD's at higher order reflections does show an apparent spot splitting due to the two different lattice parameters for the $[0001]^*$ and $\langle 1\bar{1}00\rangle^*$ and $\langle 11\bar{2}0\rangle^*$ systematic rows. The $[1\bar{2}11]^*_{1:5}$ = $[2\bar{2}01]^*_{R2:17}$ systematic rows very nearly superimpose, indicating that the misfit between the corresponding planes in direct space is very low, as suggested by Livingston and Martin [40]. Thus, if the nucleation is by a spinodal mechanism, it seems reasonable to expect the concentration modulations to form in such a way as to minimize the elastic energy; in this case that would result in a

dominant Sm concentration wave vector oriented perpendicular to the pyramid planes of the structure. Alternatively, if the nucleation of 1:5 is discrete, occurring at heterogeneities, anisotropic growth along the pyramid planes would also be expected to generate the cellular structure.

Another factor which may favor the pyramidal habit is that the interface between the two phases in this configuration is, in a sense, simple. Figure 56 shows an idealized drawing of the cellular structure. The 1:5 cell walls have been inclined at 60 degrees to the basal plane; their thickness was arbitrarily chosen. The dumbbell sites have been arranged to suggest regions of both R2:17 orientational variants; translational variants also occur. In this orientation, the structure projects exactly; the next layer of dumbbell/Sm sites, either above or below the plane of the paper, would be exactly the same. (Cell walls would occur, lying on crystallographically equivalent pyramid planes; they would not project. However, they are related to the configuration of the drawing by symmetry operations, so they can be ignored for the present discussion.) Note that two types of 1:5/2:17 interface occur. One gives a smooth surface of dumbbell sites; the other gives a sawtooth shape in this idealization; presumably it would smooth out somewhat in a real alloy. The point is that the lattice mismatch is minimized in this configuration and there is a 50% chance that a smooth interface is generated. The combination of these two is the reason for the commonly observed 60 degree habit.

The transformation from the long period phase to the

cellular structure may also take place by the generation of long-range fluctuations far from equilibrium. However, in this case, a discrete mechanism is also simple to imagine. The mistakes in the stacking of the R2:17 units form a high density of what are locally orientation and translation antiphase boundaries. It is only reasonable to expect that excess Sm in solution would adsorb on such heterogeneities, creating small regions of 1:5 stoichiometry. As usual, anisotropic growth of these nuclei along pyramid planes is highly favored. The strongest evidence for the discrete, heterogeneous nucleation of the 1:5 appears in Figure 46 which shows many instances of small, isolated 1:5 particles, elongated along the usual pyramid habit plane; they have not yet coalesced to form the cellular modulations. After excess Sm is expelled from the long period material, the remaining twin interfaces are expected to slowly disappear by diffusional growth of individual R2:17 particles. This process is expected to be very slow as the interfaces surely have a low surface energy; some residual twinning persists throughout the aging treatments.

Growth of the Cellular Structure. The quasi-periodic cellular structure is a two-phase system with a large interfacial area per volume; as such, it is expected to coarsen if sufficient thermal activation is available. This is indeed true; the cellular structure does grow uniformly with time at 850 ^{o}C. The coarsening process occurs by the occasional elimination of individual segments of 1:5 material. This allows adjacent particles of 2:17 material to coalesce. The elimination of the

cell wall seems to go quickly once started; only occasionally was it observed that a segment of 1:5 extended into the center of the 2:17 cell interior. Upon coalescence, the 2:17 particles produce either a perfect match, a translational antiphase boundary, or a twin interface. Thus, new twins are continuously produced as the structure coarsens. The 1:5 cell walls seem to be eliminated randomly in such a way that the overall morphology is maintained.

Within experimental error, the growth of the average cell obeys the usual time$^{1/3}$ law for diffusional coarsening (Figure 57). The conventional Lifshitz-Slyozov-Wagner [54,55] theory of diffusional coarsening predicts that the average particle size should grow as:

$$r - r_o = kt^{1/3}$$

where: r is the average particle size

r_o is a constant

k is a rate constant having units of size/time$^{1/3}$

t is the time at temperature.

This expression is strictly valid for spherical particles in a liquid, but it has been shown to be reasonably predictive for several solid-state systems including Ni_3Al particles in Ni(Al), [44] Cu-rich precipitates in Fe, [56] and for several spinodally decomposing systems [57,58,59] as long as the growth rate is controlled by bulk diffusion and the coarsening is driven by the reduction in surface area. In this case, it is probably the

diffusion of Sm which limits the growth rate, as it is the nature of the Sm sublattice which determines the cell structure. The rate constant should be closely related to the diffusivity of Sm; the fact that Figure 56 shows two different slopes for two different Zr concentrations can therefore be taken to mean that Zr inhibits Sm diffusion. Because the LSW theory seems to be obeyed, it is reasonable to conclude that the growth of the modulated structure is driven by the reduction in the interfacial energy but limited by diffusion of Sm through the lattice.

The excellent agreement between the experimental results and the straight line for the 3% Zr alloy is probably somewhat fortuitous. For a given alloy, there is a significant distribution in cell sizes; no attempt has been made here to characterize the variability of the size distributions. The data used in Figure 56 is simply the best estimate of average size after a maximum number of measurements were made on each micrograph. Nevertheless, the confidence in the data for the 3% Zr alloys is much greater than that for the 1.5% Zr alloys. The 3% Zr alloys have much smaller, more regular cells, giving the possibility of more measurements with less spread in the data. The data for the 1.5% Zr alloy is much less reliable; the straight line has been drawn through these points primarily for comparison purposes. The larger cells in the 1.5% Zr alloys allowed fewer measurements for the same extent of electron transparent material. A larger variability in cell sizes and increased percentage of curved boundaries also contribute to uncertainty in the 1.5% Zr results. Measurements of average cell

size for the 1.5% Zr magnets varied by as much as ± 30 nm; for the 3% Zr magnet, the average measurement varied by ± 5 nm.

The growth of the cells continues until, at very long aging times, coherency begins to breakdown. For the 1.5% Zr alloy, this begins to be evident after 40 hours at 850 ^{o}C. The cells are approximately 180 nm in size at this point; the cell walls are 10 to 20 nm thick. Where coherency is lost, the mismatch energy no longer effectively maintains the pyramidal habit plane. The 1:5 particles begin to spheroidize, consuming neighboring cell walls in a process reminiscent of abnormal grain growth. Figure 52 shows an example of such an overaged 1:5 particle. Contrast analysis of the interfacial dislocations gives the result that the largest component of their Burgers vector is perpendicular to the c-axis. Thus, the mismatch accommodated by this dislocation wall is primarily in the a-direction.

The effect of Zr on the growth of the cells is evident from Figure 57: Zr inhibits cell growth. Because the diffusion of Sm is probably the limiting process in cell growth, Zr inhibits Sm diffusion. This could be due to some affinity between these elements which causes their diffusional motions to be correlated. Alternatively, it could be due to size considerations. The Zr atoms are much larger than the Co atoms (Zr atomic radius = 0.160 nm; Co atomic radius = 0.125 nm); if, as commonly assumed, Zr occupies Co sites, it probably causes some distortion of the lattice in the neighborhood of each Zr atom, giving less "free volume" and reduced Sm diffusivity. It is interesting to speculate about which Co site would be favored by the Zr atoms. As an

oversized atom, they might be expected to behave as excess Sm atoms do in the 1:5 lattice. At higher Sm compositions than 1:5 stoichiometry, Sm atoms tend to occupy the mixed plane Co sites. If there are enough Sm atoms, they order to form 1:3, 2:7, or 5:19 phases. One might guess then that this lattice best accommodates excess oversized atoms on the mixed plane Co sites. If this is so, and Zr atoms do tend to favor that site, their proximity to the Sm sites might well be cause for reduced Sm diffusion.

One might tentatively identify another role of Zr in the growth and development of the modulated microstructures. Zr seems to promote strict adherence to the pyramidal habit. In all cases, the 1.5% Zr alloys had more curved and disoriented cell walls than did the 3% Zr alloys. Following the hypothesis that minimal mismatch energy dictates the habit plane, Zr presumably promotes mismatch. That is, relatively speaking, Zr elongates the 2:17 c-axis while elongating the 1:5 a-axis. Both effects must be present at roughly equal magnitudes because the habit planes in both cases lie at 60° from the basal plane. Furthermore, there is no significant difference in c/a ratios between the two compositions.To generate the two different strains, Zr would probably occupy different sites in the 2 phases; the mixed plane Co site in the 1:5 and the Co plane site in the 2:17. This is a possibility, but no direct evidence for it is yet available. Alternately, if Zr occupies Co sites completely randomly, it is conceivable that anisotropies in the lattices may cause both of the above mentioned distortions to occur. In other words, Zr might be

well accommodated at a mixed plane Co site in 2:17, but may result in c-axis elongation when occupying a Co plane site; Zr at a mixed plane Co site in the 1:5 may cause a-axis elongation but be well accommodated when occupying a Co plane site in 1:5. Whatever the atomistic origin, Zr does seem to promote regularity of the cell structure.

The other important microstructural feature which develops during 850 ^{o}C isothermal anneals is the density of the Z phase plates. The presence of these features seems to be controlled simply by the quantity of Zr in the alloy; step-aging seems to have no effect on them. For the 3% Zr alloy, large numbers of the plates come into existence after approximately one hour at 850 ^{o}C. In the case of the 1.5% Zr alloys, the Z phase does not appear until later - at 6-10 hours aging. In all cases, the cell structure is developed before the Z phase appears. Once started, the density of the plates increases rapidly, quickly reaching a limiting density which is greater for the 3% Zr alloy than for the 1.5% Zr alloy. Presumably the Zr available to drive the precipitation reaction is consumed at this point. Up to the point where the cell structure loses coherency, there is no evidence of coalescence and diffusional coarsening of the plates. They seem to maintain their thin nature - one to three unit cells thick - until the breakdown of the cellular structure. They are not connected; for coarsening to occur, Zr would have to leave one plate, diffuse through the lattice, and nucleate and grow a ledge on the surface of an adjacent plate. Even with the 1:5/2:17 interfaces, such a reaction seems to be unlikely.

Nucleation and Growth of the Z Phase Plates. Before beginning a discussion of the nucleation and growth of the Z plates, it is necessary to indulge in some speculation about its structure. No complete structure determination has been done; even with extreme coarsening, the largest Z plates observed were only approximately 30 nm thick. To completely determine the locations of all the atoms in the Z phase lattice, a single crystal x-ray diffraction experiment would have to be done. At present, all that is known of the Z phase is that it has the same reciprocal lattice as $SmCo_3$, that it is enriched in Zr with respect to the bulk of these magnets, that the lattice parameters of Z are a~0.5 nm, and c~2.4 nm, and that it is coherent with both the 2:17 and the 1:5 along its broad faces. A reasonable guess about the Z phase structure is that it involves some sort of ordered substitution on the 1:5-type structure in such a way as to generate rhombohedral symmetry. If so, the substitutions must occur at Co sites; any ordering of the Sm/dumbbell sites would necessarily increase the a-axis parameter of Z beyond 0.5 nm as is the case for the 2:17's. The reciprocal correspondence with R1:3 suggests that Zr might order at the mixed plane Co sites as Sm does to form $SmCo_3$. To obtain a 2.4 nm c-axis parameter and rhombohedral symmetry, this substitutional ordering would have to occur at every other mixed plane, to generate an:

...A-B-C-A-B-C-A...

type stacking. (The "-" indicates a mixed plane having no substitution.) This relatively simple ordered substitution on the

1:5 would account for all the observations - the lattice parameters, the rhombohedral symmetry, and the Zr enrichment. The same type of ordering could also occur on the 2:17 lattice, making it possible for such a structure to occur in conjunction with both major phases.

Assuming the Z structure to be a single ordered substitution of Zr at mixed plane Co sites, gives reasonable agreement with the observed volume fractions of Z plates and the overall Zr concentration. For the 3% Zr alloy, aged 15 hours at 850 ^{o}C, and step-aged, Table 5 indicates that Z plates occur on the average of every 25 nm; if each plate is 1 unit cell thick, this would constitute 3 Zr atoms in a volume equivalent to 62.5 $SmCo_5$ primitive unit cells. A quick calculation:

(62.5 unit cells)(1 Sm atom per cell)(150.4 grams per Sm mole)
+(62.5 unit cells)(5 Co atom per cell)(58.93 grams per Co mole)
+(3 Zr atoms)(91.22 grams per mole Zr)
=28090 grams.

273 grams Zr/28090 grams total ≅ 1 wt% Zr in such a volume.

Correspondingly, for Z plates two unit cells thick, a similar volume would contain ~ 2 wt% Zr. If all Z plates were 3 unit cells thick, spaced every 25 nm, all the Zr (~ 3 wt%) would be consumed. The structure images (Figures 29 and 30) indicate that the Z plates are 1, 2, or 3 unit cells thick (3, 6, or 9 fringes, respectively). Thus, for such a structure, most but not all the

Zr is in the Z plates.

The Z structure discussed above is the simplest situation which would produce all experimental observations; other, more complicated structures are conceivable, but they would have to be closely related. Instead of simple one-for-one Zr substitution at mixed plane Co sites, it is possible that complexes of atoms are ordering. For example, one might imagine that three adjacent Co atoms - not necessarily in the same plane - might be replaced by two Zr atoms. These complexes could then order. Alternately, it is possible that Zr could form ordered substitutions on the Co planes which would produce the same rhombohedral cell. Other possibilities exist, but it is impossible to determine which one is the real Z structure without further experimentation.

Assuming a simple Zr substitution as suggested above, it is possible to make some guesses about the atomistics of Z phase nucleation. Recall that the misfit between the 1:5 and the 2:17 is largely perpendicular to the c-axis (Figure 52). Also recall that the interfaces between 1:5 and 2:17 are of two distinct types, "sawtooth" and "smooth". (Figure 55) Finally, note that the positions of Co atoms in the Co planes of $SmCo_3$ are not aligned along the c-axis; they shift by $1/3\langle 10\bar{1}0\rangle_{1:5} = 1/3\langle 10\bar{1}0\rangle_{1:3}$ from layer to layer. Now consider a sawtooth interface; from consideration of lattice parameters, the 2:17 teeth are in tension perpendicular to the c-axis. The notches are in compression. A state of shear should be present in the neighborhood of each tooth. This shear could be accommodated by basal plane slip; if the magnitude of the basal plane slip is

$1/3\langle 10\bar{1}0\rangle_{1:5} = 1/9\langle 11\bar{2}0\rangle_{2:17}$, the Co planes across the slipped region - the stacking fault - will be in the configuration of Co planes in the 1:3 and 2:7 structures. This type of slip is a partial dislocation in the 1:5 lattice as well as in the 2:17. It causes Sm/dumbbells to move to the mixed plane Co positions and Co atoms to move to the Sm/dumbbell sites. There is no reason why such a partial dislocation should not be glissile in the basal planes of both 1:5 and 2:17, but the energy of the associated stacking fault would be expected to be high. The energy of Sm atoms at Co sites (and Co atoms at Sm sites) might well be reduced if some Sm atoms are replaced by Zr atoms. If this replacement is sufficiently favorable, the fault energy would be reduced to the point that the partial dislocation could propagate further through the lattice, its growth rate being limited by the diffusion of Zr to the fault. The logical extension of such a process is a Zr-enriched planar defect extending completely across the grain. This would account for the extreme aspect ratios of the Z plates.

The only remaining detail of Z phase nucleation and growth to be dealt with is the finite thickness of the Z plates. The above mechanism would result in a zero-thickness Zr-enriched stacking fault and a shear of the lattice by $1/3\langle 10\bar{1}0\rangle_{1:5}$. To eliminate this shear, a triad of partial dislocations, $1/3[10\bar{1}0]$, $1/3[\bar{1}100]$, and $1/3[0\bar{1}10]$ would have to move through the lattice on parallel planes. This situation is reminiscent of the formation of gamma-prime plates in Al(Ag) alloys by the simultaneous propagation of a triad of Schockley partial

dislocations on alternating {111} planes with concomitant diffusion of Ag.[59,60] If a partial dislocation moved along every mixed plane in the 1:5 and 2:17 structures, the result would be a rhombohedral lattice with c~1.2 nm, a~0.5 nm. Instead, the Z phase lattice parameters require the partial dislocations in the triad to lie on alternating mixed planes. Propagation of this dislocation complex through the 1:5 and 2:17, with the requisite ordered substitutions of Zr would result in the observed plates and the observed fact that the terminations of Z plates do not result in extensive lattice strain contrast.

Through all of this structural speculation, the question remains as to why a phase similar to $SmCo_3$ forms rather than a phase like Sm_2Co_7 as would be expected by the binary SmCo phase diagram. (Figure 1) It should be stressed that the Z phase is not the 1:3 phase; it only has a similar reciprocal lattice. There is no reason to expect that the stoichiometry of Z is anything like 1:3. All indications support the hypothesis that Z is an ordering on the Co sites in both 1:5 and R2:17 phases, there is no reason to believe that the dumbbell sites have disappeared. Thus the ratio of Sm to Co sites (including whatever Co site has been substituted) is probably still in the range 1:5 to 1:8.5.

The eutectoid decomposition of $SmCo_5$ into Sm_2Co_7 and Sm_2Co_{17} seems to have played no role here. In any case, it would not normally be expected unless the aging were done at a lower ($T \lesssim 700$ ^{o}C) temperature.

A final question about the Z phase is why it chooses a structure resulting from the propagation of three nonparallel

partial dislocations on alternating mixed planes. Specifically, why is the Z phase c-parameter 2.4 nm rather than 1.2 nm (partial dislocations on every mixed plane) or 3.6 nm (partial dislocations on every third mixed plane)? Furthermore, why is the rhombohedral form chosen rather rather than an hexagonal form which would result from propagation of pairs of antiparallel partials on parallel planes? One might speculate that the answer to these questions lies in the nucleation processes; the c-axis spacing between adjacent sawteeth is 2.4 nm. However, no complete atomistic model comes to mind, so without mentioning questions of the theory of phase stability, these questions will simply have to remain unanswered.

Twinning. The final microstructural feature - the twinning of the R2:17 - does not seem to be noticeably affected by the 850 ^{o}C isothermal anneals. Within an individual cell, topological constraints would seem to render difficult any process which would eliminate the twins. This situation is related to the difficulty in eliminating growth antiphase boundaries in more conventional ordered alloys. This case is especially stable because the twins are low energy interfaces which are planar; there is no curvature to drive their migration. As cell growth occurs, cell walls are systematically removed, causing adjacent 2:17 particles to impinge and create new R2:17-R2:17 interfaces. Such an interface can be perfect; it can be a simple twin (two orientational variants in contact); it can be a translational variant interface; or it can be a combination orientation plus trans-

lation (which reduces to a simple twin) interface. All of these possibilities occur in the cells throughout all stages of growth; as cells coalesce, their density is maintained. No fundamental changes in alloy structure and/or properties should be expected due to the twins; their morphology is constant.

Redistribution of the Transition Metals. Given a well-developed cellular structure, there is no guarantee that the coercivity will be high. To have effective domain wall pinning, there must be some form of strong interaction between the domain walls and the cellular structure. The energy of the domain walls must be much lower in one position than at others. Since both 1:5 and 2:17 are ferromagnetic and have similar compositions and crystal structures, it is possible that the wall energy in each phase may be similar, giving very little pinning effect. Thus, there must be some mechanism which causes the two phases to have significantly different domain wall energies. In this system, that requirement is met by the presence of Cu, Fe, and Zr in the lattice.

The overaging experiments indicate that Fe partitions to the 2:17, Cu partitions to the 1:5 and Zr to the 1:5 and Z phase. The behavior of Fe and Cu is to be expected; Sm_2Fe_{17} and Sm_2Co_{17} form completely miscible systems, but there is no stable $SmFe_5$. On the other hand, $SmCu_5$ and $SmCo_5$ form completely miscible systems, but Cu has limited solubility in Sm_2Co_{17}. Furthermore, the partitioning trends are in agreement with several reports in the

literature. [34,35,38] Thus, even though the experimental evidence for partitioning in this system was obtained from an extremely coarsened specimen, there is confidence that the effect is real.

The partitioning was easily detectible in the 960 ^{o}C aged specimen; presumably the effect is enhanced at lower temperatures. Limits of solid solubility generally decrease as temperature decreases. The degree of segregation in an 850 ^{o}C annealed alloy would probably be greater; that of a 400 ^{o}C alloy might be nearly complete elimination of Fe from 1:5 and Cu from 2:17. However, no direct evidence for these hypotheses is currently available.

The speculations of the previous paragraphs provide the key to the understanding of the effects of step-aging on coercivity. While the cell sizes and morphologies and Z phase densities are not noticeably affected by step-aging, the coercivity can be increased dramatically. At 400 ^{o}C < T < 850 ^{o}C, the diffusion of Sm required for cell growth is probably extremely slow. However, that does not stop the motion of the Co, Cu, and Fe. The Co sublattices in these structures are relatively open; the Co planes are essentially close-packed planes in which 1/3 of the positions are vacant. To be sure, some of this free volume is occupied by the adjacent Sm or dumbbell sites, but there is still reason to believe that the Co, Cu, and Fe are free to move about with very little thermal activation. The Sm framework which is established at 850 ^{o}C remains nearly constant, but the transition metals move about freely on the framework. If the trend toward

more restricted solid solubility at lower temperatures is followed by this system, there is an increased driving force for the partitioning as T is lowered to 400 ^{o}C. Thus, the step-aging treatment drives Cu to the 1:5 and Fe to the 2:17, increasing their chemical and magnetic dissimilarity and consequently improving the pinning strength of the system. This explains the effect of step-aging on coercivity.

It has been pointed out that the nucleation of the Z phase plates occurs at the same time in the thermal treatment as the large rise in coercivity in three of the four cases studied; their role deserves some explanation. First of all, it is difficult to expect that the Z phase actually pins the domain walls. Because of anisotropy, the domain walls are expected to lie on planes parallel to the crystallographic c-axis; their migration must proceed perpendicular to their faces, i.e. perpendicular to the c-axis. The Z phase plates lie on basal planes; their configuration is such that the domain walls should cut them and move along them, rather than meeting them face-to-face. Thus, it is hard to imagine that they present any resistance to domain wall migration.

If the Z plates have no direct role in coercivity, their effect must be indirect (or the correlation is simply fortuitous). Arguing that coercivity depends on the degree of partitioning of Cu and Fe, it is possible that the Z plates serve as high diffusivity paths for the Cu, Fe, and Co. No direct evidence for this is available, but step-aging does seem to be much more effective if there are significant numbers of Z plates.

Conversely, it is possible to argue that the Z plates are, in a sense, detrimental. Once they have formed, the maximum coercivity always levels off, the coercivity of the 3% Zr alloy at a higher level than the coercivity of the 1.5% Zr alloy. This might well mean that Zr in the matrix is beneficial, but that Zr in the Z phase is ineffective, only slightly increasing the kinetics. The fact that the 3% Zr step-aged alloy is superior to the 1.5% step-aged alloy indicates that the density of Z phase plates is beneficial or that Zr in the lattice is beneficial. The former possibility is doubtful because of the poor quality of the 3% Zr non-step-aged alloy which has plenty of Z plates. The latter possibility may be correct because the residual level of Zr in the matrix of the 3% Zr alloy after depletion by Z phase precipitation is probably still higher than that of the 1.5% Zr alloy in the same condition. The corresponding degree of Cu and Fe partitioning will also be greater. One can only speculate about the coercivity of an alloy for which the Zr did not precipitate from solution.

The degree of chemical and magnetic dissimilarity of the two major phases is presumed to determine the magnitude of the domain wall pinning; it is desirable to put this hypothesis on a firmer theoretical basis. Many theories of domain wall pinning have been proposed starting with Kersten's [61] theory of the effects of a non-magnetic inclusion in a magnetic matrix. All subsequent theories have followed his lead in attempting to describe the energy of the domain walls as a function of position in the structure. Recent models for the SmCo system such as those of

Perkins et al. [62] and Paul [63,64,65,66] have become very elaborate. They could be reproduced here, but for the sake of argument, a simpler, more intuitive approach is sufficient.The energy of a domain wall per unit area in the continuum limit (very wide Bloch wall) [67] is:

$$e = 2(3.14)(KJS^2/a)^{1/2}$$

where K is the anisotropy constant

JS^2 is the exchange parameter

a is the crystal lattice parameter.

Although this expression is probably not valid for the SmCo system where high magnetocrystalline anisotropy gives very narrow domain walls, it can form a convenient framework for argument. It is reasonable to expect the energies in the 1:5 and in the 2:17 to be of similar magnitude. The exchange in 2:17 is stronger than in 1:5 as evidenced by higher M_s and T_c, but the anisotropy of 1:5 is known to be greater than that of the 2:17. Originally, it was thought that the wall energy of 1:5 should be much larger than that of 2:17 because the coercivity of binary 1:5 is higher than that of binary 2:17. [40] However, the fact that Cu segregates to 1:5 in the two-phase magnets contradicts this idea [38]. Cu is expected to decrease both the exchange and the anisotropy of the 1:5 phase. If the energy of the domain wall in 1:5 were higher, Cu additions would result in a trend in domain

wall energies toward that of the 2:17. If the two were in contact, coercivity would decrease with Cu content. Instead, the opposite is observed; Cu segregation to 1:5 drives coercivity up, indicating that the domain wall energy in 2:17 is always higher than in 1:5. The domain walls should therfore tend to lie in the 1:5 cell walls as sketched in Figure 57. Recent Lorentz electron microscope images support this idea [51].

Coercivity depends on the resistance of motion of magnetic domain walls. Thus, one must consider the positional gradient of the domain wall energy. Optimal pinning should occur for a high amplitude square wave in domain wall energy versus position. The results of this investigation suggest that this is essentially what is generated by step-aging these alloys.

Summary. A fairly clear picture of the microstructural aspects of coercivity is now available. Aging these five-component alloys at 850 ^{o}C results in continuous growth of the cellular structure by volume diffusional processes. This growth ultimately causes loss of coherency at the point where the cells are approximately 200 nm in size. The pyramidal habit is maintained in order to minimize elastic misfit energy between the two phases. The Zr tends to precipitate from solution, forming Z phase plates. It is not sufficient to simply grow the cells to optimal size (100 to 150 nm); the alloys must be step-aged (slow cooled) in order to allow the Cu and Fe to partition to the 1:5 and 2:17 phases respectively. The resulting nearly square wave in

domain wall energy as a function of position presents maximal resistance to domain wall propagation and correspondingly high coercivity.

Comparison to related alloys.

Because of space and time limitations, only a limited number of alloys and heat treatments have been examined microscopically. However, the understanding obtained from these few alloys can be well applied to a much larger class of alloys in a consistent manner. Figures 17,18,and 19 show the trends in coercivity as controlled by several compositional variables. These figures will be briefly discussed in terms of what is known about magnet microstructures.

Variable Sm Content. Figure 17 shows the effect of Sm content on coercivity for two different Cu concentrations (6 and 8 wt%). As usual, both isothermal aging at 850 ^{o}C, and isothermal aging at 850 ^{o}C plus step-aging, treatments have been considered. All isothermal aging treatments were for one hour duration. The compositions range from that of stoichiometric 2:17 [$Sm(Co_{69.4}Fe_{20.7}Cu_{7.3}Zr_{2.5})_{8.5}$ = 23 wt% Sm] to $Sm(Co_{68.8}Fe_{21.2}Cu_{7.4}Zr_{2.6})_{7.21}$ = 26.5 wt% Sm. The corresponding microstructures should range from clean R2:17 to a rather thick-walled cellular structure.

It is expected that a cellular structure will occur for all alloys containing more than 20 vol% 1:5 material, stoichiometry less than 1:7.8, Sm content more than 24.5 wt%. Since these are 3 wt% Zr alloys aged for only one hour at 850 ^{o}C, the cells will be relatively small - approximately 60 nm in size. Changing the Sm concentration will probably not significantly affect the cell sizes, but increased Sm will increase the volume fraction of 1:5, giving thicker cell walls.

The coercivity of the isothermally aged alloys in the low Sm (Sm < 25.5 wt%) regime is probably controlled by reverse domain nucleation. For the stoichiometric 2:17 this would be expected; there are no pinning centers. As Sm concentration is increased, 1:5 precipitates form, eventually resulting in a cellular structure. However, these precipitates are chemically and magnetically very similar to the parent 2:17 so they do not effectivelt pin the domain walls. They only result in a reduction in the energy of reverse domain nucleation as they disrupt the symmetry and the anisotropy energy of the parent phase. Thus, coercivity drops dramatically.

The role of Cu in the low Sm content isothermally aged alloys is somewhat obscure. Assuming that reverse domain nucleation controls coercivity, one expects a critical dependence on interfaces, as they are the points of least magneto-crystalline anisotropy. The action of Cu at such points is simply unknown at this time.

As the Sm content exceeds 25.5 wt%, the coercivity begins to be controlled by domain wall pinning. The reverse nucleation has

become easier than the propagation of the domain walls through the cellular structure. As the Sm content increases further, the volume fraction of the 1:5 increases, but the chemical compositions and magnetic properties of the two phases remain constant. In this regime, the effect of Cu is to slightly magnetically soften the 1:5 material with respect to the 2:17. Thus, increasing Cu concentration from 6 to 8 wt% increases the differences in the magnetic properties of the two phases, marginally increasing the coercivity of the 8 wt% Cu alloy over that of the 6 wt% Cu alloy.

The increase in coercivity with step-aging occurs for all Sm concentrations included in Figure 17. This can be readily attributed to increased effectiveness of domain wall pinning. As aging temperature decreases, the chemical differentiation of the 1:5 and 2:17 increases; the interaction of the domain walls with the two-phase structure increases and coercivity is enhanced.

For the stoichiometric 2:17 alloy (23 wt% Sm), there is a question as to whether or not wall pinning precipitates exist. If some precipitates are present, the enhanced coercivity is easily explained by the previous paragraph. If no precipitates exist, the coercivity is controlled by the difficulty of reverse domain nucleation. In that case, the enhancement of coercivity by step-aging would have to be attributed to some as yet unknown surface phenomena.

The effectiveness of step-aging of the two-phase alloys is limited by Cu content and 1:5 volume fraction. At 24.5 wt% Sm, the coercivities of the 6 and 8 wt% Cu alloys are equal. This

indicates that the relatively small volume fraction of 1:5 must be saturated with Cu. As Sm content increases, the volume fraction of the magnetically soft 1:5 phase increases, giving a slight decrease in coercivity but an increase in the capacity for Cu. The higher Cu content alloy begins to have an advantage. Ultimately, the 1:5 volume fraction reaches the point where there is insufficient Cu - even for the 8 wt% alloy; the coercivity begins to decrease at a faster rate as there is increased volume fraction of the soft phase, but decreased chemical differentiation between the two phases.

In all cases, the presence or absence of Z phase plates should have little relative effect. All alloys considered in Figure 17 are 3 wt% Zr alloys; they should all have essentially the same Z phase content.

The two loop squareness curves, $H_K/_iH_c$ (Figure 17, upper), seem to be dominated by the effects of coercivity. That is, the 8 wt% Cu alloy has a higher coercivity and a correspondingly larger denominator. Besides this simple inverse relationship, a small additional component may be due to the increased volume fraction of 1:5 in the 8 wt% Cu alloy. This could conceivably contribute a quicker initial demagnetization as it would be easier for a domain wall to make small movements before encountering the hard phase. This should be a small or negligible effect.

<u>Variable Fe Content</u>. Figure 18 shows the effect of Fe on coercivity for 25.5 wt% Sm alloys. Fe concentrations range from

15 to 25 wt%; alloys having 4 and 6 wt% Cu are included. All alloys have been isothermally aged for one hour at 850 ^{o}C; some have been subsequently step-aged.

The microstructures of all the alloys considered in Figure 18 should consist of a 60 nm cellular structure with 8 nm cell walls. For only one hour aging, there are probably very few Z phase plates; the 3 wt% Zr is in solution.

There is no dependence of coercivity on Fe content for the non-step-aged alloys. Evidently, the Fe is nearly random at 850 ^{o}C; it must be affecting the magnetic properties of the two phases equally; the domain wall pinning strength seems to be constant. Again, higher Cu content results in marginally higher coercivity; the 1:5 phase in the 6 wt% Cu alloy is presumably slightly softer than the 1:5 phase in the 4 wt% Cu alloy.

The effects of Cu content on the coercivity of step-aged alloys is dramatic. Evidently, the reduction in temperature during step-aging causes Fe to become "magnetically active", increasing the hardness of the 2:17. In this case, the term, "magnetically active" should relate to the magnetocrystalline anisotropy of the 2:17. As Callen [18] has pointed out, the $Sm_2(Co_{1-x}Fe_x)_{17}$ exhibits strongest axial anisotropy for intermediate ($0.05<x<0.5$; $3.6<$wt% Fe<37) Fe concentrations. The action of step-aging is to drive the Fe into the 2:17, increasing the anisotropy, causing the 2:17 to present a large barrier to domain wall migration. Assuming all the Fe is in the 2:17, and that all the alloys have a volume fraction of 2:17 of approximately 70%, an overall alloy composition of 20 wt% Fe corresponds to a 2:17

containing 29 wt% Fe. Thus the maximum in the coercivity curve corresponds to 2:17 compositions well inside Callen's range. There is therefore no objection to the hypothesis that Fe augments 2:17 anisotropy during step-aging.

Increasing the Cu content of the alloy causes the maximum value of coercivity to increase; it broadens the maximum and shifts it to slightly lower Fe concentrations. As usual, the increased coercivity can be attributed to the action of Cu to decrease the energy of a domain wall in 1:5, increasing the effective barrier to motion out of the 1:5. The shift in the maximum to lower Fe content may be due to slightly increased 1:5 volume fraction in the alloy; the correspondingly decreased 2:17 volume fraction requires less Fe to reach an optimum anisotropy. The broadness of the maximum is not well understood, but may be due to changes in the relative degrees of Fe and Cu partitioning between the two phases; in other words, the presence of Cu in the 1:5 may drive Fe to the 2:17, maintaining higher 2:17 over an extended composition range. Comparing these curves with those of Figure 20 indicates that coercivity can be increased still further (up to 25 kOe) by using still higher (8 wt%) Cu concentrations and aging for longer times.

<u>Variable Zr Content</u>. The effects of Zr concentration on coercivity, as presented in Figure 19, are easily interpretable. For only one hour of aging at 850 ^{o}C, there are few Z plates, except for alloys having very high Zr contents. The effects on coercivity as shown in Figure 19 are therefore expected to be

primarily due to Zr in solution. Zr in solution does increase the anisotropy of the 2:17 [6]; thus, the barrier to domain wall motion into the 2:17 is increased. Indirect evidence also indicates that Zr increases the chemical differentiation of the two major phases during step-aging. This results in remarkable coercivity gains for step-aged alloys, but no change for non-step-aged alloys. For very high Zr (3 wt%), Z phase plates begin to form as early as one hour into the aging; they deplete Zr from solution, causing a dropoff in coercivity.

The squareness curve follows accordingly. Zr increases 2:17 anisotropy, giving a rising curve. Ultimately, Zr forms Z plates, decreasing both H_K and ${}_iH_c$, causing their ratio to level off.

Summary. Although only two alloys have been characterized microscopically, the results seem to apply to a larger class of alloys. The fact that coercivity forms continuous functions of Sm Fe, and Zr content indicates that the same microstructural mechanisms operate over extended composition ranges; only the magnitude of individual parameters change from alloy to alloy. In retrospect, then, it does appear that the basic approach taken by this investigation, to analyze carefully a few alloys and hope to generalize, is confirmed to be valid; the results appear to have some generality.

Alloy Improvements.

SmCo is a practical, technological system; it has been examined in hopes that an understanding of its behavior might prove useful for proposing new approaches to alloy improvement. It is therefore appropriate to briefly discuss what can be done which would have a reasonable chance of resulting in improved magnets.

Improvements can fall into two catagories: 1)those designed to increase coercivity while maintaining high saturation magnetization, and 2)those designed to improve saturation magnetization at equivalent coercivity values. Either approach should improve $(BH)_{MAX}$. Coercivity improvements will involve some method of enhancing the effectiveness of domain wall pinning. Saturation improvements will attempt to minimize the fraction of magnetically disordered elements, Cu and Zr, or to lower the volume fraction of 1:5.

Coercivity Improvements. The simplest proposal to improve coercivity in these alloys was already suggested by Livingston and Martin [40] in 1977; it still has not been accomplished. Domain walls lie parallel to the c-axis in this material; the 1:5 cell walls lie at 30° to the c-axis. One would expect more effective pinning if the two were parallel. At first glance, this would not seem to be a large effect; thinking naively, the reduction in pinning with angle of the cell walls would probably be proportional to sin(90-x) where x is the angle between the domain

and cell wall normals (approximately 30°). In such a simple analysis, the pinning strength would be expected to be reduced to sin 60° = 87% of its original value. This is significant, but it is obviously not very large. However, on closer consideration, one realizes that the effect of the angle between the domain wall and the cell wall is probably much larger. Assuming the domain walls lie parallel to the c-axis, they must cross some 2:17 material; to minimize their total area in 2:17, they would be expected to facet along cell walls as shown in Figure 57. This faceting has been observed in Lorentz electron microscopy images. [51] In this configuration, migration of the cell walls will probably occur by a step or ledge mechanism (Figure 58). That is, instead of the entire wall being forced into the 2:17, a small segment can jump from one cell wall to another, reversing the magnetization of a single cell. Kinks moving along the ledge would move the domain wall across a row of cells. Thus, the steps in the domain wall can migrate one cell at a time. It is impossible to quantify the reduction in pinning strength associated with this ledge mechanism, but intuition says that such a process would probably result in a large reduction in pinning effectiveness; significant improvement would probably result from any shift of the cell walls toward the c-axis.

To shift the habit plane of the cell walls, it is necessary to shift the lattice parameters of the 1:5 and 2:17 such that there is little mismatch along the c-axis, but increased mismatch in the basal plane. Thus, if one could expand both lattice parameters of the 1:5 phase, the misfit along the c-axis in any

cellular structure would be decreased. The mismatch along the a-direction would be increased. The simplest approach to expand the lattice parameters is to substitute some of the light rare earth elements which have larger atomic radii for Sm. For example, consider the effect of Ce. Nesbitt and Wernick [2] list the lattice parameters for $CeCo_5$ and $SmCo_5$ as a=0.4922, c=0.4026, and a=0.5004, c=0.3971 nm respectively. Khan's [8] data for equivalent distances in Ce_2Co_{17} are a=0.4837, c=0.4069 nm; for Sm_2Co_{17}, they are a=0.4850, c=0.4077 nm. Assuming that lattice parameters for combinations of these phases are simply related to parameters of the simple binaries, one would expect that a cellular structure of $(SmCe)Co_5$ and $(SmCe)_2Co_{17}$ would have less misfit along the c-axis and that the cell walls would correspondingly lie nearer the c-azis. Substitutions for the transition metals might also be found which would promote a more desirable habit, but at this time it is impossible to predict which element would be effective. Nevertheless, Fidler et al. have found that Hf does increase the angle between the cell walls and the basal plane up to almost 70°. [68] This is some improvement; it is possible that even better alloys may be devised. However, substitutions of many elements will decrease M_s; each possibility will have to be tested experimentally to determine if benefits outweigh losses.

A second approach to coercivity improvement involves adjustment of the magnetic properties of the two major phases such that they are more dissimilar. The first impulse is to adjust Cu and Fe levels, but the data in Figures 17, 18, and 19

shows that they are probably very nearly optimized already. Step-aging to even lower temperatures might be marginally effective, but solubility limits usually approach zero asymptotically as temperature tends to zero, so one can not expect major improvements by this approach. Likewise, for the present heat treatment routines, Zr levels have also been optimized. Additions of any other element, whether rare earth or transition metal, would open up an entirely new Pandora's box of unknowns. It is impossible to predict what might happen; some other components have been tried, [1,68] but very little is known about what their role(s) may be. In any case, if forced to try other elements, the results of this investigation suggest that elements be considered which form 1) high M_s 2:17 phases, 2) high H_A 2:17 phases, and/or 3) low H_A 1:5 phases.

Even though Zr has been optimized for the standard TDK thermal processing routines, there is still hope for improvement by more effective use of this element. The results of this investigation suggest that Zr is much more effective for improving 2:17 anisotropy and for driving the partitioning of Fe and Cu if it remains in solution. It is probable that heat treatment schemes could be devised which would avoid Z phase precipitation. Although it would have to be experimentally verified, aging at slightly higher temperatures would probably not favor Z phase precipitation. Thus, after quenching, the alloys could be aged for 0.5-1.0 hour at 900 ^{o}C, then quenched to 600 ^{o}C, and step-aged to 400 ^{o}C to partition the Fe and Cu. The details would have to be optimized, but it is believed that such

a scheme might well generate high coercivity by retaining the Zr in solid solution.

Alternately, if it should prove absolutely impossible to retain Zr in solution, it might be good to resort to the use of a small amount of Ti, V, or Hf instead. These elements have been shown [69] to improve magnetocrystalline anisotropy of 2:17, although not so efficiently as Zr. If they can be retained in solution, the benefits may be greater than for the Zr which does not stay in solution.

Saturation Magnetization Improvements. The second approach to alloy improvement involves improving M_s without sacrificing H_c. In this composition range, that involves increasing the volume fraction of 2:17 as much as possible without losing the domain wall pinning of the 1:5. Shifting to lower Sm concentrations will increase the volume fraction 2:17 but may also result in loss of favorable continuous precipitation. Thus, the challenge is to find a way to minimize the 1:5 while maintaining effective pinning.

Ideally, an excellent permanent magnet would have a microstructure consisting of thin, continuous, but extremely well separated films of 1:5. These films would be enriched in Cu and would lie nearly parallel to the c-axis. The continuous films are necessary to minimize the demagnetization field associated with discrete particles. Thus, such a morphology would still pin domain walls, but its volume would be small enough to not significantly reduce the M_s of the overall alloy. The bulk of the alloy would be $Sm_2(Co_{70}Fe_{30})_{17}$; some Zr would be beneficial.

To produce a microstructure like that imagined in the previous paragraph, it would be necessary to begin with an alloy of overall stoichiomatry 1:8.0. Because of the smaller volume fraction of 1:5, this alloy would require less Cu (~3 wt%), but more Fe (~20 wt%). The Zr level would be nearly optimal at 3 wt%.

As usual, the heat treatment routine would have to begin with an homogenization step. Since this alloy is nearer to 2:17 stoichiometry, it is likely that homogenization will occur for 1150 $^{o}C<T<1225$ ^{o}C. The question remains as to whether this alloy will transform allotropically to H2:17 at these temperatures; this could only be answered experimentally. If the high temperature state is hexagonal, the usual 1:5 nucleation mechanism will operate; if not, extremely rapid quenches may be necessary to lead the homogeneous state to the point of absolute instability, which would also serve to nucleate 1:5.

To form a continuous 1:5 distribution from such a low volume fraction of 1:5 material, the aging sequences will have to be adjusted to cause maximal continuous nucleation rates followed by extensive growth. By aging the alloy at temperatures less than 850 ^{o}C (T~750 ^{o}C) for two hours, it should be possible to form a high density of 1:5 nuclei. Increasing the temperature to 900 ^{o}C will cause these discrete particles to grow; the usual pyramidal habit planes should develop as the discrete 1:5 particles grow and coalesce. If predictions are correct, a five hour treatment at 900 ^{o}C will result in connected films of 1:5, forming cells of 200-300 nm in size.

To develop the pinning strength of this structure, step-

aging to 400 ^{o}C will again be necessary. From the 900 ^{o}C aging temperature, cooling continuously at approximately 2 ^{o}C per minute until 400 ^{o}C and holding at that tempereture for 40 hours will probably result in sufficient Cu and Fe partitioning to generate a high coercivity alloy.

Obviously, the scheme outlined in the previous paragraph will have to be tested experimentally to determine if 1) a high coercivity magnet is produced and if 2) the microstructure is as designed. This scheme is simply a process with a good chance of success as suggested by the results of this investigation.

There may be many more means of producing improved SmCo-based permanent magnets; the approaches proposed here are only those directly suggested by the results of this investigation. There are many other elements and processing routines which could be tried, but there is at present no indication of how to predict their results, no indication of how to proceed with an efficient choice of elements or processes. The few design proposals presented here are necessarily not far removed from the alloys which have been characterized; they are in the regimes where predictions based on available experimental results can be expected to have some validity. They are simply the proposals which will most likely result in magnet improvement.

SUMMARY

A microstructural characterization of a series of $Sm(CoCuFeZr)_{7.4}$ permanent magnet alloys has shown that high intrinsic coercivity in these alloys depends on the interaction of magnetic domain walls with a continuously modulated structure of Cu-enriched $Sm(CoCuFeZr)_5$ (1:5) and Fe-enriched $Sm_2(CoCuFeZr)_{17}$ (2:17). The modulated structure has a "cellular" morphology of thin, continuous layers of 1:5 material lying on the pyramid planes of twinned rhombohedral 2:17. Aging of these alloys results in diffusional coarsening of this structure by repeated elimination of segments of 1:5 material. As the cell structure coarsens, a Zr-enriched phase having a structure similar to $SmCo_3$ precipitates in the form of thin plates lying on the common basal planes. Step-aging to lower temperatures allows the Cu and Fe to redistribute themselves on the modulated structures without any further growth of the average cell size. The resulting steep gradients in domain wall energy at the interphase interfaces gives a very large barrier to domain wall migration and, consequently, a large intrinsic coercivity.

The nucleation of the continuously modulated cellular structure is assisted by an allotropic transformation in the parent 2:17 material. During high temperature homogenization treatments, these alloys transform either to the hexagonal form of 2:17 or to a long period modulation, a nearly periodic twinning, of the

R2:17 as they dissolve all the 1:5 material. On quenching, there is a driving force for the reverse transformation to R2:17 as well as for the precipitation of 1:5. Both processes occur by the diffusional shuffling of Sm atoms and Co dumbbells without change in the Co sublattices. Given sufficient thermal activation, these processes result in the formation of small regions of R2:17 whose antiphase boundaries are coated with the 1:5 phase. This situation coarsens into the technologically useful cellular modulated structure.

The precipitation of the Zr-enriched Z phase plates during extended aging of the cellular structure probably occurs at the 1:5/2:17 interfaces where a state of shear is expected to develop due to mismatch between the two lattices. If this shear is accommodated by a partial dislocation, and Zr is added as an ordered substitution on the Co sites, the Z phase embryo is established. This embryo can then grow by the Zr diffusion limited propagation of three mutually annihilating partial dislocations on alternating mixed planes, generating a thin plate of a structure similar to $SmCo_3$. The mode of nucleation and propagation of the Z plates strongly favors an extreme aspect ratio; they are commonly one unit cell thick, extending completely across the matrix grains.

Zr has four metallurgical effects in these alloys. First of all, Zr tends to inhibit Sm diffusion; high Zr alloys have smaller cells for equal heat treatments. Secondly, if it is a minimization of elastic misfit strain energy which maintains the pyramidal habit of the 1:5 cell walls, Zr presumably enhances

misfit; the pyramidal habit of the 3 wt% Zr alloys is more rigorously maintained than that of the 1.5 wt% Zr aloys. The presence of Zr in the lattice must further reduce the solubility of Fe in 1:5 and Cu in 2:17 leading to increased compositional and magnetic differences between the two major phases; the coercivity, and presumably the wall pinning strength, of the 3 wt% Zr alloys is higher than that of the 1:5 wt% Zr alloys. Finally, Zr leads to the formation of the Z phase plates; the fact that they are observed to nucleate at the same time in the heat treatment cycle as when the alloys exhibit a dramatic rise in coercivity is attributed to their effects on the kinetics of Cu and Fe partitioning.

Data from other investigators indicate that the microstructural features observed in the alloys of this investigation are common to a wider class of alloys. Levels of substituents can be adjusted significantly, giving continuous curves in the magnetic property data. This data can be readily understood in terms of ideas derived from the study of the alloys in this investigation. Thus, this microstructural study seems to have some generality.

The careful analysis of the development of coercivity in these alloys readily provides suggestions for the design of improved alloys. In order to increase coercivity, the pinning strength of the two-phase structure should be enhanced, either by adjusting the lattice parameters to achieve a more favorable morphology or by adjusting the magnetic properties of the individual phases to augment their differences in domain wall

energy. An especially simple way to achieve this is by adjusting heat treatments such that the Zr is retained in supersaturated solid solution. Increases in M_s might be achieved by decreasing the volume fraction of 1:5 material; this would require a shift in Sm content and careful processing to retain the continuous decomposition product required for effective domain wall pinning. More radical approaches to magnet alloy design would entail changes in compositions and fabrication processes. By showing which compositions and structures are desirable, this investigation opens the door for many new approaches to the design of excellent permanent magnets in this system.

ACKNOWLEDGEMENTS

I gratefully those individuals who have been of assistance in the completion of this project. Thanks first of all go to Professor Gareth Thomas who supported and supervised this work, to Dr. Raja Mishra for his comments on this thesis and for many enlightening discussions during its development, and to Professors Didier deFontaine and Hans-Rudolf Wenk for their support and time, serving on my committees and inspecting the thesis.

T. Ojima and the staff at the Research and Development Laboratory, TDK Electronics Co., 2-15-7 Higashi Owada, Ichikawa, Chibaken, 272-01, Japan provided the alloys for this study as well as the magnetic coercivity data; their efforts are greatly appreciated. An Atlantic Richfield Foundation Fellowship supported me financially during a portion of this work; I am grateful for their assistance. Furthermore, this work was supported by the Director, Office of Energy Research, Office of Basic Energy Sciences, Division of the U. S. Department of Energy under Contract No. DE-AC03-76SF00098.

I'd also like to thank all the fellow graduate students for comradeship, assistance, and many stimulating, but not necessarily scientific, discussions. Special thanks go to Channing Ahn, R'Sue Caron, and Alan Pelton who have been very much more than just fellow graduate students. I also very much

appreciate the efforts of Tim Dinger who has recently assumed many responsibilities for equipment maintenance and administration around the laboratories in Hearst Mining Building. I must mention my apartment-mates, Jim Gebhardt and Lenny Summers. Jim put up with me for four years; need I say more? Lenny calmly tolerated piles of papers and scribblings around the apartment for the several months during which this thesis was being composed. Thanks to Don Jurica for doing his best to maintain a state of equilibrium around the electron microscope laboratory and to Karen Bean for her tips on the usage of the word processing equipment.

Thanks to my parents and family who got me started in school and have been supportive throughout my entire educational career.

And finally, a very personal note of gratitude goes to Bev Seidl.

REFERENCES

1. T. Ojima, S. Tomizawa, T. Yoneyama, T. Hori, IEEE Trans. Magn. MAG-13, 1317, (1977).

2. E. A. Nesbitt and J. H. Wernick, Rare Earth Permanent Magnets, (Academic Press, New York, 1973).

3. For a recent review, see: W. E. Wallace and K. S. V. L. Narasimhan in Science and Technology of Rare Earth Materials, E. C. Subbarao, and W. E. Wallace, eds., (Academic Press, New York, 1980).

4. K. P. Gupta, in Science and Technology of the Rare Earth Materials, E. C. Subbarao and W. E. Wallace, eds, (Academic Press, New York, 1980).

5. G. Asti and A. Deriu in Proceedings of the Sixth International Workshop on Rare Earth-Cobalt Permanent Magnets and Their Applications, J. Fidler, ed., (Druckerei Lischkar and Co., Vienna, 1982).

6. W. E. Wallace, H. Fujii, M. V. Satyanarayana, and S. Hirosawa, Proceedings of the Sixth International Workshop on Rare Earth-Cobalt Magnets and Their Applications, J. Fidler, ed.,(Druckerei Lischkar and Co., Vienna, 1982)

7. K. H. J. Buschow, J. the Less-Common Metals, 11, 204, (1966).

8. Y. Khan, Acta Cryst. B29, 2502, (1973).

9. L. S. Ramsdell, American Mineralogist 32, 64, (1947).

10. D. T. Cromer and C. E. Olsen, Acta Cryst. 12, 689, (1959).

11. D. T. Cromer and A. C. Larson, Acta Cryst. 12, 855, (1959).

12. Y. Khan, Acta Cryst. B30, 1533, (1974).

13. Y. Khan, Phys. Stat. Sol. A23, 425, (1974).

14. G. Van Tendeloo and S. Amelinckx, Acta Cryst. A30, 431, (1974).

15. G. Hoffer and K. Strnat, IEEE Trans. Magn. MAG-2, 487, (1966).

16. A. Menth, H. Nagel, and R. S. Perkins, Ann. Rev. Mat. Sci. 8, 21, (1978).

17. R. K. Mishra and G. Thomas, J. Appl. Phys. 49, 2067, (1978).

18. E. Callen, J. Appl. Phys. 53, 2367, (1982).

19. K. Inomata, Phys. Rev. B23, 2076, (1981).

20. J. Deportes, D. Givord, R. Lemaire, H. Nagai, and Y. T. Yang, J. the Less-Common Metals 44, 273, (1976).

21. R. S. Perkins, and S. Strassler, Phys. Rev. B15, 477, (1977).

22. C. W. Allen, D. L. Kuruzar, and A. E. Miller, IEEE Trans. Magn. MAG-10, 716, (1974).

23. F. Hofer, IEEE Trans. Magn. MAG-6, 221, (1970).

24. J. Fidler and P. Skalicky, Phys. Stat. Sol. A50, 73, (1978).

25. J. Fidler and P. Skalicky, Proceedings of the 38th Annual Meeting of EMSA, (Claitor's, Baton Rouge, 1980)p.190.

26. J. Fidler, H. Kirchmayr, and P. Skalicky, Phil. Mag. B43, 765, (1981).

27. J. Fidler and P. Skalicky, Phil. Mag. A44, 427, (1981).

28. J. G. Smeggil, P. Rao, J. D. Livingston, E. F. Koch, AIP Conf. Proc. 18, 1144, (1974).

29. J. Fidler, H. Kirchmayr, J. Wernisch, J. the Less-Common Metals, 71, 245, (1980).

30. J. D. Livingston, IEEE Trans. Magn. MAG-14, 668, (1978).

31. F. J. A. Den Broeder and K. H. J. Buschow, J. the Less-Common Metals 29, 65, (1972).

32. I. Nishida and M. Uehara, J. the Less-Common Metals 34, 285, (1974).

33. H. Nagel, A. J. Perry, and A. Menth, J. Appl. Phys. 47, 2666, (1976).

34. A. J. Perry, J. the Less-Common Metals, 51, 153, (1977).

35. H. Nagel and A. Menth, IEEE Trans. Magn. MAG-12, 959, (1976).

36. H. Nagel and A. Menth, IEEE Trans. Magn. MAG-14, 671, (1978).

37. T. Yoneyama, A. Fukuno, and T. Ojima, Proceedings of the Fourth International Conference on Rare Earth-Cobalt Magnets and Their Applications. (Hakone, Japan, May 1979)p.407.

38. H. Nagel, J. Appl. Phys. 50, 1026, (1979).

39. H. J. Leamy and M. L. Green, IEEE Trans. Magn. MAG-9, 205,

(1973).

40. J. D. Livingston and D. L. Martin, J. Appl. Phys. 48, 1350, (1977).

41. K. N. Melton and R. S. Perkins, J. Appl. Phys. 47, 2671, (1976).

42. K. N. Melton and H. Nagel, J. Appl. Phys. 48, 2608, (1977).

43. R. K. Mishra and G. Thomas, Proceedings of the Fourth International Workshop on Rare Earth-Cobalt Permanent Magnets and Their Applications, (Hakone, Japan, 1979) p.301.

44. A. J. Ardell and R. B. Nicholson, Acta Met. 14, 1295, (1966).

45. E. M. Lifshitz and L. P. Pitaevskii, Statistical Physics, 3rd ed. (Pergamon Press, Oxford, 1980) p.459ff.

46. A. G. Khachaturyan, Progress in Materials Science, 22, 35, (1978).

47. H. Zijlstra, IEEE Trans. Magn. MAG-14, 661, (1978).

48. R. K. Mishra, G. Thomas, T. Yoneyama, A. Fukuno, and T. Ojima, J. Appl. Phys. 52, 2517, (1981).

49. K. Fujiwara, J. Phys. Soc. Japan 12, 7, (1957).

50. G. Van Tendeloo and S. Amelinckx, Phys. Stat. Sol. A43, 553, (1977).

51. G. C. Hadjipanayis, Proceedings of the Sixth International Workshop on Rare Earth-Cobalt Permanent Magnets and Their Applications, J. Fidler, ed. (Druckerei Lischkar and Co., Vienna, 1982). p.609.

52. S. M. Allen and J. W. Cahn, Acta Met. 24, 425, (1976).

53. S. M. Allen, Proceedings of an International Conference on Solid-Solid Phase Transformations, H. I. Aaronson, D. E. Laughlin, R. F. Sekerka, and C. M. Wayman, eds. (TMS-AIME, Warrendale, PA, 1982) p.219.

54. I. M. Lifschitz and V. V. Slyozov, J. Phys. Chem. Solids 19, 35, (1961).

55. C. Wagner, Z. Elektrochem. 65, 581, (1961).

56. G. R. Speich and R. A. Oriani, Trans. TMS-AIME 233, 623, (1965).

57. A. J. Ardell, Acta Met. 20, 61, (1972).

58. R. Gronsky and G. Thomas, Acta Met. 23, 1163, (1975).

59. J. A. Hren and G. Thomas, Trans. TMS-AIME 227, 308, (1963).

60. C. Laird and H. I. Aaronson, Acta Met. 17, 505, (1969).

61. M. Kersten, Grundlagen der Theorie der Ferromagnetischen Hysterese und der Koerzitivkraft,(S. Hirzel, Leipzig; reprinted by J. W. Edwards, Ann Arbor, 1943).

62. R. S. Perkins, J. Bernasconi, and H. J. Weisman, J. Appl. Phys. 47, 2679, (1976).

63. D. I. Paul, J. Appl. Phys. 53, 2362, (1982).

64. D. I. Paul, J. Appl. Phys. 53, 1649, (1982).

65. R. Friedberg, and D. I. Paul, Phys. Rev. Lett. 34, 1234, (1975).

66. R. Friedberg, and D. I. Paul, Phys. Rev. Lett. 34, 1415, (1975).

67. C. Kittel, Introduction to Solid State Physics, Fifth ed., (J. Wiley and Sons, New York, 1976) p.488.

68. J. Fidler and P. Skalicky, J. Mag. and Mag. Mat. 27, 127, (1982).

69. M. V. Satyanarayana, H. Fujii, and W. E. Wallace, J. Appl. Phys. 53, 2374, (1982).

TABLE I

Fundamental Properties of $SmCo_5$ and Sm_2Co_{17} Phases

	$SmCo_5$ hexagonal	Sm_2Co_{17} rhombohedral	Sm_2Co_{17} hexagonal
Prototype Structure	$CaCu_5$	Th_2Zn_{17}	Th_2Ni_{17}
Lattice Parameters (nm)	a = 0.5004 c = 0.3971	a = 0.8401 c = 1.223	a = 0.836 c = 0.852
Space Group	P6/mmm	$R\bar{3}m$	$P6_3/mmc$
Curie Temperature	724 °C	920 °C	920 °C
Saturation Magnetization $4\pi M_s$	9650 G	12,000 G	12,000 G

TABLE 2

Microstructural Measurement Data
1.5 wt% Zr Alloys (Part 1)

Specimen Number	Composition & Heat Treatment	$_iH_c$ (kOe)	Cell Size (nm)	Wall Thickness (nm)	Twin Thickness (nm)
17	1 hr @ 850 °C	3.6	50		20
18	3 hrs @ 850 °C	3.6			
19	15 hrs @ 850 °C	5.2	150	10	20
41	40 hrs @ 850 °C	11.3	160	10	20
20	1 hr @ 850 °C + Stepaging	5.8			
42	3 hrs @ 850 °C + Stepaging	5.0			
43	15 hrs @ 850 °C + Stepaging	15.6	170	10	15
44	40 hrs @ 850 °C + Stepaging	13.6	180	10	30

TABLE 3

Microstructural Measurement Data
1.5 wt% Zr Alloys (Part 2)

Specimen Number	Composition & Heat Treatment	Z Phase Spacing (nm)	c/a $\langle 1\bar{1}00 \rangle$	c/a $\langle 11\bar{2}0 \rangle$
17	1 hr @ 850 °C	infinite	0.820	0.810
18	3 hrs @ 850 °C			
19	15 hrs @ 850 °C	12.5	0.848	0.846
41	40 hrs @ 850 °C	40	0.841	0.844
20	1 hr 850 °C + Stepaging			
42	3 hrs @ 850 °C + Stepaging			
43	15 hrs @ 850 °C + Stepaging	280	0.846	0.840
44	40 hrs @ 850 °C + Stepaging	40	0.833	0.828

TABLE 4

Microstructural Measurement Data
3.0 wt% Zr Alloys (Part 1)

Specimen Number	Composition & Heat Treatment	iHc (kOe)	Cell Size (nm)	Wall Thickness (nm)	Twin Thickness (nm)
13	1 hr @ 850 °C	0.9			
14	3 hrs @ 850 °C	2.25	60	5	22
15	15 hrs @ 850 °C	2.95	85	10	10
31	40 hrs @ 850 °C	4.20			
16	1 hr @ 850 °C + Stepaging	13.9	60	10	15
32	3 hrs @ 850 °C + Stepaging	24.0	65	?	?
33	15 hrs @ 850 °C + Stepaging	25.8	85	8	25
34	40 hrs @ 850 °C + Stepaging	25.8	95	?	?

TABLE 5

Microstructural Measurement Data
3.0 wt% Zr Alloys (Part 2)

Specimen Number	Composition & Heat Treatment	Z Phase Spacing (nm)	c/a $\langle 1\bar{1}00 \rangle$	c/a $\langle 11\bar{2}0 \rangle$
13	1 hr @ 850 °C			
14	3 hrs @ 850 °C	22.5	0.820	0.818
15	15 hrs @ 850 °C	20	0.847	0.840
31	40 hrs @ 850 °C			
16	1 hr @ 850 °C + Stepaging	167	0.831	0.830
32	3 hrs @ 850 °C + Stepaging	24	0.840	0.834
33	15 hrs @ 850 °C + Stepaging	25	0.831	0.835
34	40 hrs @ 850 °C + Stepaging	25	0.837	0.831

TABLE 6

Results of Homogenize-and-Quench Experiments

Alloy 1: 3 wt% Zr, 25.5 Sm, 15 Fe, 8 Cu, 48.5 wt% Co
$Sm(Co_{66}Fe_{21}Cu_{10}Zr_{2})_{7.4}$

Heat Treatment	Structure
1 hr @ 1194 °C	Homogenous H2:17
1 hr @ 1194 °C + 20 minutes @ 850 °C	Small, welldefined cellular structure

Alloy 2: 1.5 wt% Zr, 25.5 Sm, 15 Fe, 8 Cu, 50 wt% Co
$Sm(Co_{67}Fe_{21}Cu_{10}Zr_{1})_{7.4}$

Heat Treatment	Structure
1 hr @ 1140 °C	Coarsened Two-Phase Structure of R2:17 and 1:5
1 hr @ 1160 °C	Homogeneous H2:17
1 hr @ 1200 °C	Homogeneous H2:17
1 hr @ 1200 °C + 20 minutes @ 850 °C	Cellular Structure: R2:17 twinned; Some H2:17 in cells

TABLE 6
(continued)

Results of Homogenize-and-Quench Experiments

Alloy 3: 0 Zr, 25.5 Sm, 15 Fe, 8 Cu, 51.5 wt% Co
$Sm(Co_{69}Fe_{21}Cu_{10})_{7.5}$

Heat Treatment	Structure
1 hr @ 1210 °C	Long Period plus R2:17
1 hr @ 1217 °C	Long Period plus R2:17
1 hr @ 1222 °C	Long Period plus R2:17
1 hr @ 1210 °C + 20 minutes @ 850 °C	Long Period breaks up into cellular product
1 hr @ 1217 °C + 20 minutes @ 850 °C	Breakdown of long period occurs at faults

FIGURE CAPTIONS

Figure 1. SmCo Binary Phase Diagram. Note the presence of several intermetallics; especially note the fact that the $SmCo_5$ and Sm_2Co_{17} phases exhibit a large amount of mutual solid solubility at high temperatures. (Figure taken from Nesbitt and Wernick, reference 2.) XBL 834-9198

Figure 2. SmFe Binary Phase Diagram. Even though this system is similar to the SmCo system, there is no $SmFe_5$ phase. (Figure taken from Nesbitt and Wernick, reference 2.) XBL 834-9199

Figure 3. Perspective Drawing of the $SmCo_5$ Conventional Unit Cell. This is the basic structural unit of several of the SmCo intermetallic compounds. XBL 831-5004

Figure 4. Perspective Drawing of the Hexagonal Sm_2Co_{17} Primitive Unit Cell. This structure is formed by ordered substitution of dumbbell pairs of Co at one third of the Sm sites. The corresponding primitive cell of the $SmCo_5$ is outlined. XBL 831-5006

Figure 5. Perspective Drawing of the Rhombohedral Sm_2Co_{17} Primitive Unit Cell. This structure is also formed by an ordered substitution of pairs of Co atoms at Sm sites; the corresponding $SmCo_5$ primitive cell has again been outlined. XBL 831-5007

Figure 6. Plan Views of atomic Layers in the 2:17 Structures. The 2:17's are layered structures consisting of mixed Sm and Co planes (upper) alternating with pure Co planes (lower). The dumbbell sites form a hexagonal lattice in each mixed plane; stacking of mixed planes in ...ABAB... or ...ABCABC... patterns generate the H2:17 and R2:17 structures respectively. Note that the dumbbell and Sm sites lie directly above and below the vacancies in the Co planes (dashed outlines). XBL 834-5543

Figure 7. Schematic Drawings of the RCo_5, Hexagonal R_2Co_{17} and Rhombohedral R_2Co_{17} Structures. The essential features of these structures are shown by drawing this particular planar section. The 2:17 stacking sequences are clearly distinguishable; the pattern of dumbbell and Sm sites repeats into the plane of the paper. The Co planes are constant; they may be omitted.

XBL 834-5544

Figure 8. Schematic Drawings of Possible 2:17 Polytypes. Only the Sm and dumbbell Co sites have been sketched; the remaining Co sites would be constant throughout these structures.Because of their importance to this investigation, the two different orientation variants of the R2:17 (1R) structure have been sketched. XBL 834-5545

Figure 9. Schematic Drawing of Hexagonal RCo_3 Primitive Cell. The basic structural unit is like that of the 1:5 phase,

but rare earth atoms have been periodically substituted for mixed plane Co atoms. To accommodate these substitutions, the rare earth atoms shift slightly along the c-axis; the Co planes shift in the a-directions such that their vacancies provide maximum volume for the rare earth atoms. XBL 831-5009

Figure 10. Schematic Drawing of the Rhombohedral RCo_3 Primitive Unit Cell. See comments for Figure 9. XBL 831-5011

Figure 11. Schematic Drawing of the Hexagonal R_2Co_7 Primitive Unit Cell. See comments for Figure 9. XBL 831-5010

Figure 12. Schematic Drawing of the Rhombohedral R_2Co_7 Primitive Unit Cell. See comments for Figure 9. XBL 831-5012

Figure 13. Schematic Drawing of the Reciprocal Structures of the 1:5 and R2:17 Structures. XBL 832-5188

Figure 14. Schematic Drawing of the Reciprocal Structures of the 1:5 and H2:17 Structures. XBL 832-5187

Figure 15. Schematic Drawing of the Reciprocal Structures of the 1:5 and R1:3 Structures. XBL 832-5189

Figure 16. Schematic Drawings of Hysteresis Loops. The upper figure shows the concave-upward virgin magnetization curve and the square demagnetization curve of a magnet whose coercivity

is limited by the difficulty in nucleating reversed magnetic domains. The lower figure shows the concave-downward virgin magnetization curve as well as the relatively rounded shape of a domain wall pinning limited magnet. XBL 835-9800

Figure 17. Intrinsic Coercivity as a Function of Sm Content. The alloys whose data are presented here have been aged one hour at 850 ^{o}C, with and without step-aging. Besides Sm and Co, they contain 15 wt% Fe, 6 or 8 wt% Cu and 3 wt% Zr. The upper curves show the squareness of the two step-aged alloys; H_k is defined to be H at 0.9 B_R. XBL 8011-7429

Figure 18. Intrinsic Coercivity as a Function of Fe Content. The alloys whose data are presented here were also aged one hour at 850 ^{o}C, with and without step-aging. Besides Fe and Co, they contain 25.5 wt% Sm, 4 or 6 wt% Cu, and 3 wt% Zr. XBL 8011-7430

Figure 19. Intrinsic Coercivity as a Function of Zr Content. The alloys whose data appear here were also aged one hour at 850 ^{o}C, with and without step-aging. Besides Zr and Co, these alloys contain 25.5 wt% Sm, 15 wt% Fe, and 6 wt% Cu. XBL 8011-7432

Figure 20. Intrinsic Coercivity as a Function of Aging Time. Alloys containing 25.5 wt% Sm, 15 wt% Fe, 8 wt% Cu, 1.5 or 3 wt% Zr, remainder Co have been aged at 850 ^{o}C for time as indicated on the x-axis, and quenched. Some alloys have been subsequently step-aged. Note that the step-aging is always beneficial; high Zr

content is only beneficial if the alloy is step-aged.

XBL 8011-7418

Figure 21. Typical Image and SAD of Cellular Structure. The cell walls are imaged primarily due to strain contrast. The twins in the R2:17 are visible as bands of light and dark contrast perpendicular to the c-axis. The Z phase plates are the linear features running from upper left to lower right. The SAD and indexing are consistent with a combination of 1:5 and twinned rhombohedral 2:17 structures. The intense spots are common to all phases; the weaker spots are from the two variants of the R2:17, only one of which has been explicitly indexed. An extra spot at 0.8 inverse nanometers along $(0001)^*$ is the only distinct reflection from the Z phase.

(3 wt% Zr alloy; 1 hour at 850 ^{o}C; step-aged) XBB 819-9499

Figure 22. Image and SAD of 3 wt% Zr Alloy in a Symmetric $\langle 10\bar{1}0 \rangle_{1:5}$ Orientation. This is usually the most useful orientation for imaging these alloys. The 1:5 and 2:17 diffraction spots are separated and distinct (strong and weak reflections, respectively).

(3 wt% Zr alloy; 3 hours at 850 ^{o}C; step-aged) XBB 835-4361

Figure 23. Indexing of $\langle 10\bar{1}0 \rangle_{1:5}$ Diffraction Patterns. This schematic drawing indicates that the patterns generally encountered are made up of patterns from the 1:5, two variants of R2:17, and two variants of the Z phase. XBL 836-10124

Figure 24. Indexing of $\langle 11\bar{2}0\rangle_{1:5}$ Diffraction Patterns. This schematic drawing indicates that the patterns obtained in this orientation have the 1:5 and two R2:17 variants exactly superimposed; two variants of Z phase occur as distinct spots in this orientation. XBL 836-10123

Figure 25. Image and SAD of 3 wt% Zr Alloy in a Symmetric $\langle 11\bar{2}0\rangle_{1:5}$ Orientation. This is the same area of the foil as appears in Figure 22, but tilted 30° to the other high symmetry pole, as indexed in Figure 24.
(3 wt% Zr alloy; 3 hours at 850 °C; step-aged) XBB 835-4359

Figure 26. Image of a 3 wt% Zr Alloy taken along the C-axis. Imaging along the c-axis reveals a roughly hexagonal pattern of cell walls. The structure is not very regular, indicating that the pyramidal habit is not a rigidly-determined crystallographic feature.
(3 wt% Zr alloy; 24 hours at 850 °C; step-aged) XBB 8110-9523

Figure 27. Image of 1.5 wt% Zr Alloy, Oriented to Enhance Twin Contrast. By tilting such that one R2:17 variant is in a better orientation for strong diffraction, the structure factor contrast between the two is heightened.
(1.5 wt% Zr alloy; 15 hours at 850 °C; step-aged) XBB 812-1226

Figure 28. Bright Field and Dark Field Images of the Z

Phase. Near the $\langle 11\bar{2}0\rangle_{1:5}$ pole, the Z reflections appear as streaked spots; using the most intense area of the streak, the DF image of the Z phase was formed (lower image), indicating that the Z phase is definitely responsible for the streaking.
(3 wt% Zr alloy; 15 hours at 850 °C; step-aged) XBB 812-1225

Figure 29. Lattice Fringe Structure Image Along the $\langle 10\bar{1}0\rangle_{1:5}$ Pole. In this image, the Z plates appear as bands of 0.8 nm fringes running roughly vertically. The two variants of the R2:17 image as two sets of fringes (0.64 nm spacing) running roughly at 60° to the Z plates.
(3 wt% Zr alloy; 24 hours at 850 °C; step-aged) XBB 8111-10172

Figure 30. Lattice Fringe Structure Image Along the $\langle 11\bar{2}0\rangle_{1:5}$ Pole. In this orientation also, the Z phase plates appear as bands of 0.8 nm fringes. The matrix lattice has not been imaged.
(1.5 wt% Zr alloy; 40 hours at 850 °C) XBB 835-4360

Figure 31. Coarsened Z Phase Plate in the 1:5 Matrix. By aging an alloy at 960 °C for 100 hours, the microstructure was coarsened such that the Z plates were approximately 30 nm thick. This allowed a discrete SAD to be obtained; this pattern could then be indexed as in Figure 24.
(3 wt% Zr alloy; 100 hours at 960 °C) XBB 819-9500

Figure 32. Coarsened Microstructure of Overaged Alloy. The

1:5 regions of the overaged alloy have spheroidized, resulting in the morphology seen in this image. The particle at the center is 1:5 with several coarsened Z plates. Outside the incoherent interface is the R2:17 material. Microanalysis was easily accomplished on these microstructures.
(3 wt% Zr alloy; 100 hours at 960 ^{0}C) XBB 836-5064

Figure 33. Microanalysis of the Z Phase in the R2:17 Matrix. This figure shows typical energy dispersive x-ray spectra from the Z phase and the 2:17 phase of the coarsened alloy. The Zr is almost completely confined to the Z phase.
(3 wt% Zr alloy; 100 hours at 960 ^{o}C) XBL 8110-7168

Figure 34. Microanalysis of 1:5 and 2:17 of Overaged Alloy. By normalizing both spectra to the Co peak, it is seen that the 2:17 is enriched in Fe and the 1:5 is enriched in Cu.
(3 wt% Zr alloy; 100 hours at 960 ^{o}C) XBL 819-2062

Figure 35. Intrinsic Coercivity as a Function of Cell Size. By plotting coercivity data versus measured cell size for all alloys characterized, no simple correlation was found to exist.
XBL 835-9803

Figure 36. Intrinsic Coercivity as a Function of the Spacing of the Z Phase Plates. Here, as in Figure 35, no obvious correlation exists. XBL 835-9801

Figure 37. Intrinsic Coercivity as a Function of the c/a Ratio. Once more, no simple relationship is apparent.

XBL 835-9802

Figure 38. Intrinsic Coercivity as a Function of Aging Time and Z Phase Nucleation. This figure is almost a repeat of Figure 20 except that x's have been added to indicate at what time in the aging sequence the Z plates nucleate in large numbers. In three of four cases, the x occurs next to the dramatic rise in coercivity. XBL 809-5787

Figure 39. BF and DF of Homogenized-and-Quenched Alloy. The upper BF image shows what appears to be a clean, single-phase structure; the lower DF image using the streak shows the presence of some heterogeneities in the foil. The SAD indicates that this foil is almost completely H2:17.
(1.5 wt% Zr alloy; 1 hour at 1200 ^{o}C; quenched) XBB 8211-10201

Figure 40. SAD and Indexing of As-Quenched H2:17. This SAD, taken from the area of Figure 39 shows an H2:17 pattern with streaking through the R2:17 positions.
(1.5 wt% Zr alloy; 1 hour at 1200 ^{o}C; quenched) XBB 834-3274

Figure 41. BF and SAD of a Homogenized, Quenched, and Aged Specimen. After only 20 minutes at 850 ^{o}C, the H2:17 has broken down into a well-defined cellular structure. Note that some intensity remains at the H2:17 positions in the SAD.

(1.5 wt% Zr alloy; 1 hour at 1200 ^{o}C; quenched; 20 minutes at 850 ^{o}C) XBB 8211-10198

Figure 42. Homogenized, Quenched, and Aged Alloy in Several Diffraction Conditions. Note that extensive faulting of the 2:17 persists, as evident in the symmetric BF (upper) as well as in the g_{0001} BF (lower right).
(1.5 wt% Zr alloy; 1 hour at 1200 ^{o}C; Quenched; 20 minutes at 850 ^{o}C) XBB 8211-10197

Figure 43. SAD of Homogenized, Quenched, and Aged Specimen. Note that the H2:17 reflections are still distinct; but much more intensity is in the R2:17 positions than for the case of the as-quenched alloy.
(1.5 wt% Zr alloy; 1 hour at 1200 ^{o}C; quenched; 20 minutes at 850 ^{o}C) XBB 834 3272

Figure 44. Long Period Structure. This image is from an area of the Zr-free alloy which has completely transformed to the long period phase. The fringed contrast arises from the fact that several electron beams contribute to the image; it is almost impossible to exclude the 4.8 nm reflections by the use of an aperture. Note the presence of many interrruptions in the fringe pattern.
(Zr-free alloy; 1 hour at 1210 ^{o}C; quenched) XBB 8211-10199

Figure 45. Long Period/R2:17 Two-Phase Structure. These two

BF images are from the same area of the foil, but viewed along two different orientations (see inset SAD'S). The upper image, taken along $\langle 11\bar{2}0\rangle_{1:5}$ shows very little evidence of the complex stacking patterns of this material. The fringe contrast is obvious in the lower image, taken along $\langle 10\bar{1}0\rangle_{1:5}$. The long period structure is thus a quasi-periodic rearrangement in the stacking of R2:17 blocks. The inset microdiffraction pattern clearly indicates that the band across the image is clean R2:17 phase.

(Zr-free alloy; 1 hour at 1210 ^{o}C; quenched) XBB 8211-10200

Figure 46. BF, SAD, and 3 DF's of an Aged Long Period Structure. During aging, the long period breaks down by a coarsening of the R2:17; these coarsened R2:17 regions cause bands of intensity in the DF images (C,D) of the two R2:17 variants. The DF image of the matrix reflection (B) shows the presence of many regions of lattice strain; these regions surround 1:5 precipitates. By the shape of the precipitates, it is apparent that they are beginning to grow along the R2:17 pyramid planes.

(Zr-free alloy; 1 hour at 1210 ^{o}C; quenched; 20 minutes at 850 ^{o}C) XBB 836-5066

Figure 47. BF of Aged Long Period Structure. This region must have been completely transformed to the long period phase - like that of Figure 45 - as the resulting cellular structure is very regular.

(Zr-free alloy; 1 hour at 1210 ^{o}C; quenched; 20 minutes at 850 ^{o}C) XBB 836-5063

Figure 48. SAD and Indexing from Long Period Phase, $\langle 11\bar{2}0\rangle_{1:5}$ Orientation. Along this pole, the only evidence of the stacking modulation is the presence of very faint streaking along $(0001)^*$. The fundamental 1:5-type structural unit does not appear to be changed.
(Zr-free alloy; 1 hour at 1210 ^{o}C; quenched) XBB 834-3275

Figure 49. SAD and Indexing from the Long Period Phase, $\langle 10\bar{1}0\rangle_{1:5}$ Orientation. Along this pole, a regular sequence of reflections occurs parallel to $(0001)^*$ passing through the 2:17 positions. Because the intensity of the reflections drops dramatically with the order of the reflection, one must conclude that this is not a regular polytypic structure.
(Zr-free alloy; 1 hour at 1210 ^{o}C; quenched) XBB 834-3273

Figure 50. Reciprocal Structures of the 1:5, the R2:17, and the Long Period Phases. Only the first-order satellites on the R2:17 reflections have been sketched; higher-order satellites are much weaker. XBL 832-5190

Figure 51. Laser Diffraction Study of a DF Micrograph of the Long Period Phase. Laser diffraction was used to measure fringe spacings in a DF image. Several diffraction patterns, taken from several areas of the DF micrograph, indicate that the fringes

tend to have wavelengths in the ratios of 3:4:4.5. This supports the hypothesis that the long period structure is composed of alternating R2:17 twins with an average twin spacing of 4 R2:17 unit cells. The two figures at the upper left are the symmetric BF and DF images of the long period structure. The SAD taken from this area of the specimen appears in the third figure of the left column; the region of reciprocal space used to from the DF image is outlined in white. The lower left figure is a diffraction pattern formed by a laser beam passing through the negative of the DF image. It should essentially reproduce the intensity distribution in reciprocal space as outlined in the electron diffraction pattern. The right hand column are the results of several laser diffraction patterns taken with a collimated (~2 mm) beam passing through the DF micrograph. The spacing of the spots is inversely proportional to the spacing of the fringes in the DF image. By moving the beam, various fringe spacings could be detected; their wavelengths tend to occur as ratios of rational numbers.

(Zr-free alloy; 1 hour at 1210 ^{o}C; quenched) XBB 836-5065

Figure 52. BF and WB images of a 1:5 Cell Wall which has Lost Coherency. The fact that several Z plates terminate at the 1:5/R2:17 interface indicates that that is a preferred nucleation site.

(1.5 wt% Zr alloy; 40 hours at 850 ^{o}C) XBB 835-4362

Figure 53. Z Phase Grain Boundary Allotriomorph. This Z

phase particle seems to have nucleated at a grain boundary and coarsened discontinuously, depleting Z phase from the upper grain. Note that the 1:5 cell walls proceed completely up to the grain boundary.

(3 wt% Zr alloy; 3 hours at 850 ^{o}C) XBB 835-4364

Figure 54. Schematic Drawing of a Dislocation Mechanism for the H2:17 to R2:17 Transformation. By passage of a partial dislocation through the lattice, a thin region of R2:17 is created. XBL 826-5878

Figure 55. Schematic Drawing of the Cellular Structure. Following the pattern of Figures 7 and 8, a schematic drawing of the relationships between phases in a typical cellular structure can be constructed. The relative positions of the Sm and dumb-bell Co sites have been indicated. Note that two types of interfaces between 1:5 and 2:17 occur - a smooth interface and a sawtooth interface. R2:17 twin interfaces are indicated by horizontal dashed lines. XBL 834-9246

Figure 56. Cell Size as a Function of the Cube Root of Time. This figure illustrates that, within the experimental error, the coarsening of the cellular structure follows the Lifshitz-Slyozov-Wagner diffusional coarsening law. XBL 836-10122

Figure 57. Schematic Drawing of a Domain Wall in the Cellular Structure. Due to the lower energy of a domain wall in

the 1:5 phase, it would be expected to facet to follow the cell wall as much as possible. XBL 836-10121

Figure 58. Schematic Drawing of a Step Mechanism for Domain Wall Migration. Because of the configurations of domain walls and cell walls, it would seem to be energetically favorable for the domain wall to migrate by steps, reversing the magnetization of 2:17 cells, one at a time. XBL 836-10120

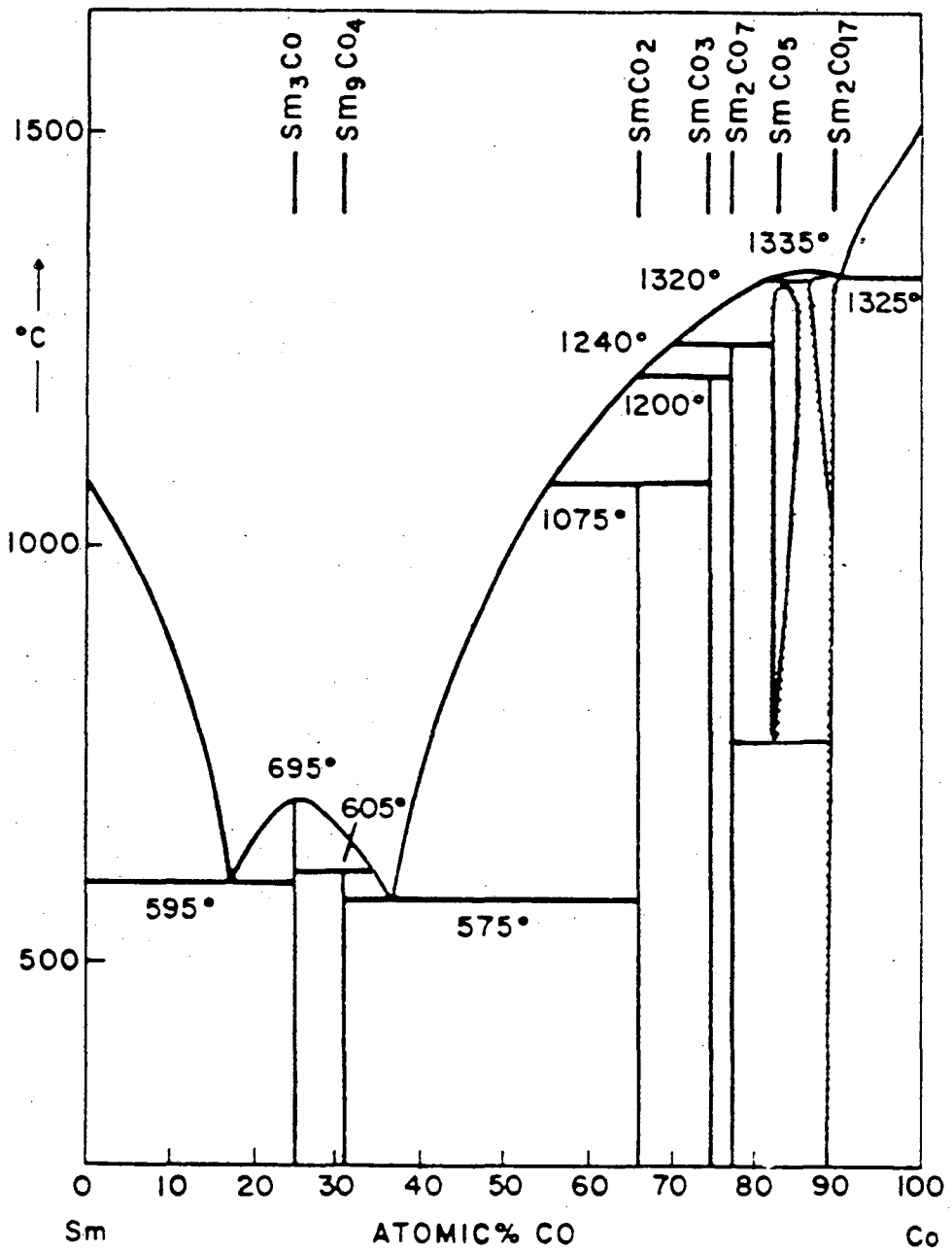
Sm3Co
Sm9Co4
SmCo2
SmCo3
Sm2Co7
SmCo5
Sm2Co17
1500
1000
500
°C
1335°
1320°
1325°
1240°
1200°
1075°
695°
605°
595°
575°
0
10
20
30
40
50
60
70
80
90
100
Sm
ATOMIC% CO
Co
XBL 834-9198

FIGURE 1

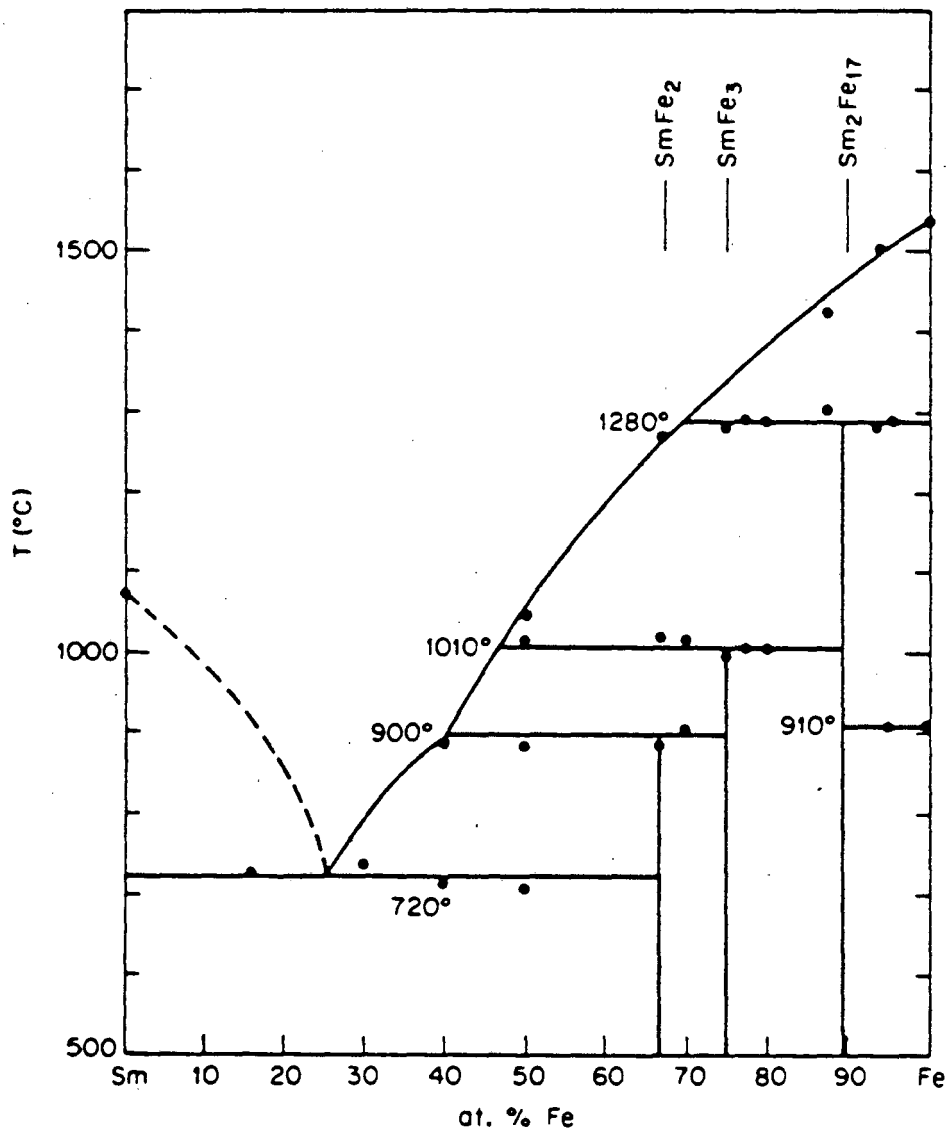

XBL 834-9199

FIGURE 2

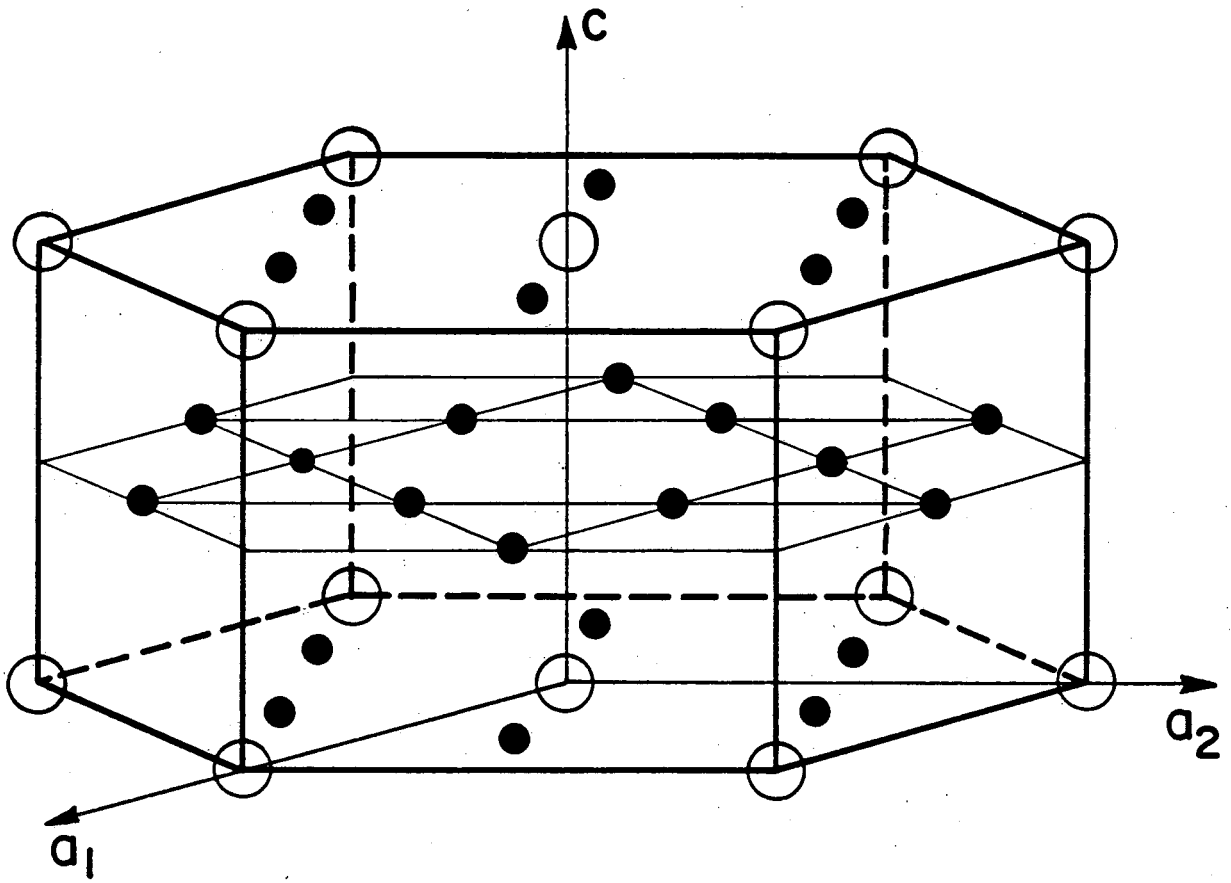

$SmCo_5$ Conventional Unit Cell
(Perspective Drawing)

○ Sm
● Co

XBL 831-5004

FIGURE 3

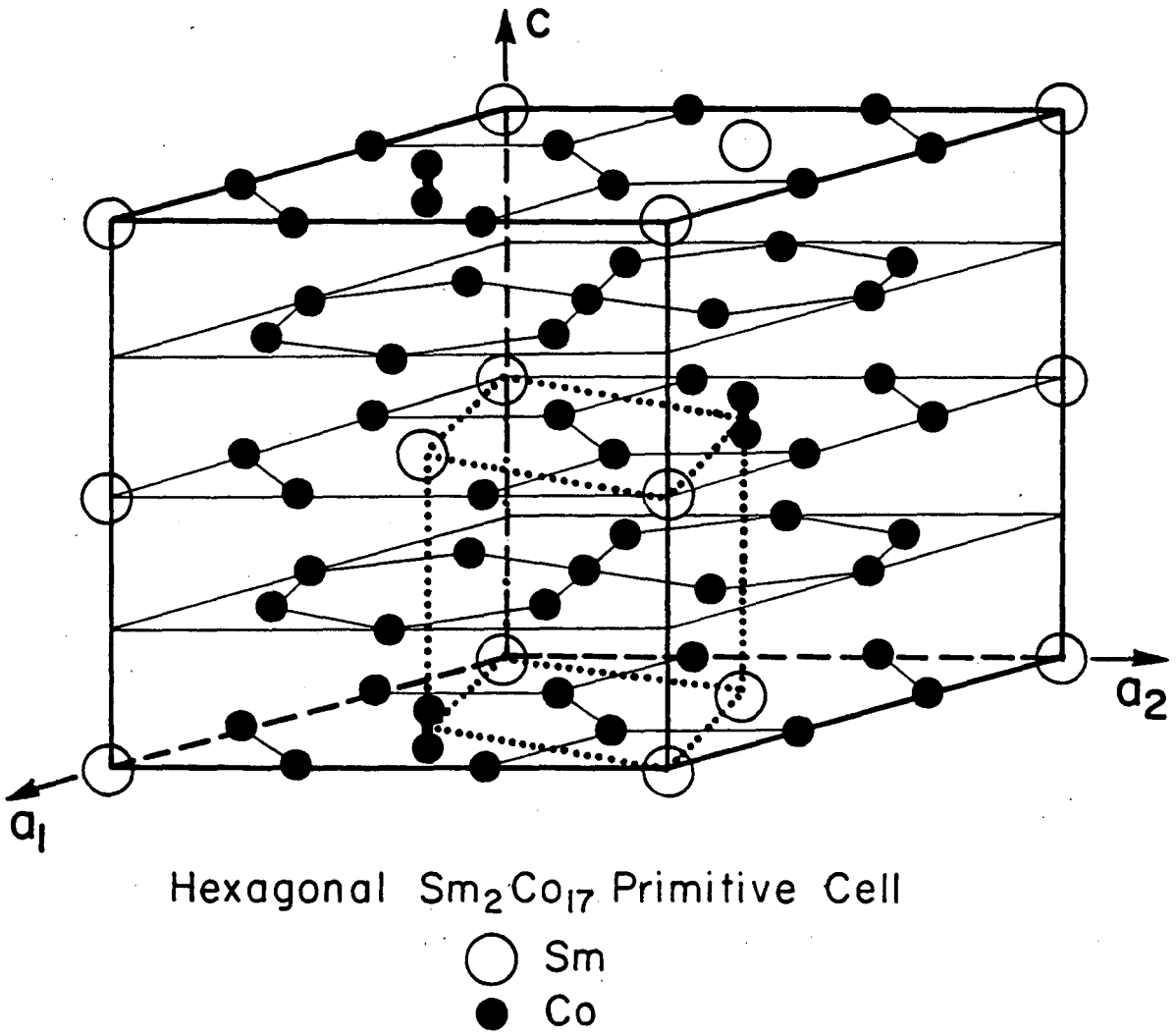

FIGURE 4

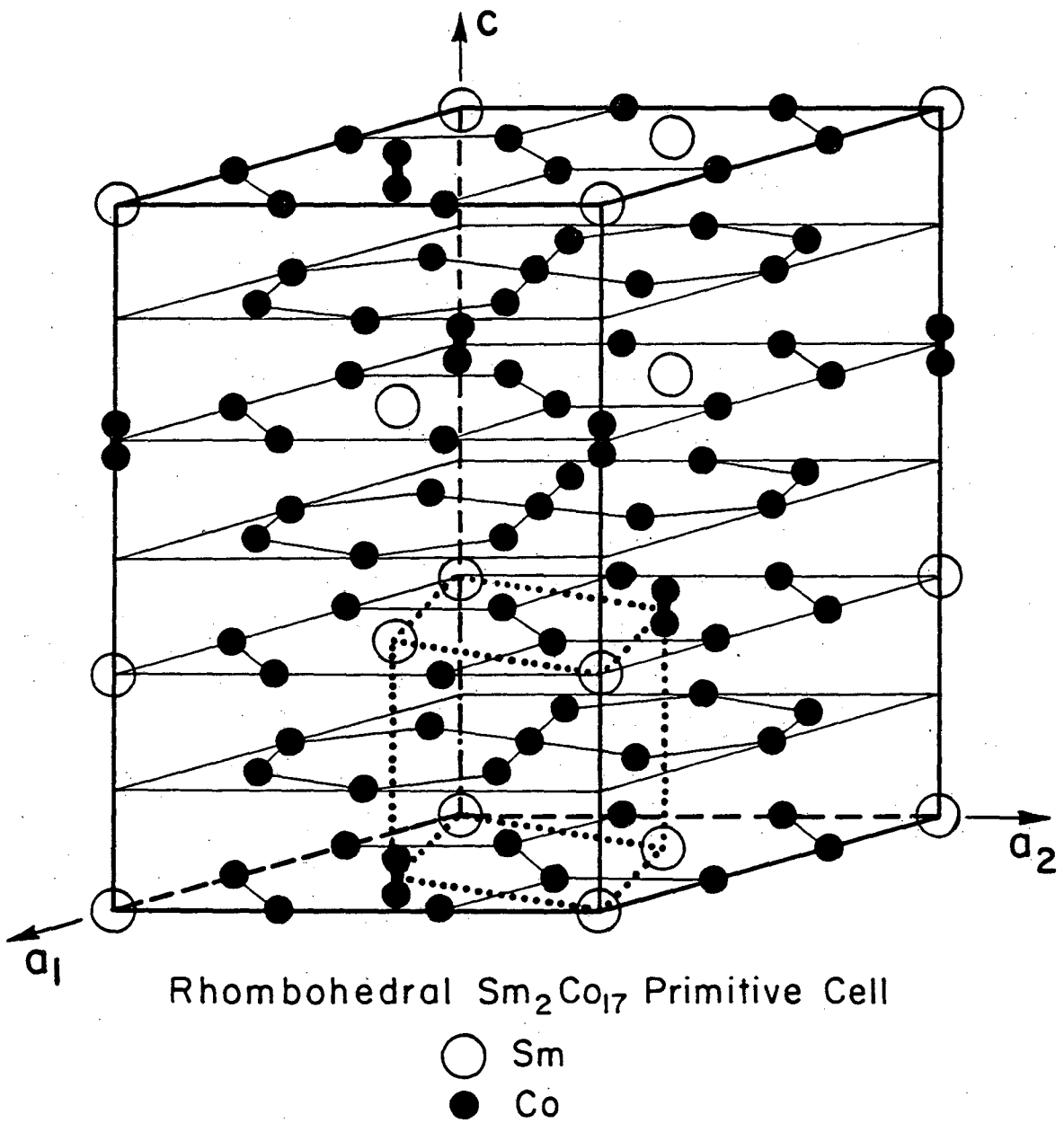

XBL 831-5007

FIGURE 5

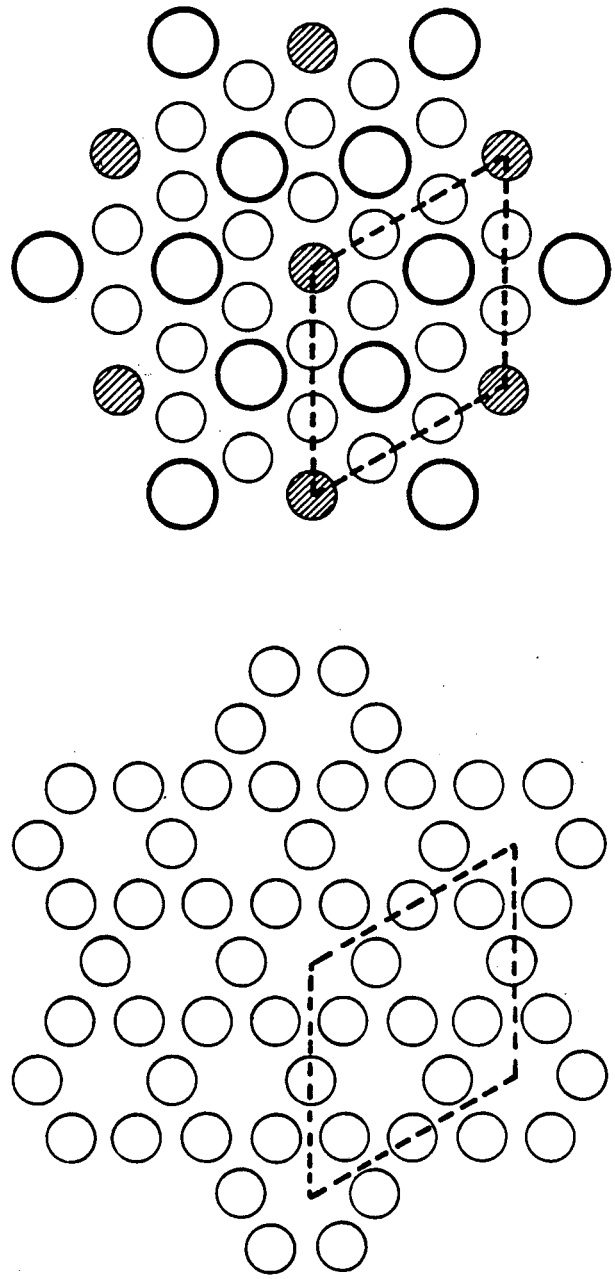

PLAN VIEWS OF ATOMIC PLANES IN R2:17

RARE EARTH SITE

DUMBBELL COBALT SITE

COBALT SITE

XBL834-5543

FIGURE 6

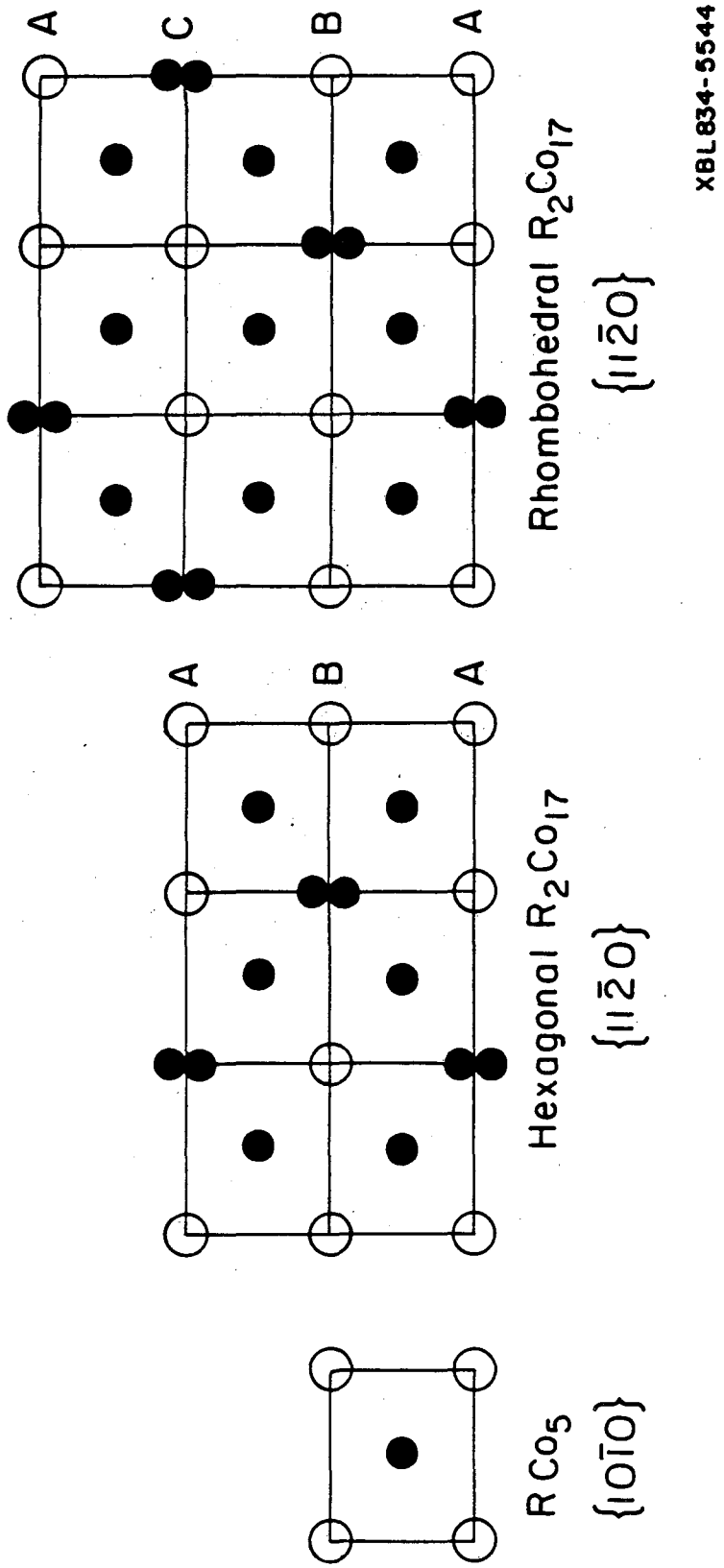
A
C
B
A
Rhombohedral R_2Co_{17}
$\{11\bar{2}0\}$
A
B
A
Hexagonal R_2Co_{17}
$\{11\bar{2}0\}$
RCo_5
$\{10\bar{1}0\}$
XBL834-5544

FIGURE 7

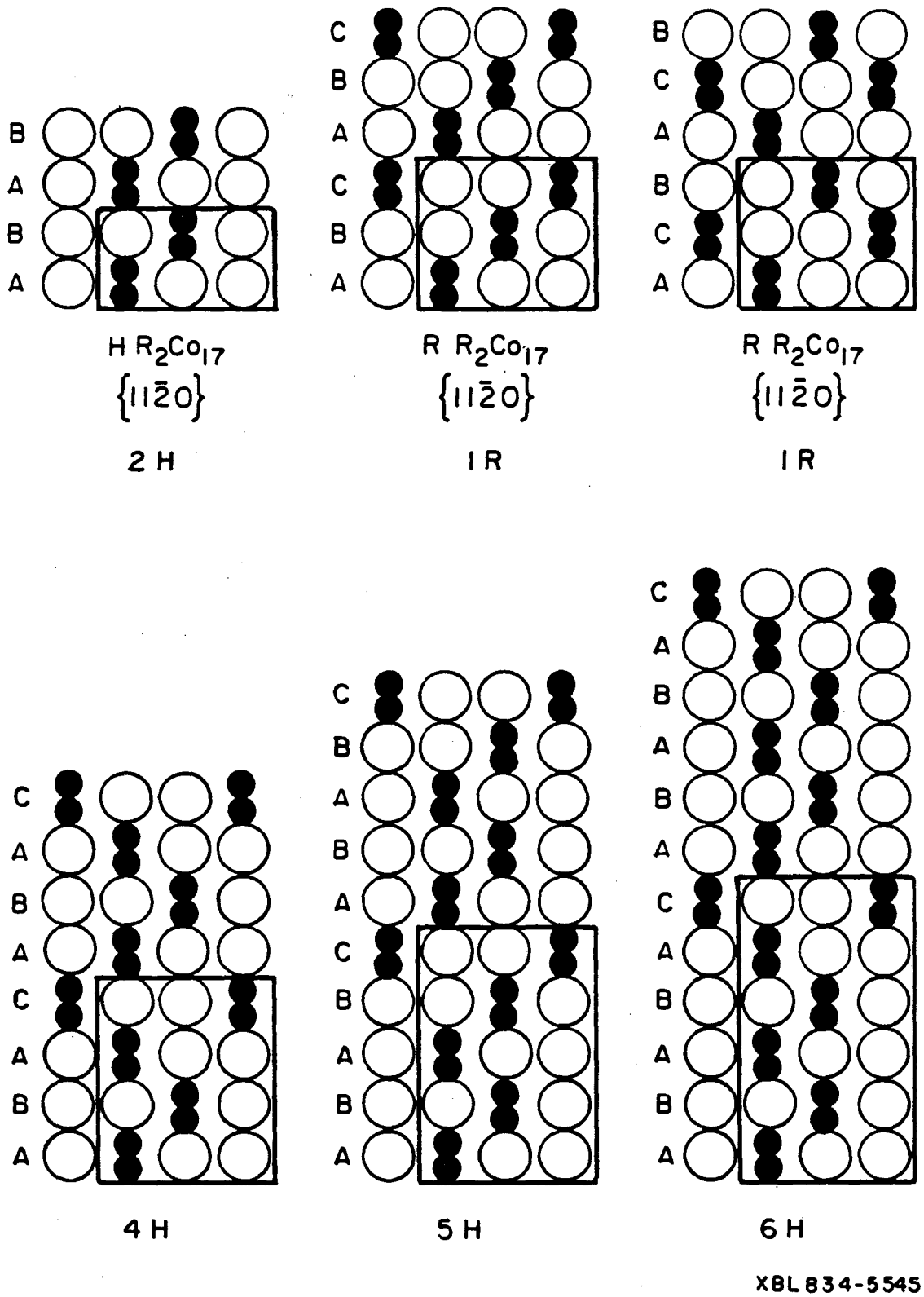
B
A
B
A
H R_2Co_{17}
$\{11\bar{2}0\}$
2 H
C
B
A
C
B
A
R R_2Co_{17}
$\{11\bar{2}0\}$
1 R
B
C
A
B
C
A
R R_2Co_{17}
$\{11\bar{2}0\}$
1 R
C
A
B
A
C
A
B
A
4 H
C
B
A
B
A
C
B
A
B
A
5 H
C
A
B
A
B
A
C
A
B
A
B
A
6 H
XBL 834-5545

FIGURE 8

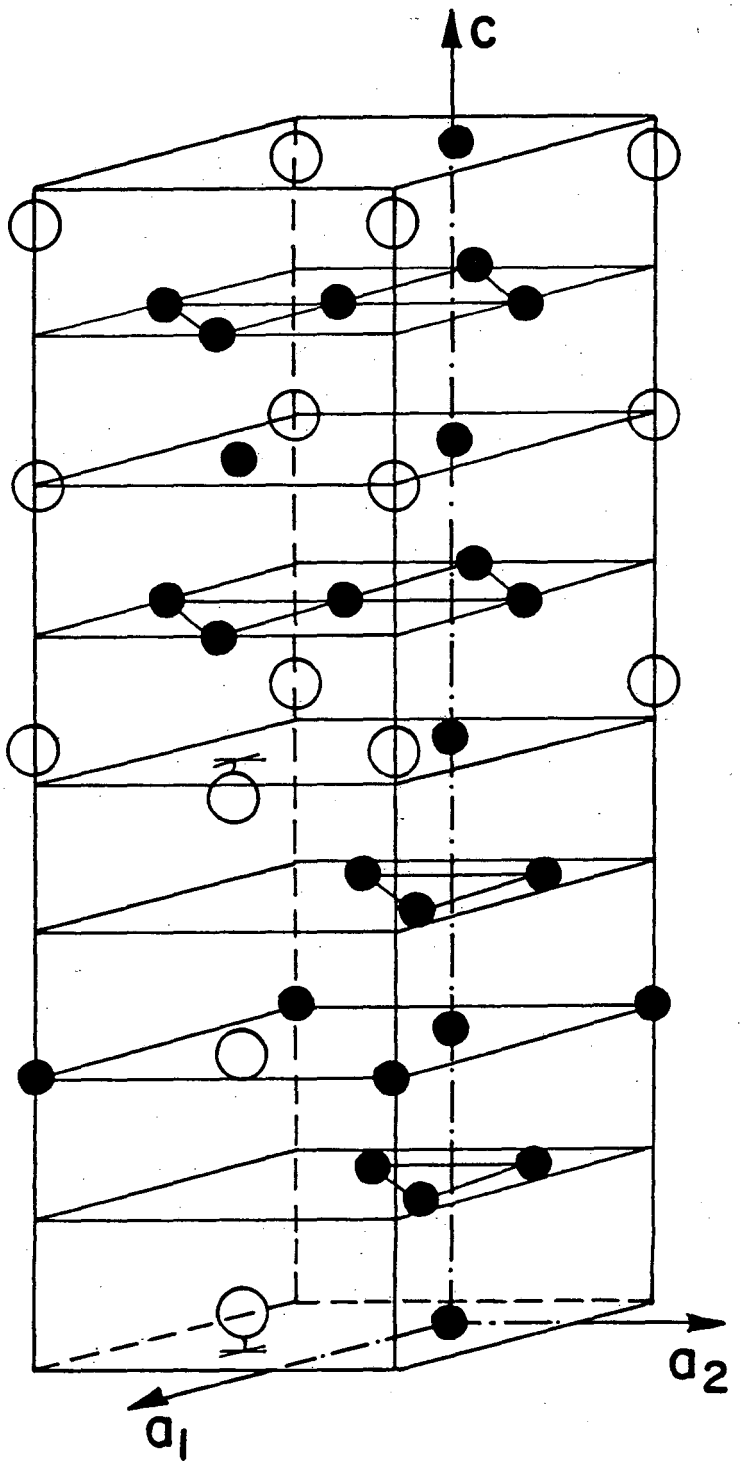

Hexagonal R Co_3

XBL 831-5009

FIGURE 9

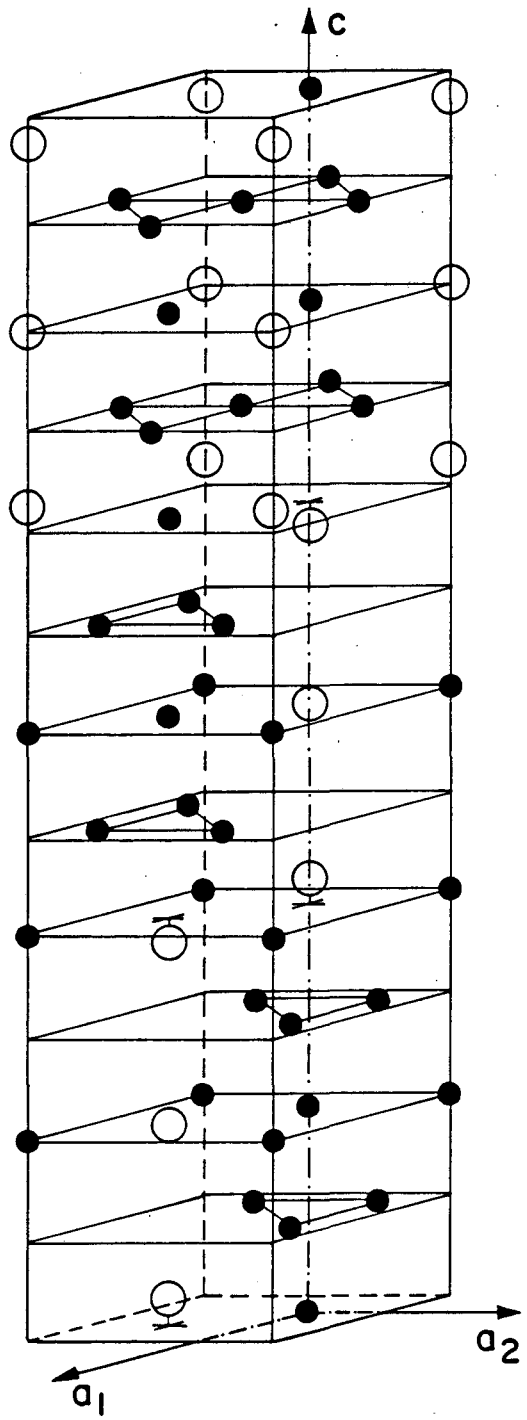

Rhombohedral R Co_3

XBL 831-5011

FIGURE 10

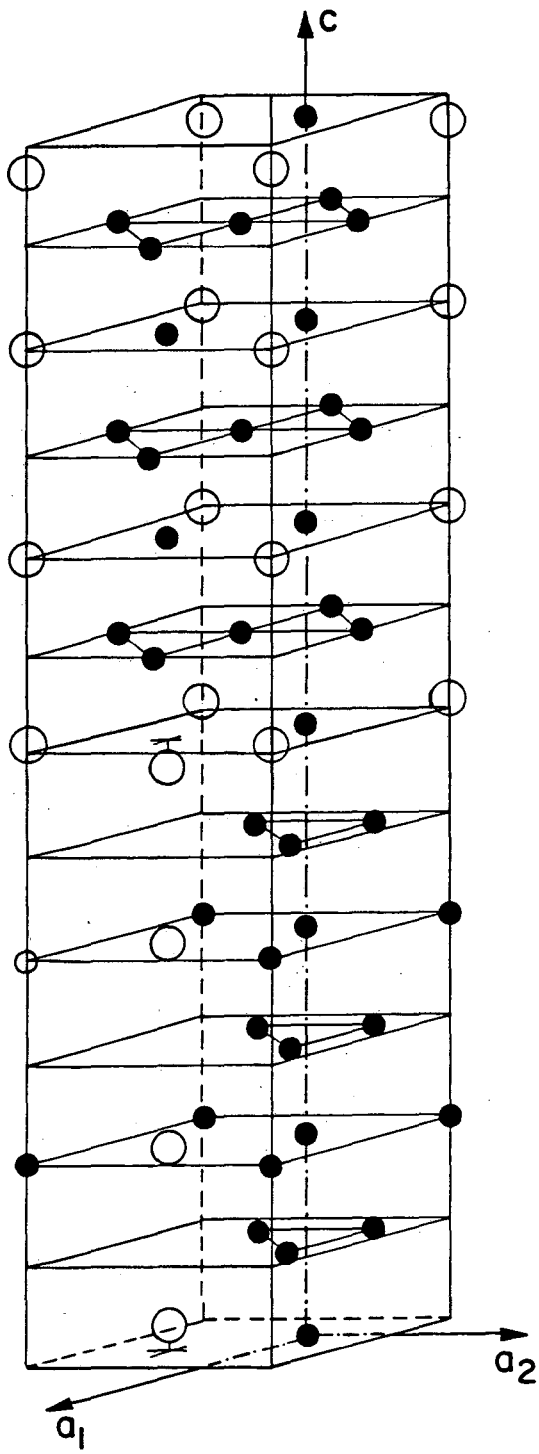

Hexagonal R_2 Co_7

XBL 831-5010

FIGURE 11

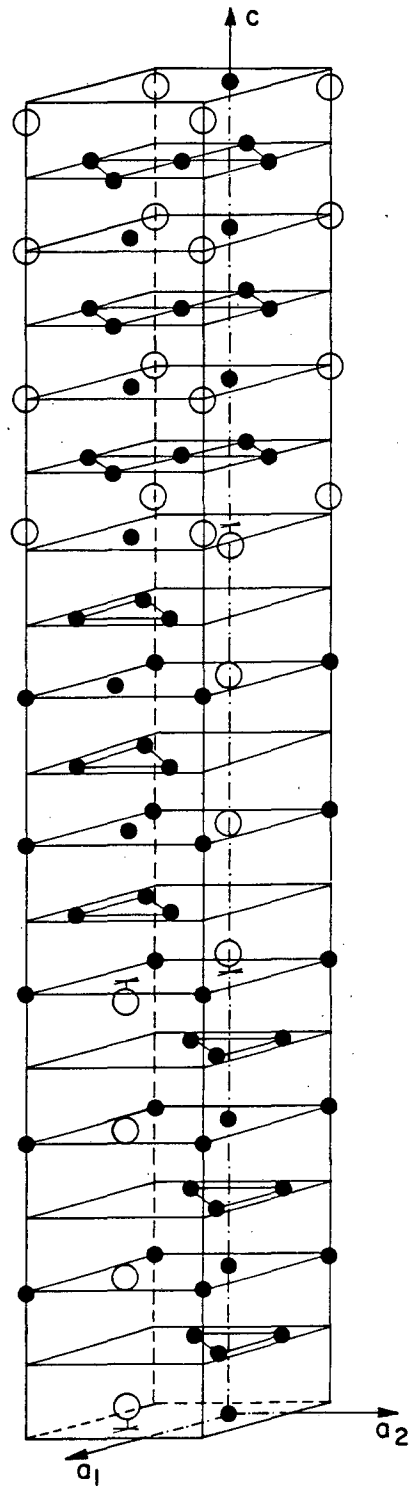

Rhombohedral R_2Co_7

XBL 831-5012

FIGURE 12

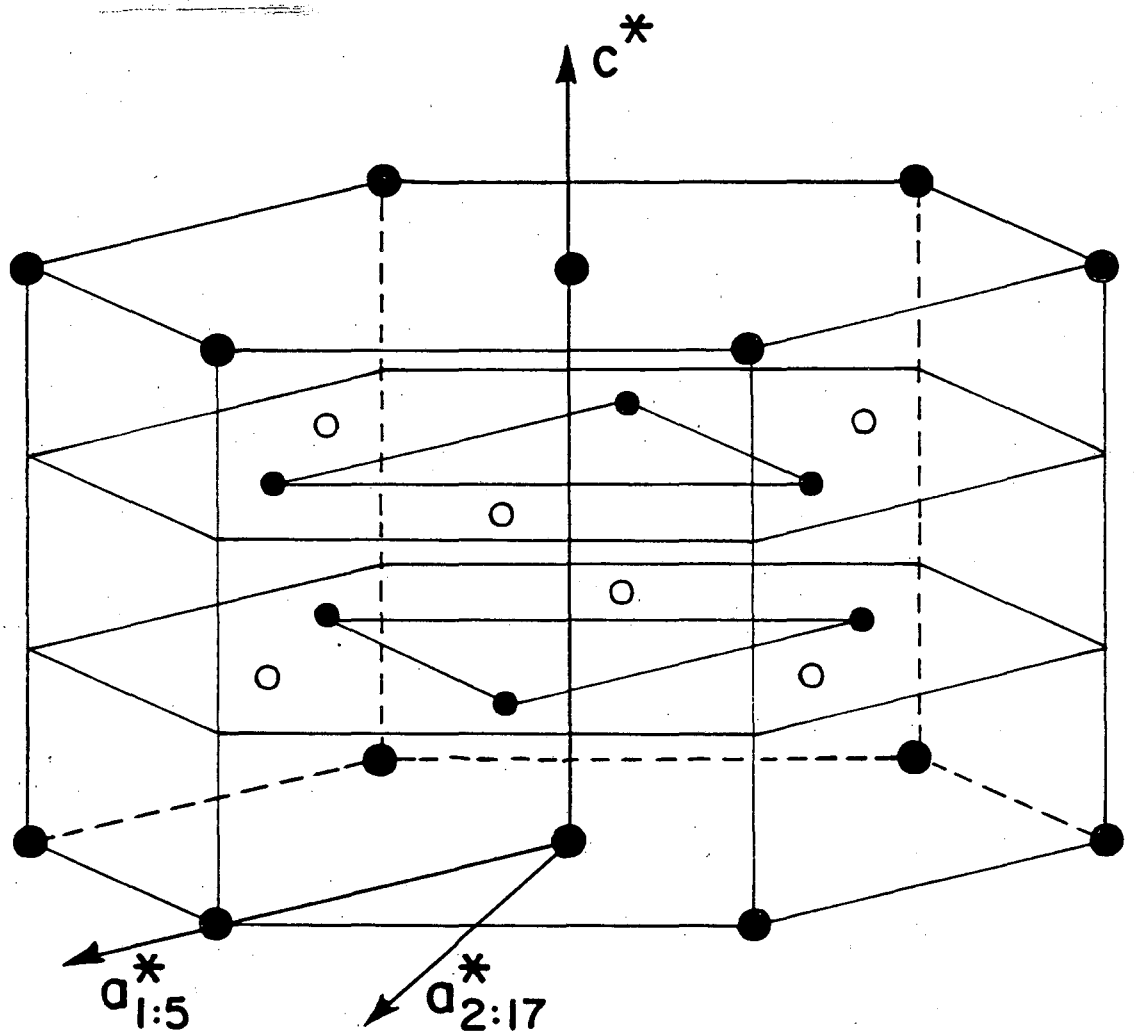

Rhombohedral R_2Co_{17} Reciprocal Lattice

- ● Reflections common to RCo_5 and both rhombohedral R_2Co_{17} twin-related variants
- ● Rhombohedral R_2Co_{17} reflections from one variant
- o Rhombohedral R_2Co_{17} reflections from the other variant

XBL 832-5188

FIGURE 13

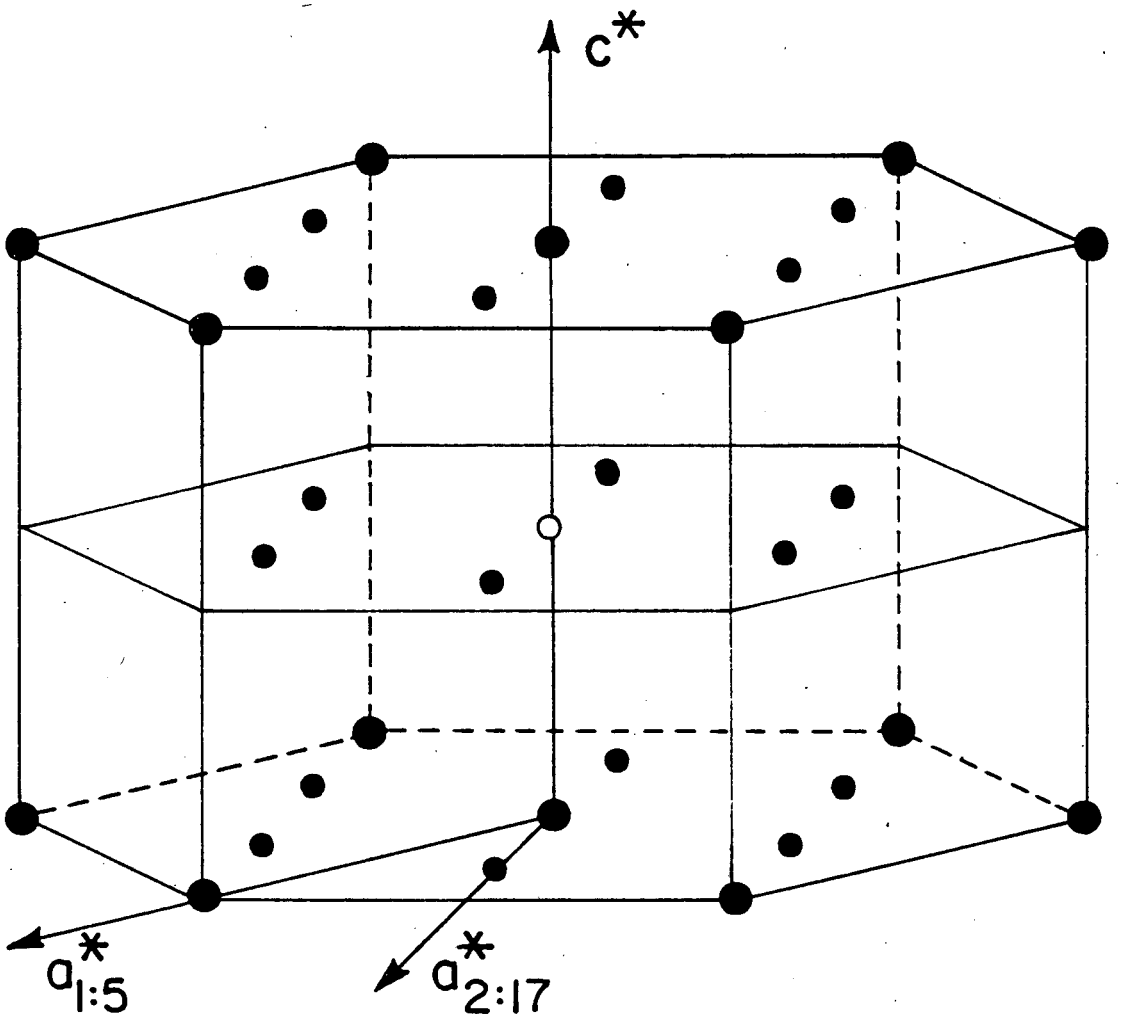

Hexagonal R_2Co_{17} Reciprocal Lattice

● Reflections common to R_2Co_{17} and RCo_5

● Allowed hexagonal R_2Co_{17} reflections

○ Kinematically forbidden hexagonal R_2Co_{17} reflections

XBL 832-5187

FIGURE 14

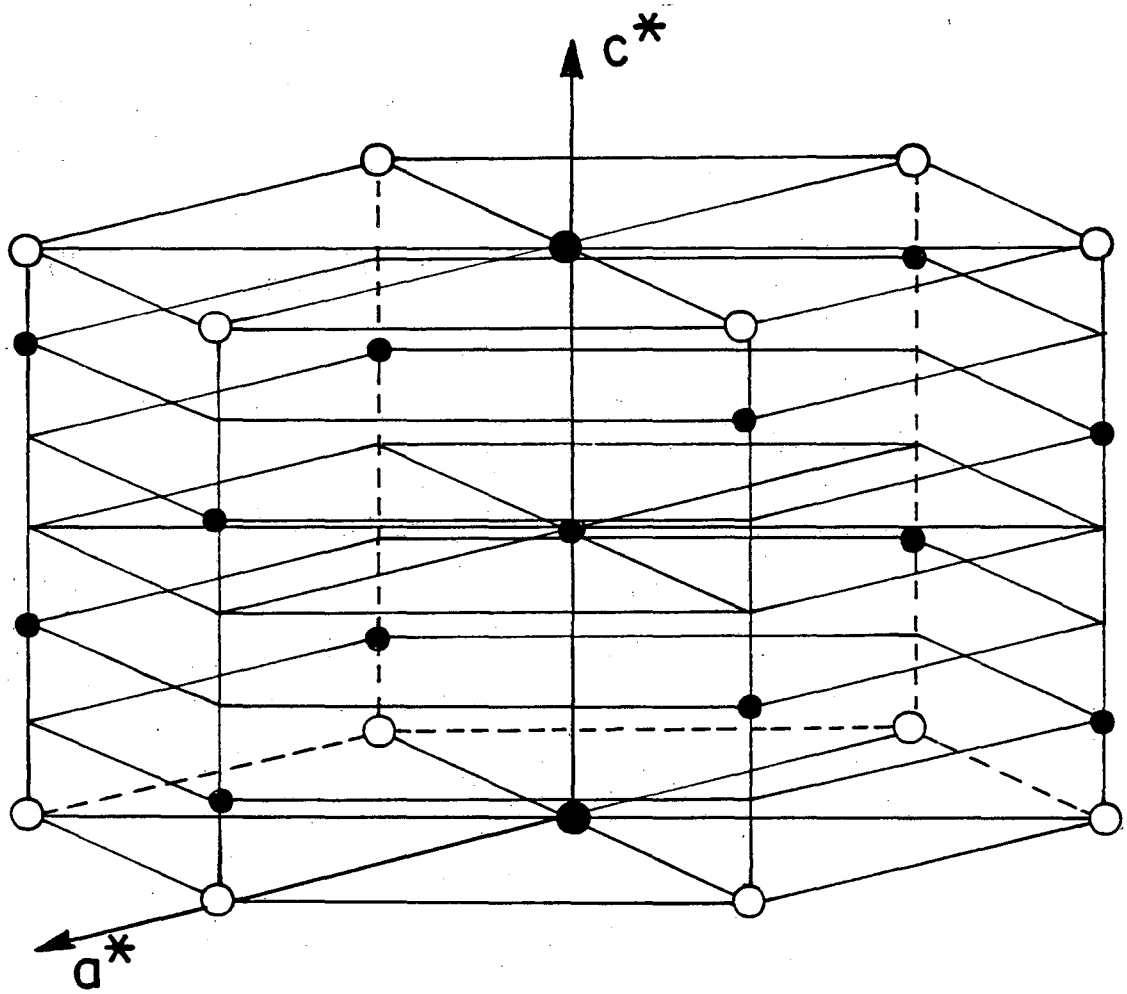

Rhombohedral RCo_3 Reciprocal Lattice

● Reflections common to RCo_5 and RCo_3

○ RCo_5 reflections

● Rhombohedral RCo_3 reflections
(Only one variant is shown)

XBL 832-5189

FIGURE 15

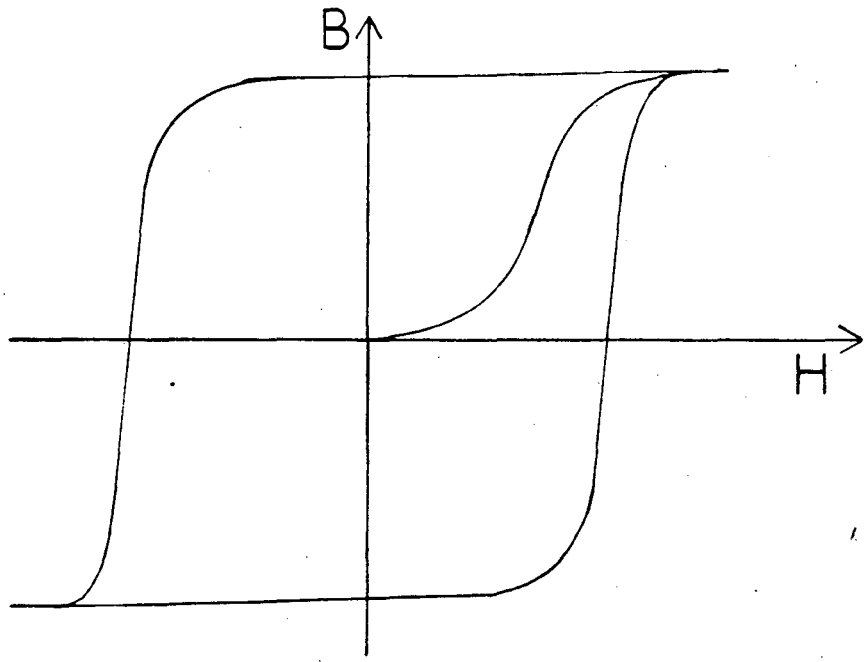

(a) DOMAIN NUCLEATION LIMITED

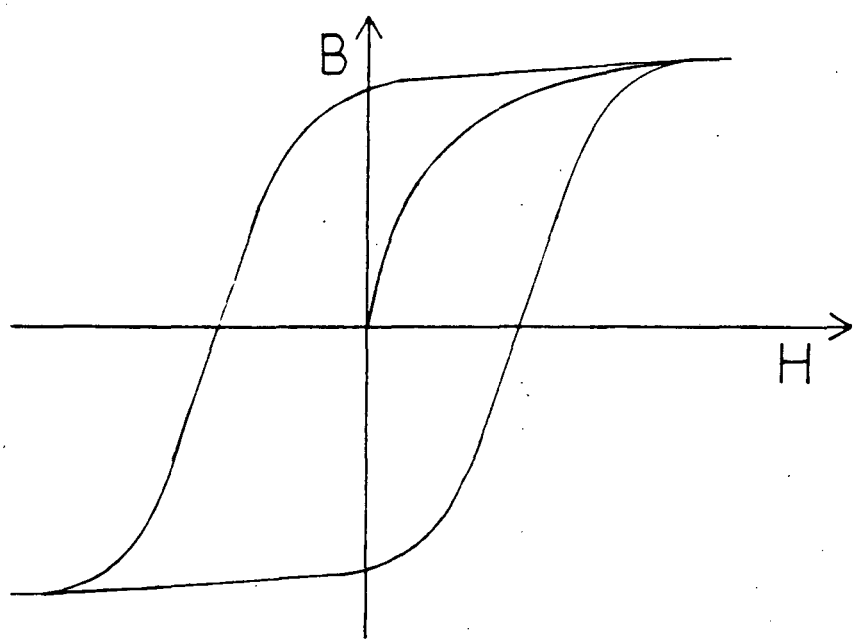

(b) DOMAIN WALL PINNING LIMITED

XBL 835-9800

FIGURE 16

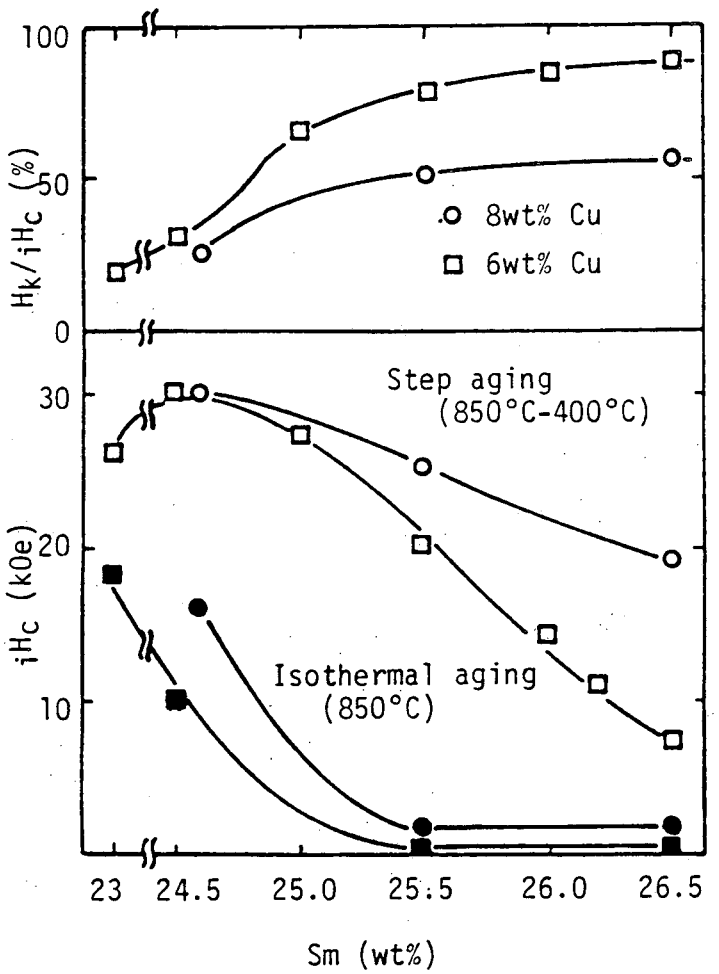

XBL 8011-7429

FIGURE 17

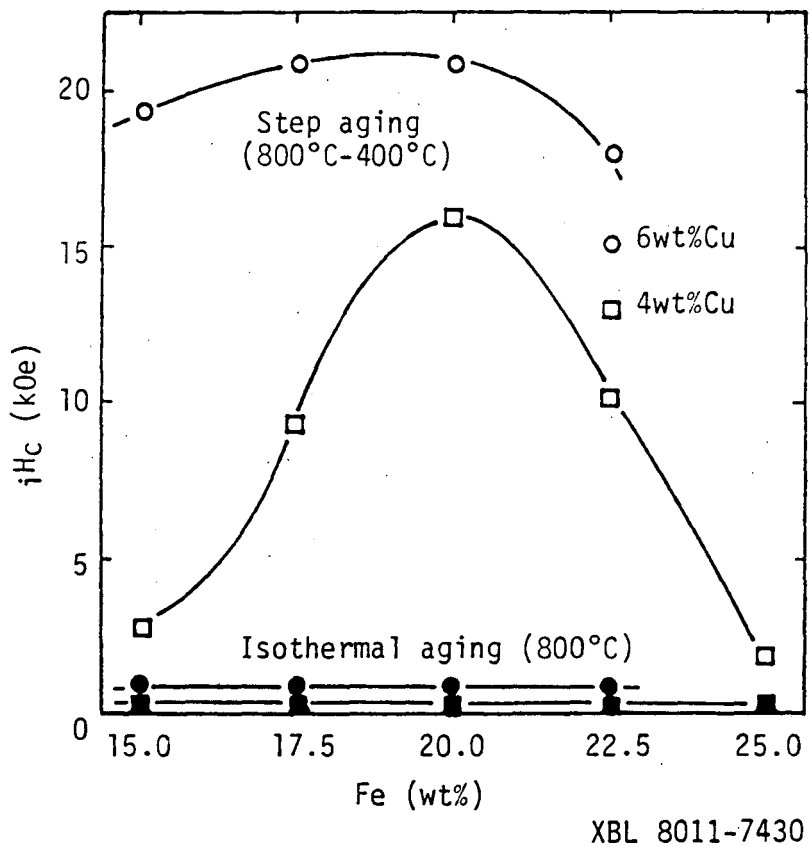
20
15
10
5
0
iHc (kOe)
Step aging
(800°C-400°C)
6wt%Cu
4wt%Cu
Isothermal aging (800°C)
15.0
17.5
20.0
22.5
25.0
Fe (wt%)
XBL 8011-7430

FIGURE 18

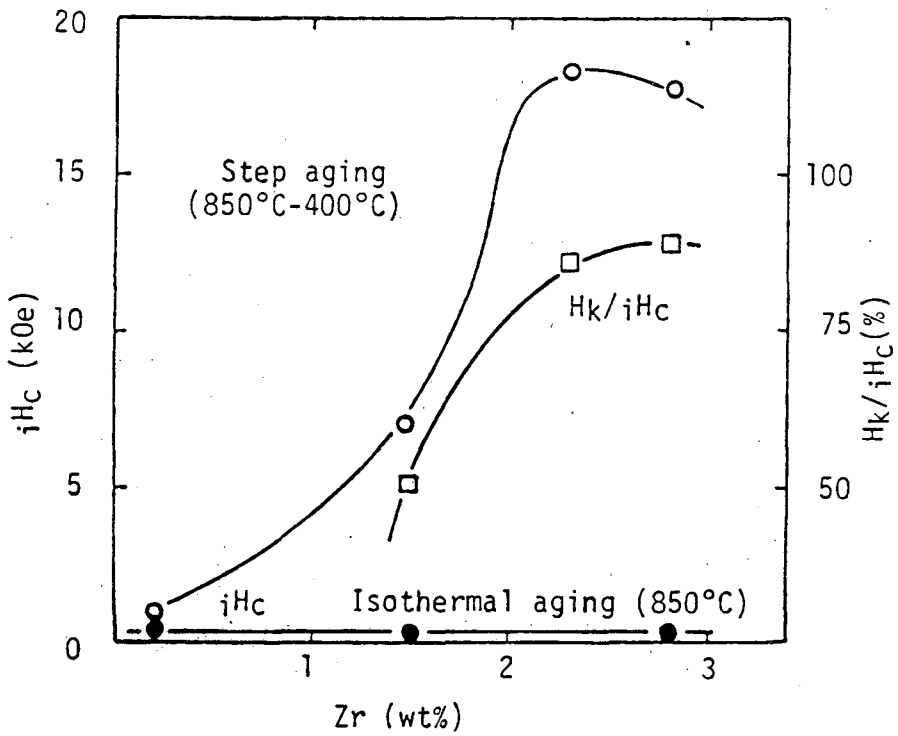

XBL 8011-7432

FIGURE 19

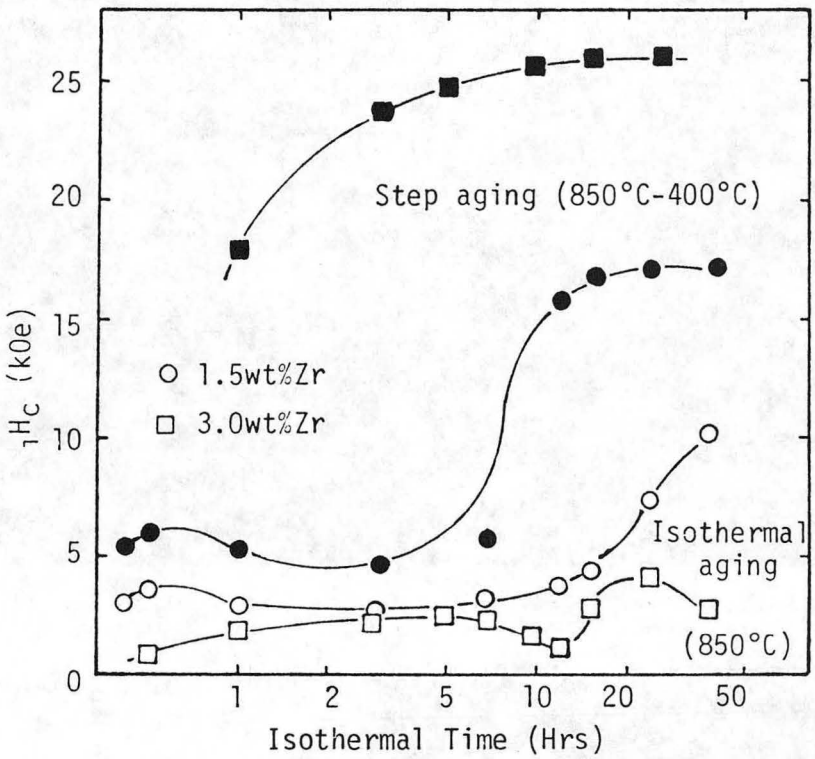

XBL 8011-7418

FIGURE 20

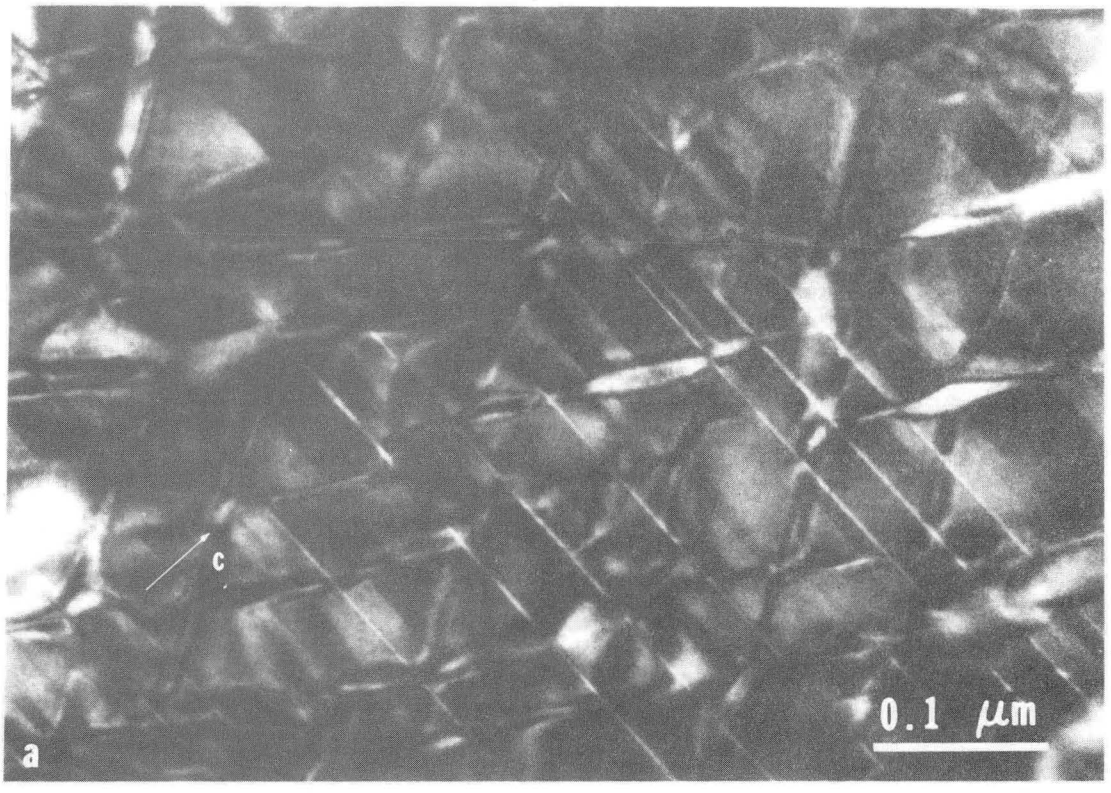

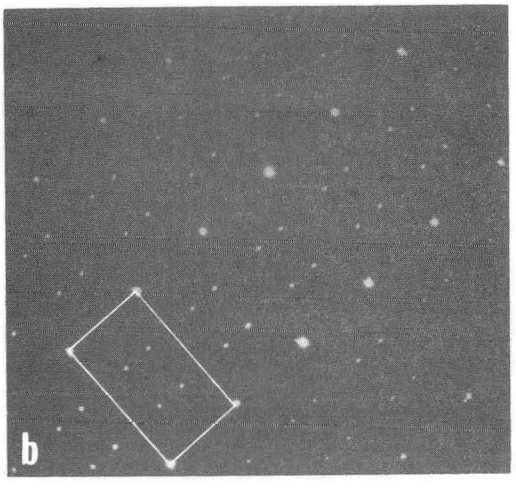

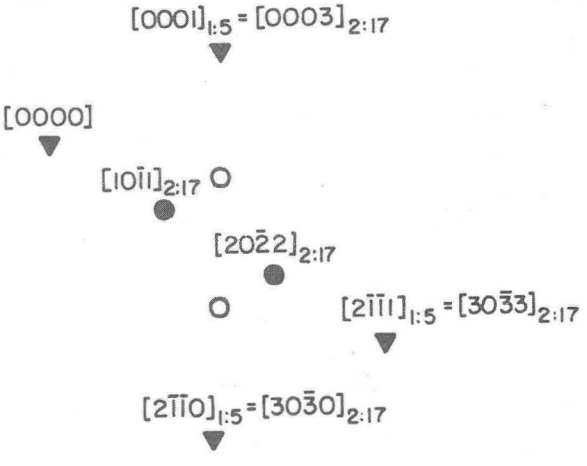

XBB 810-9499

FIGURE 21

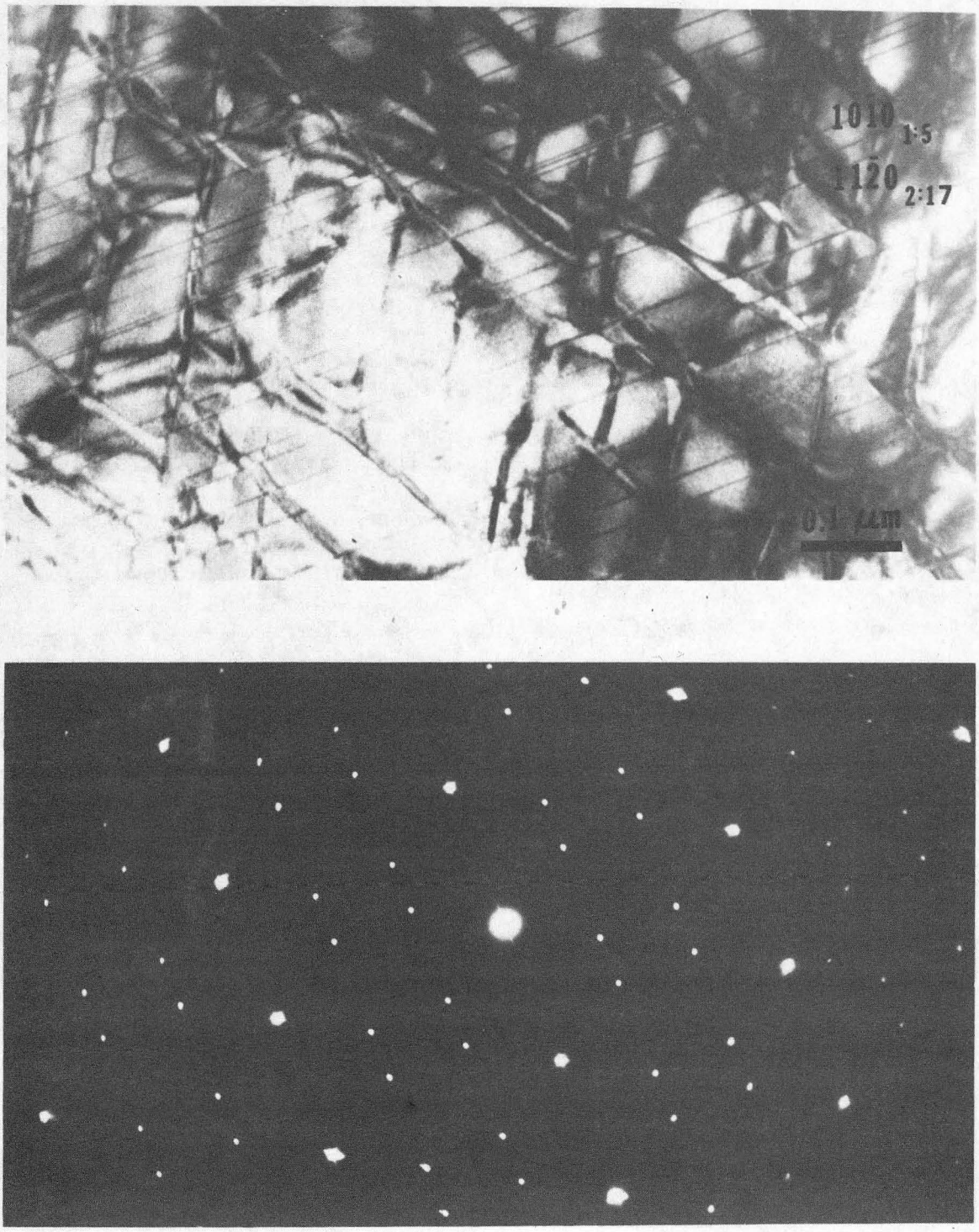

XBB 835-4361

FIGURE 22

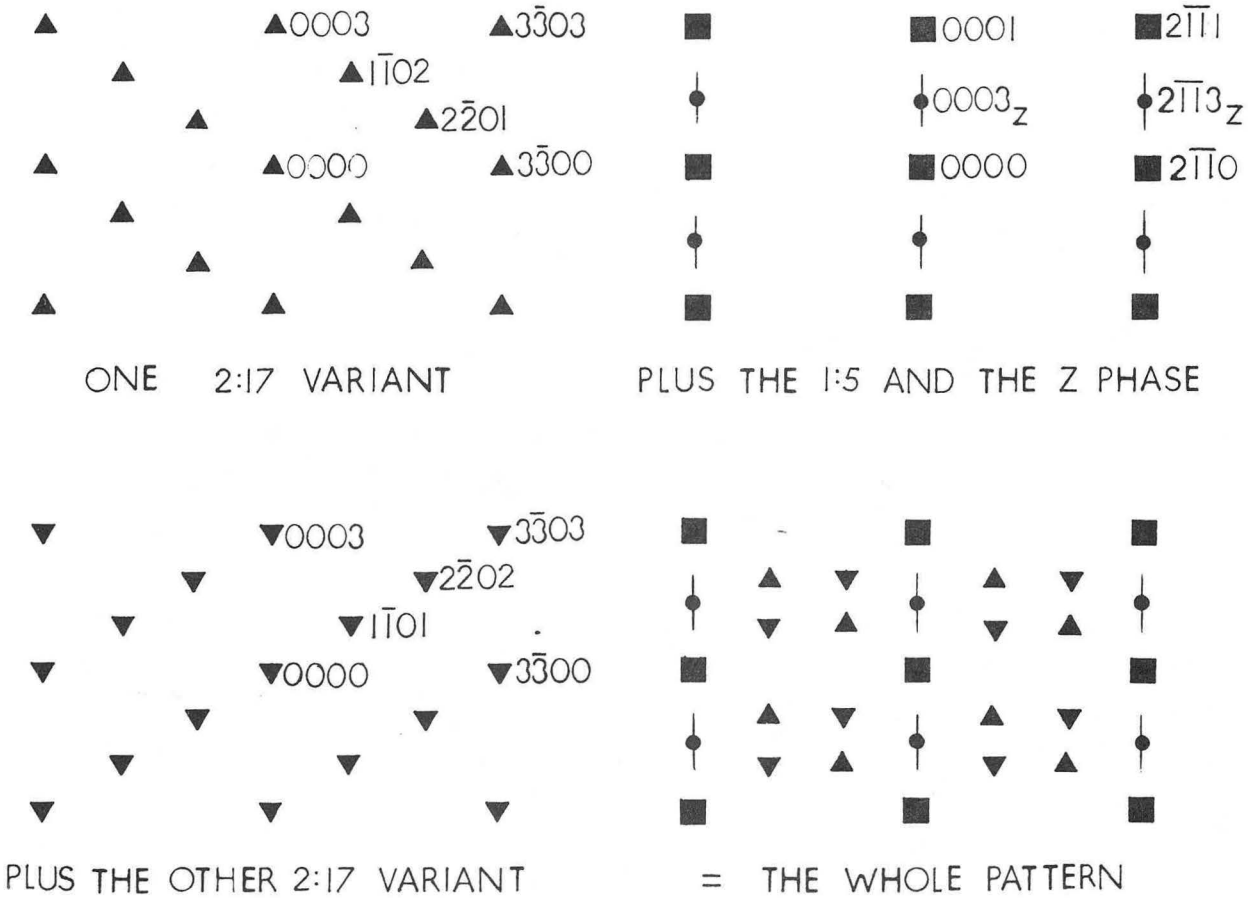

$$[01\bar{1}0]_{1:5} = [11\bar{2}0]_{2:17} = [01\bar{1}0]_Z$$

XBL 836-10124

FIGURE 23

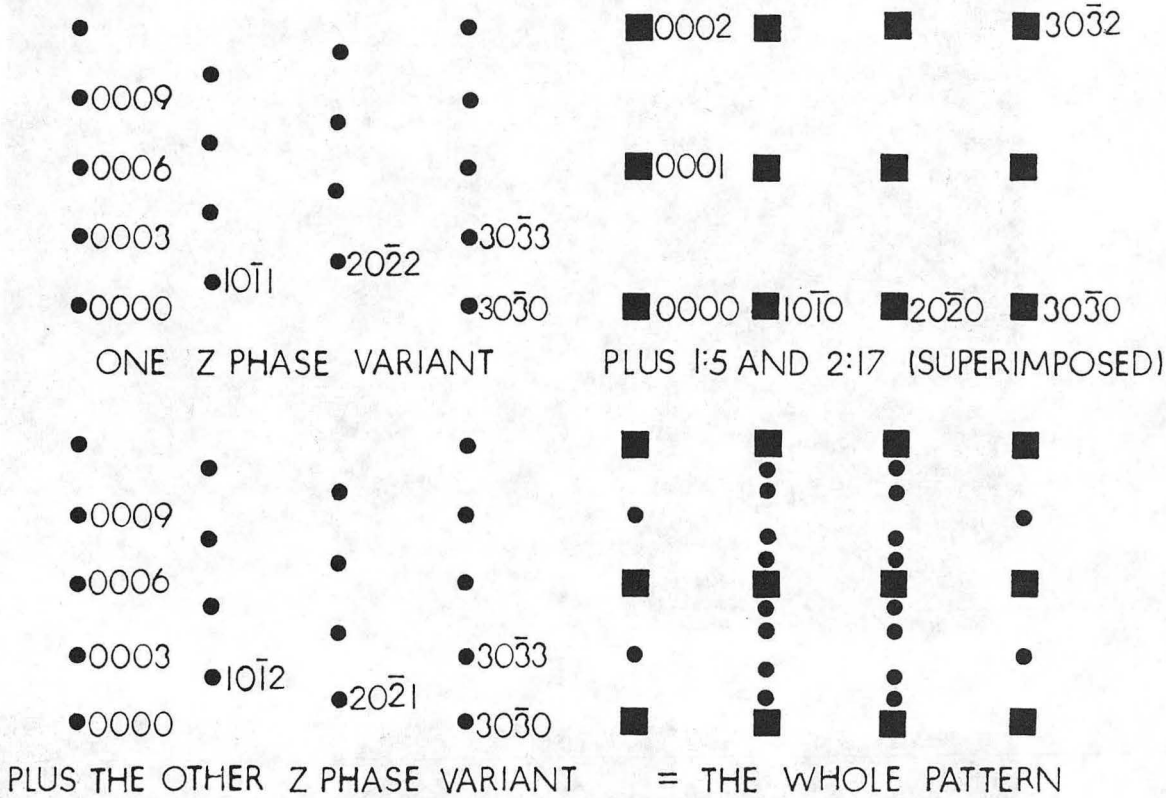

$$[\bar{1}2\bar{1}0]_{1:5} = [01\bar{1}0]_{2:17} = [\bar{1}2\bar{1}0]_{Z}$$

XBL 836-10123

FIGURE 24

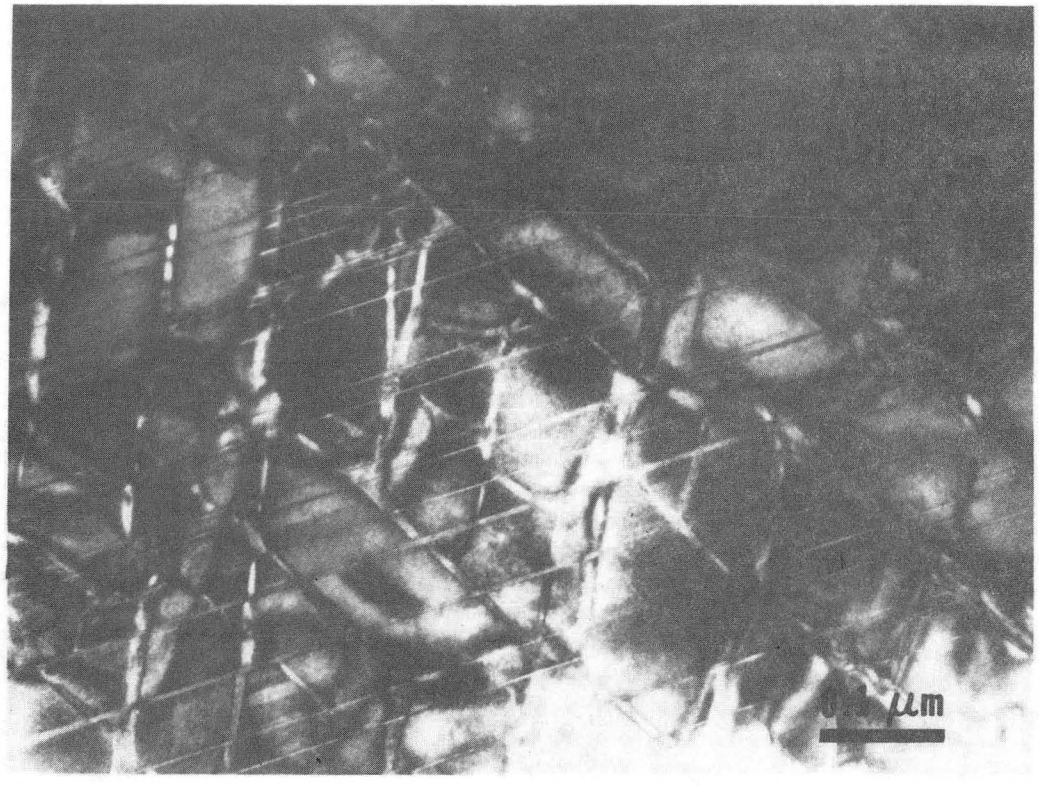

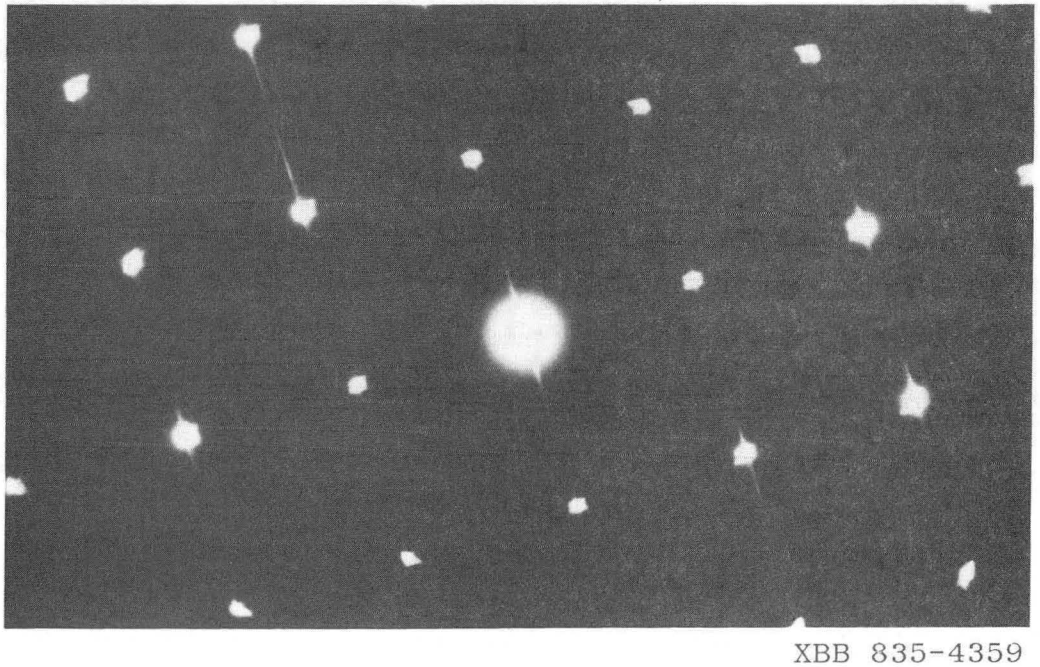

XBB 835-4359

FIGURE 25

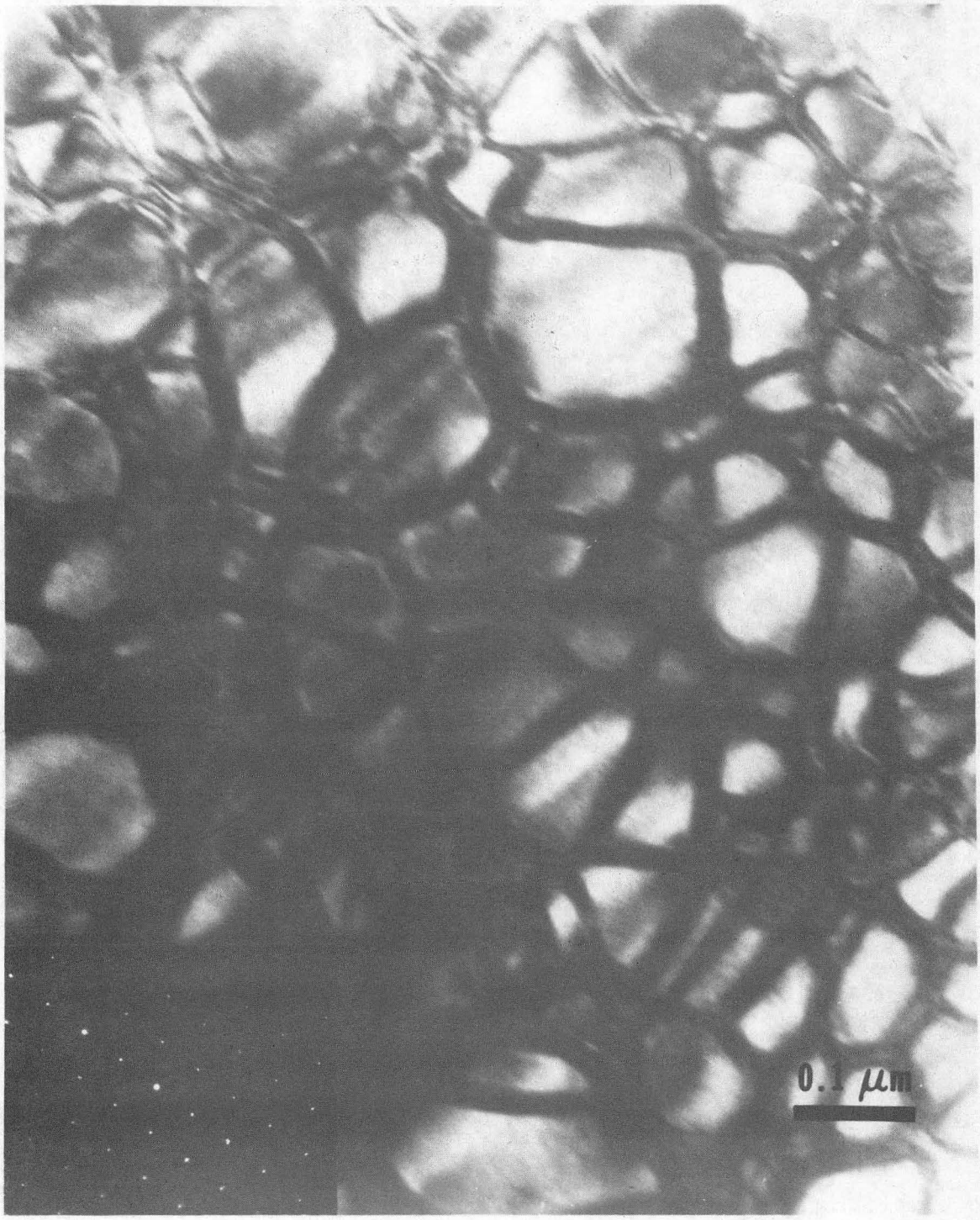

XBB 810-9523

FIGURE 26

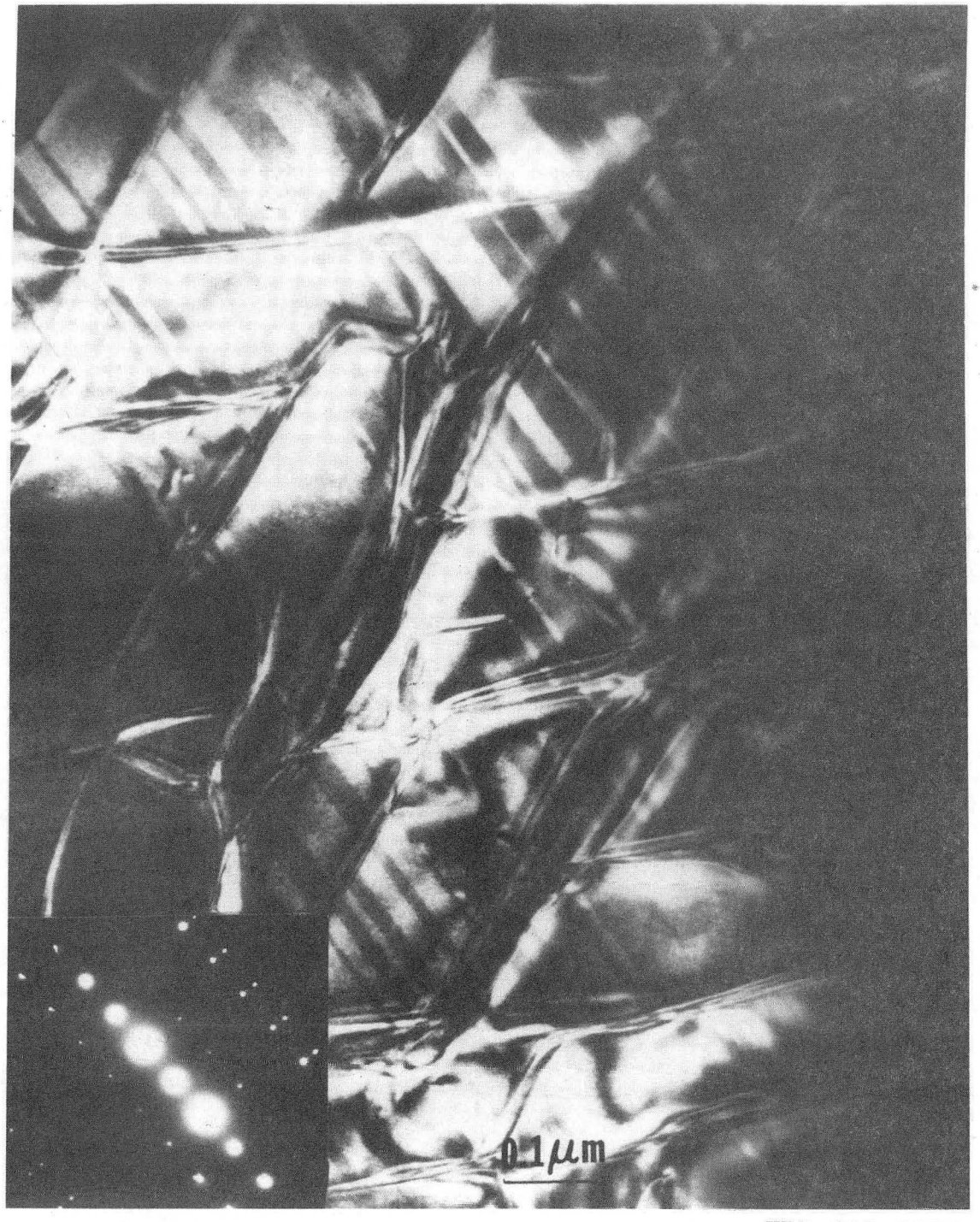

XBB 812-1226

FIGURE 27

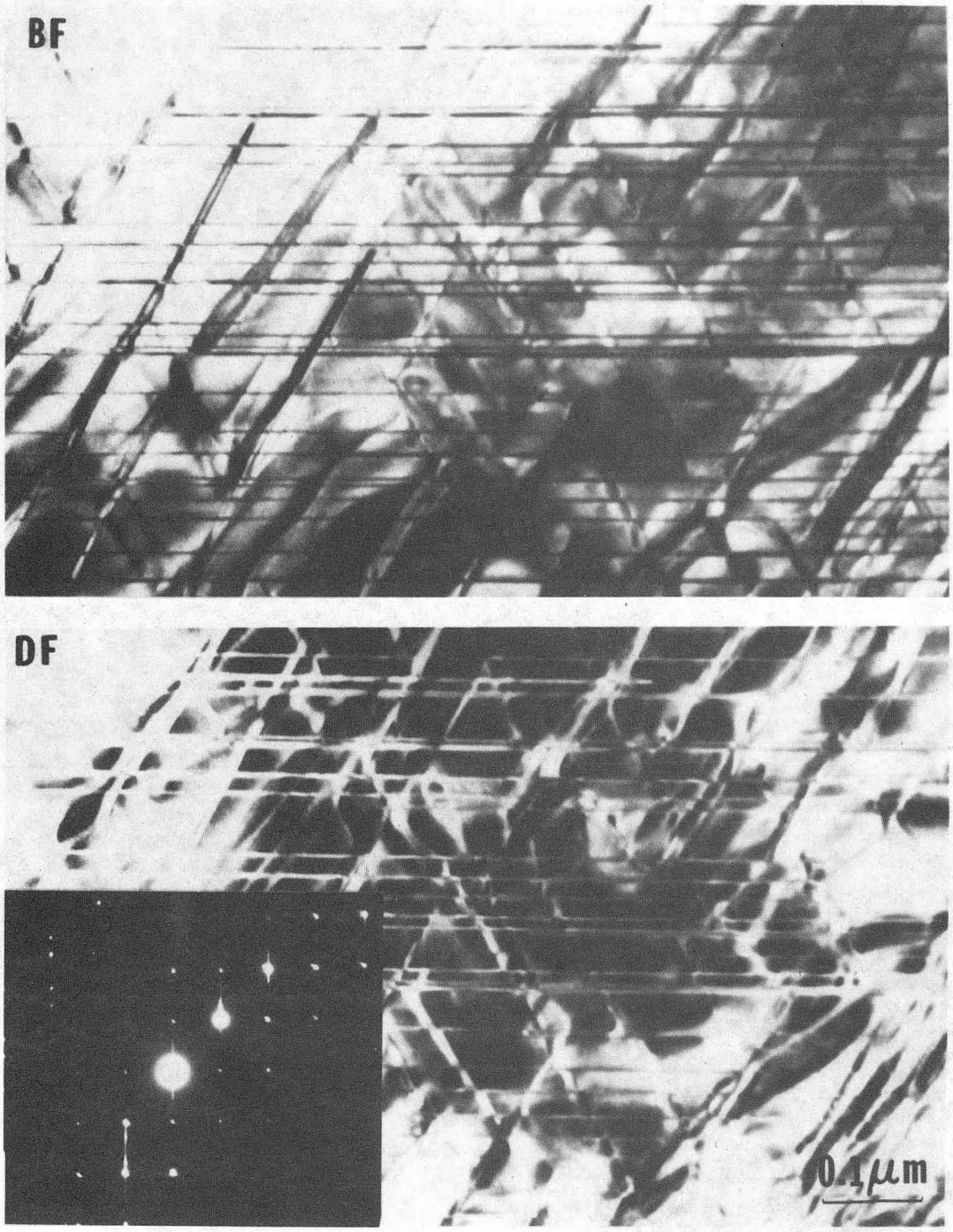

XBB 812-1225

FIGURE 28

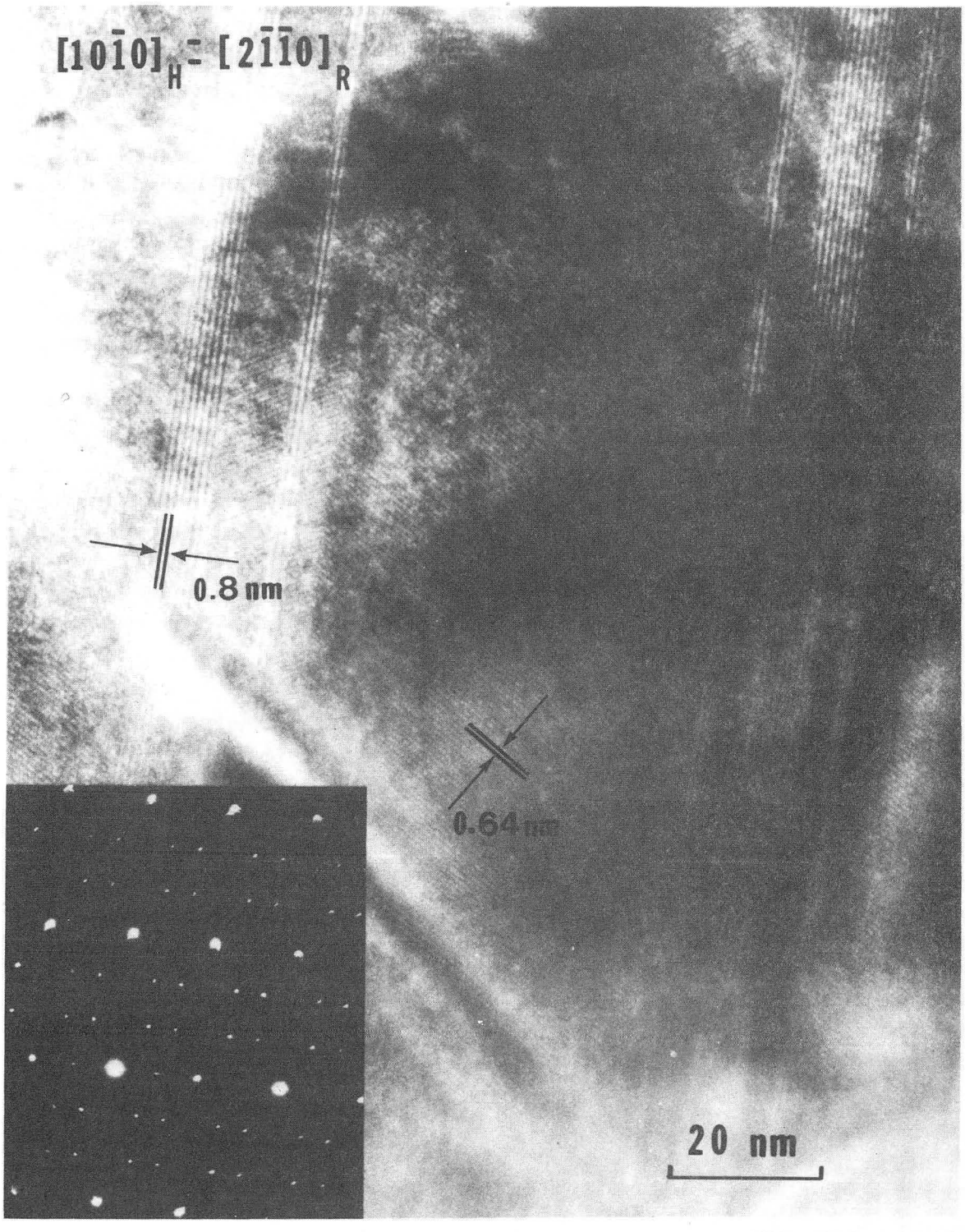

XBB 810-10172

FIGURE 29

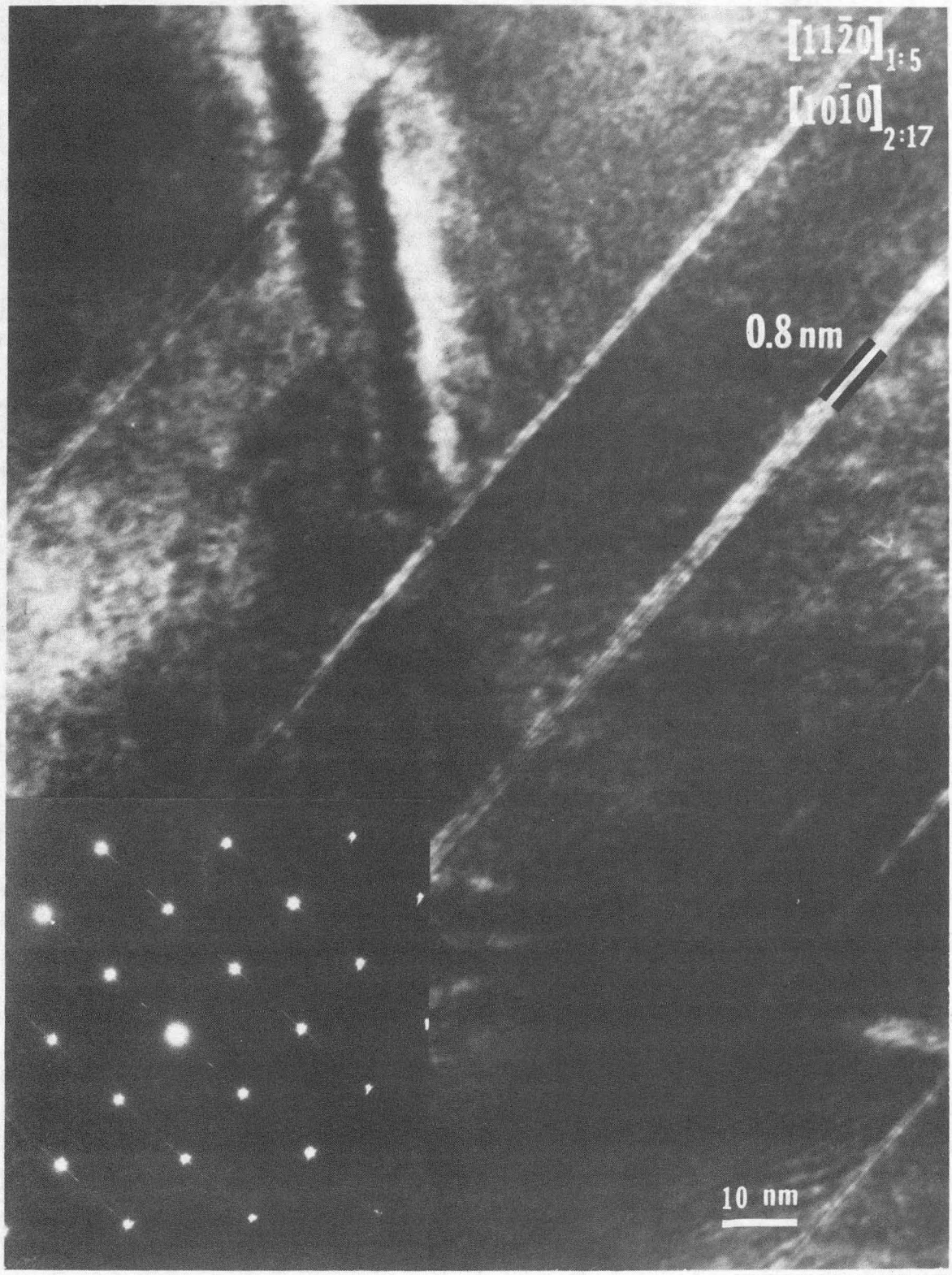

XBB 835-4360

FIGURE 30

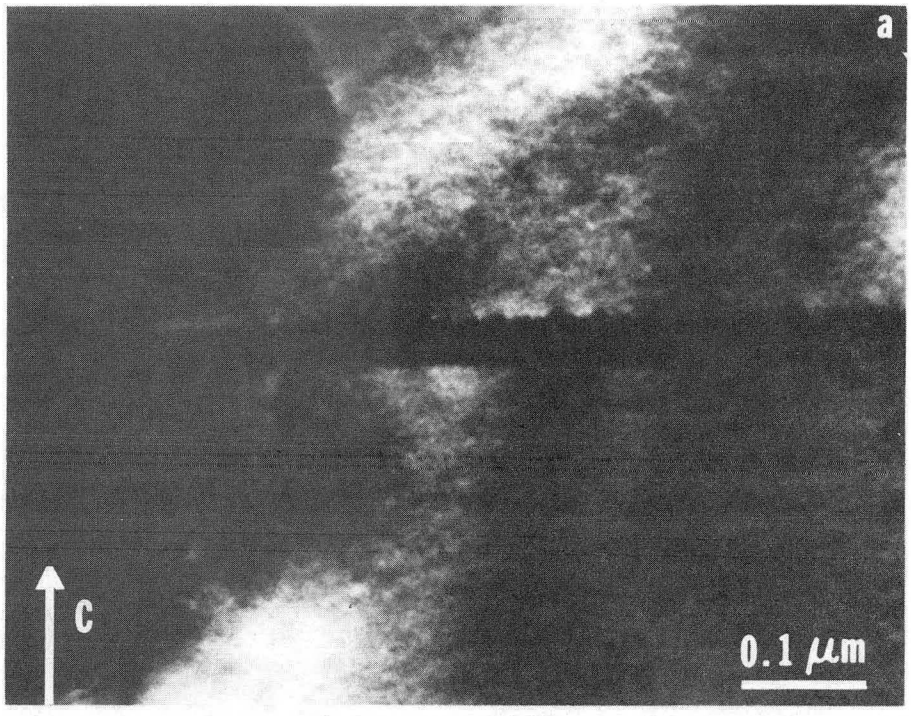

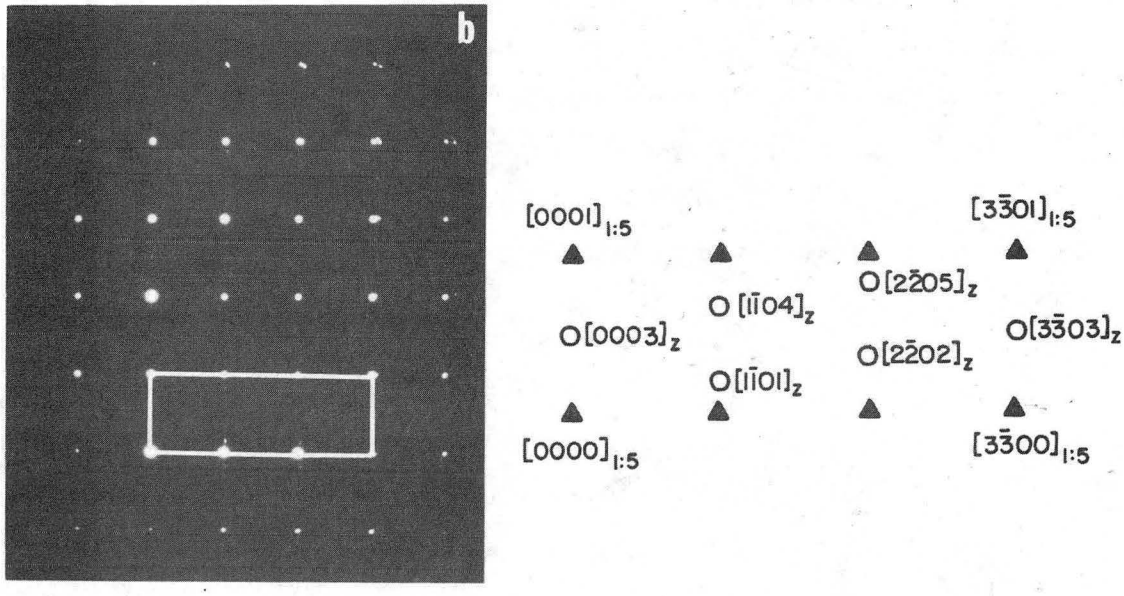

XBB 810-9500

FIGURE 31

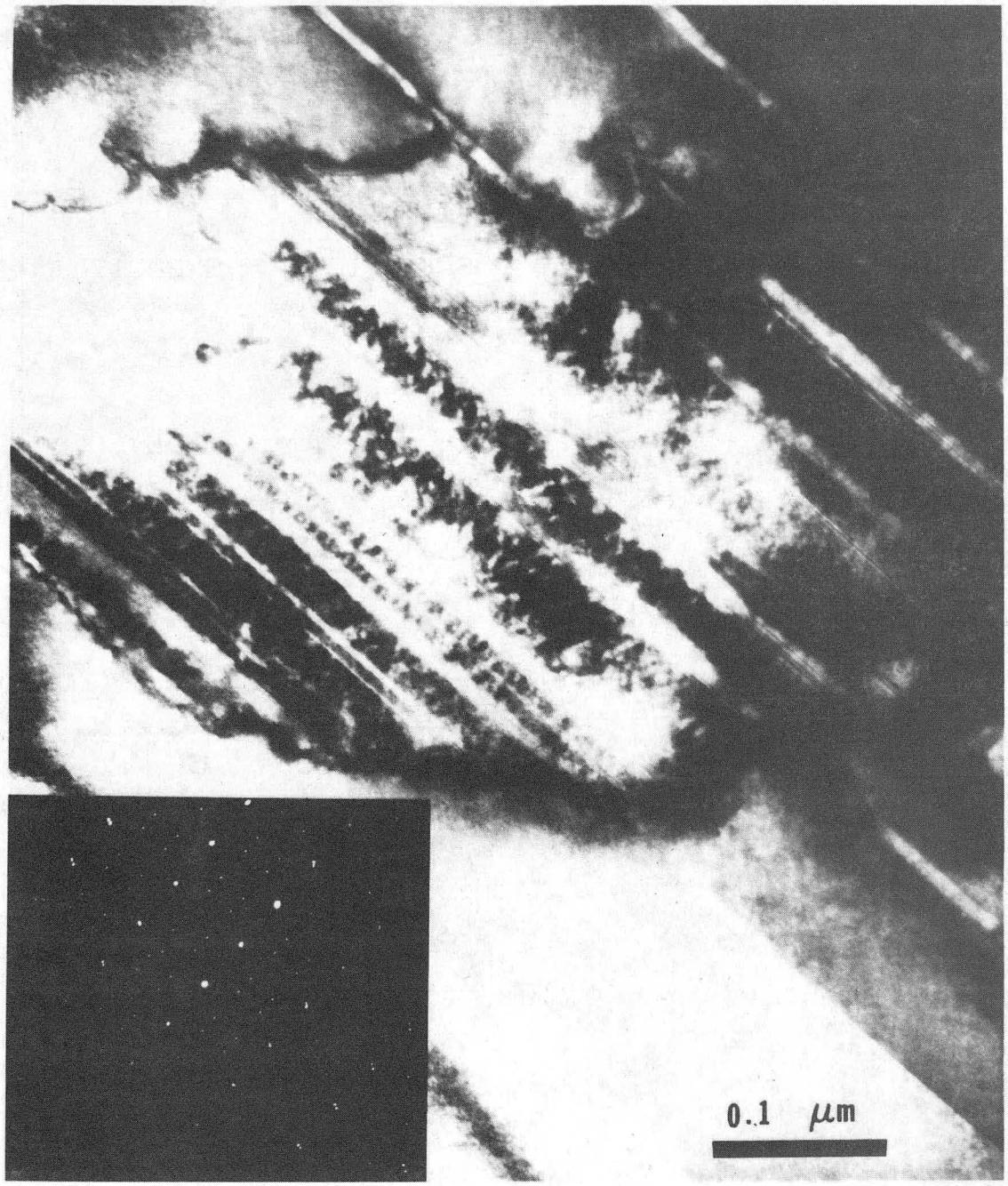

XBB 836-5064

FIGURE 32

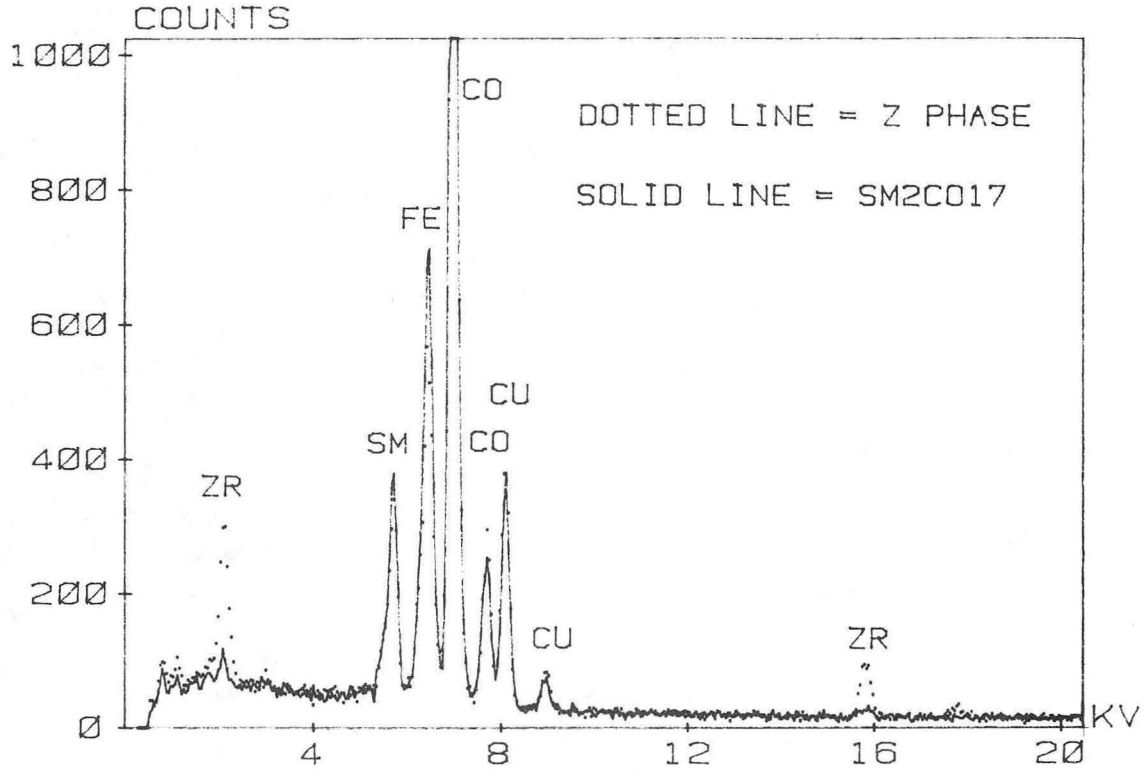

XBL 8110-7168

FIGURE 33

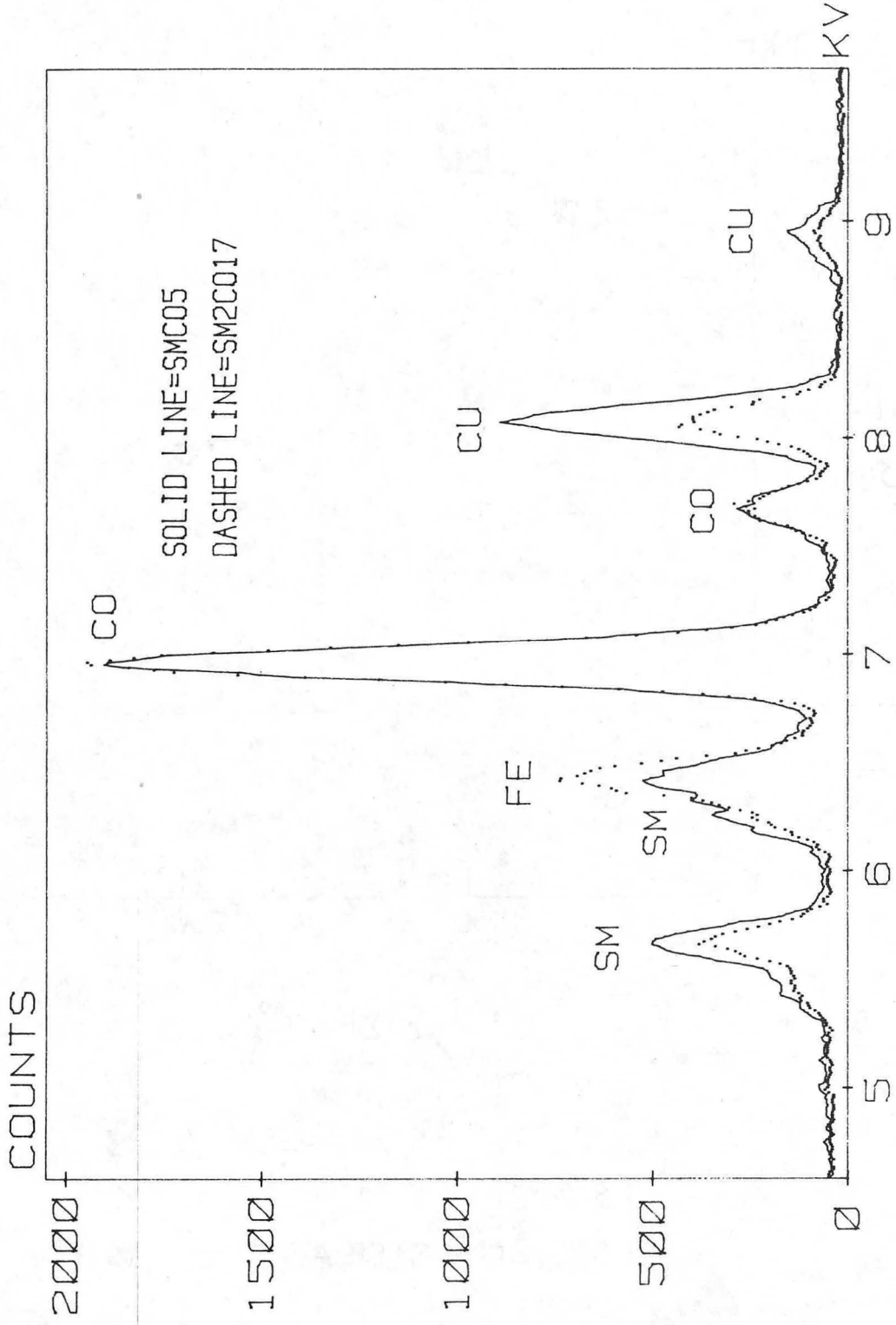

XBL 819-2062

FIGURE 34

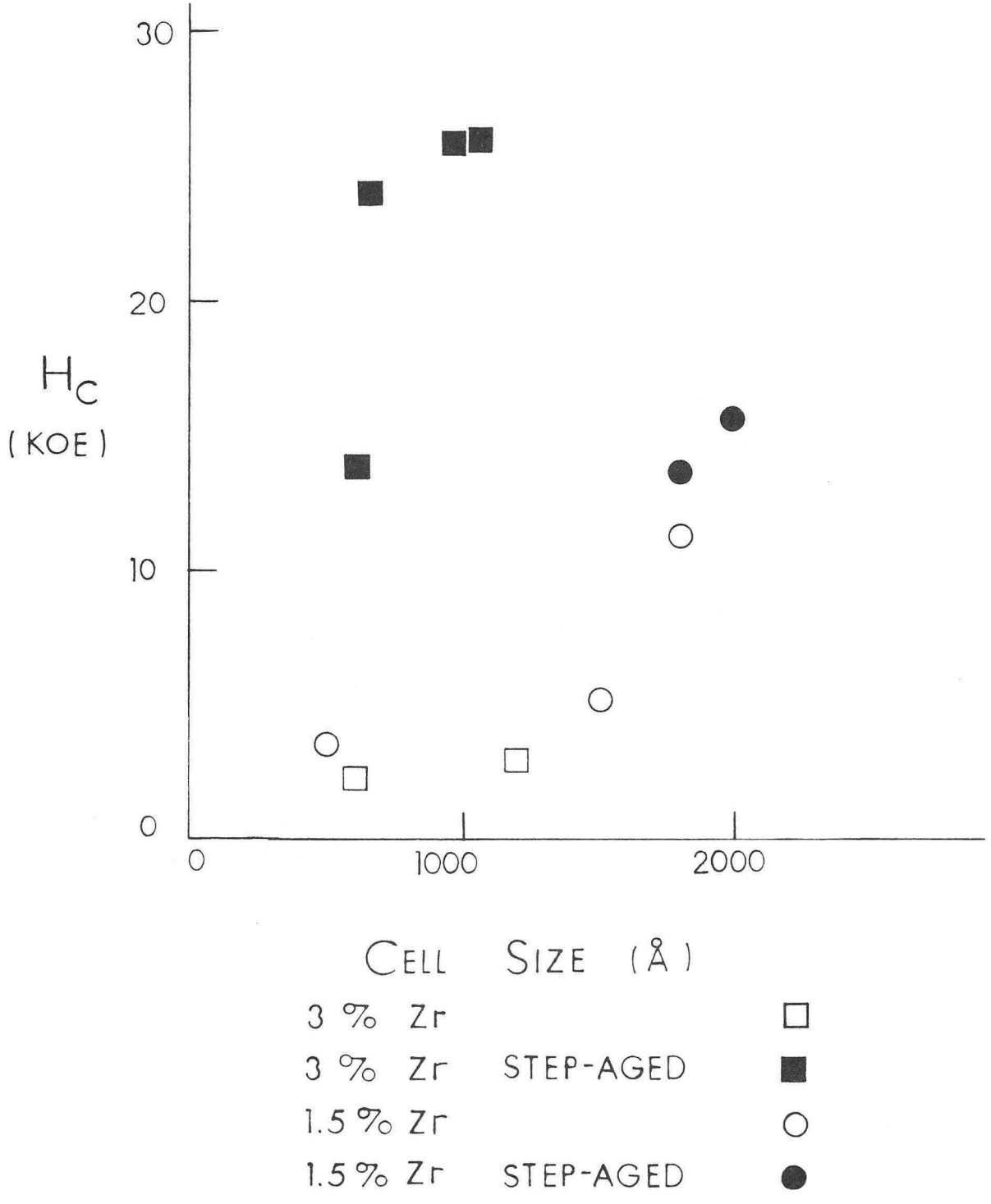

XBL 835-9803

FIGURE 35

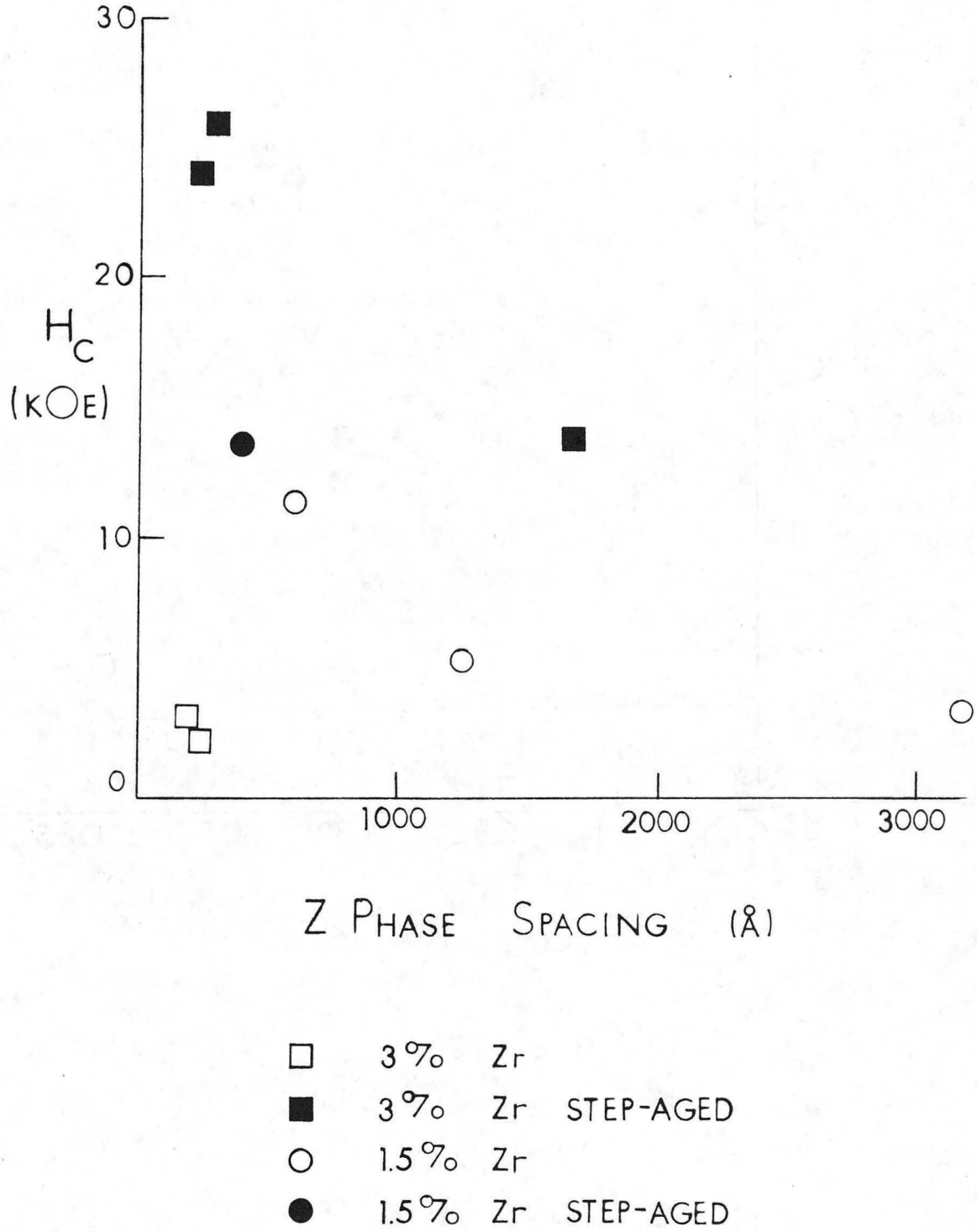

XBL 835-9801

FIGURE 36

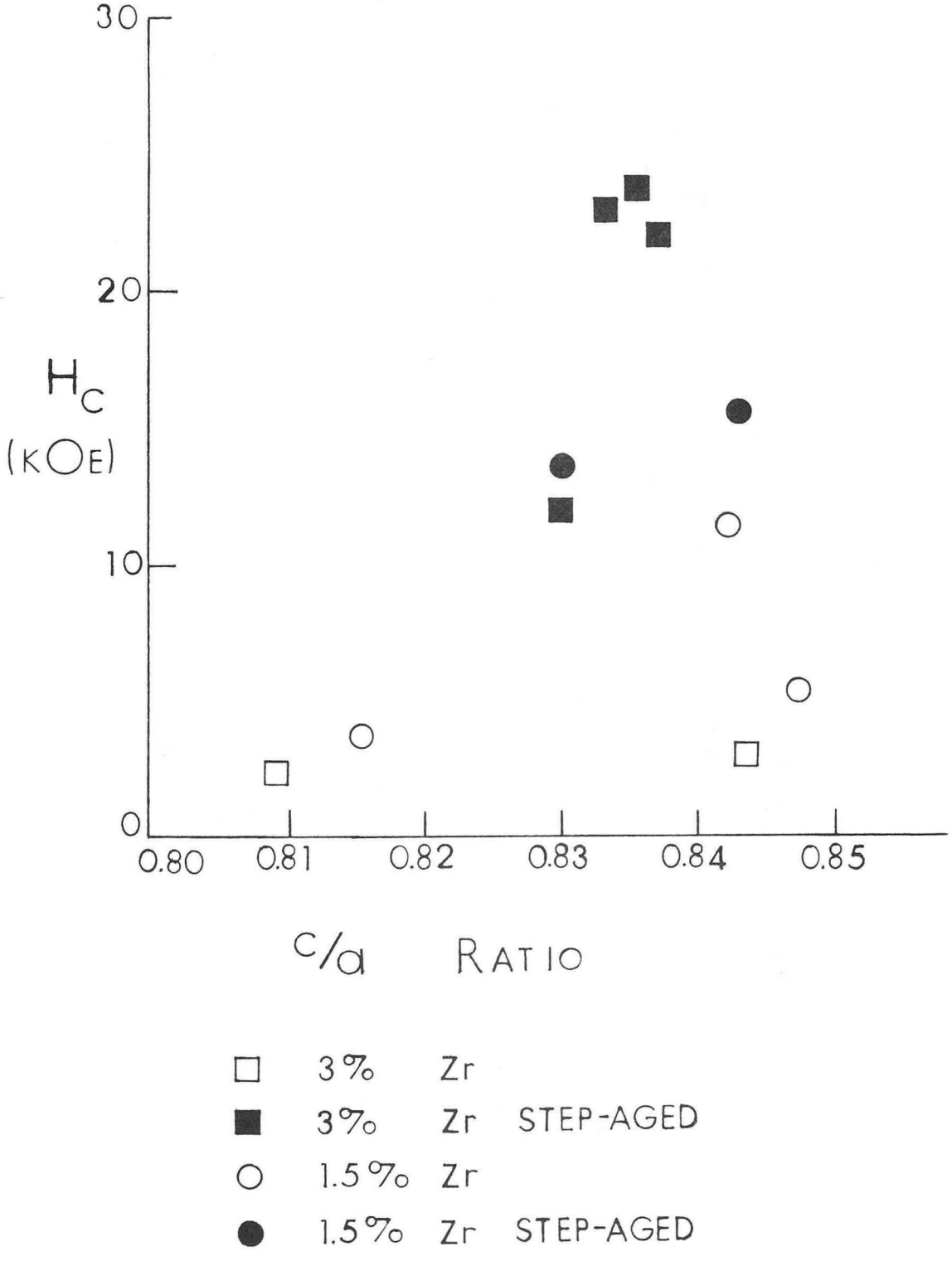

XBL 835-9802

FIGURE 37

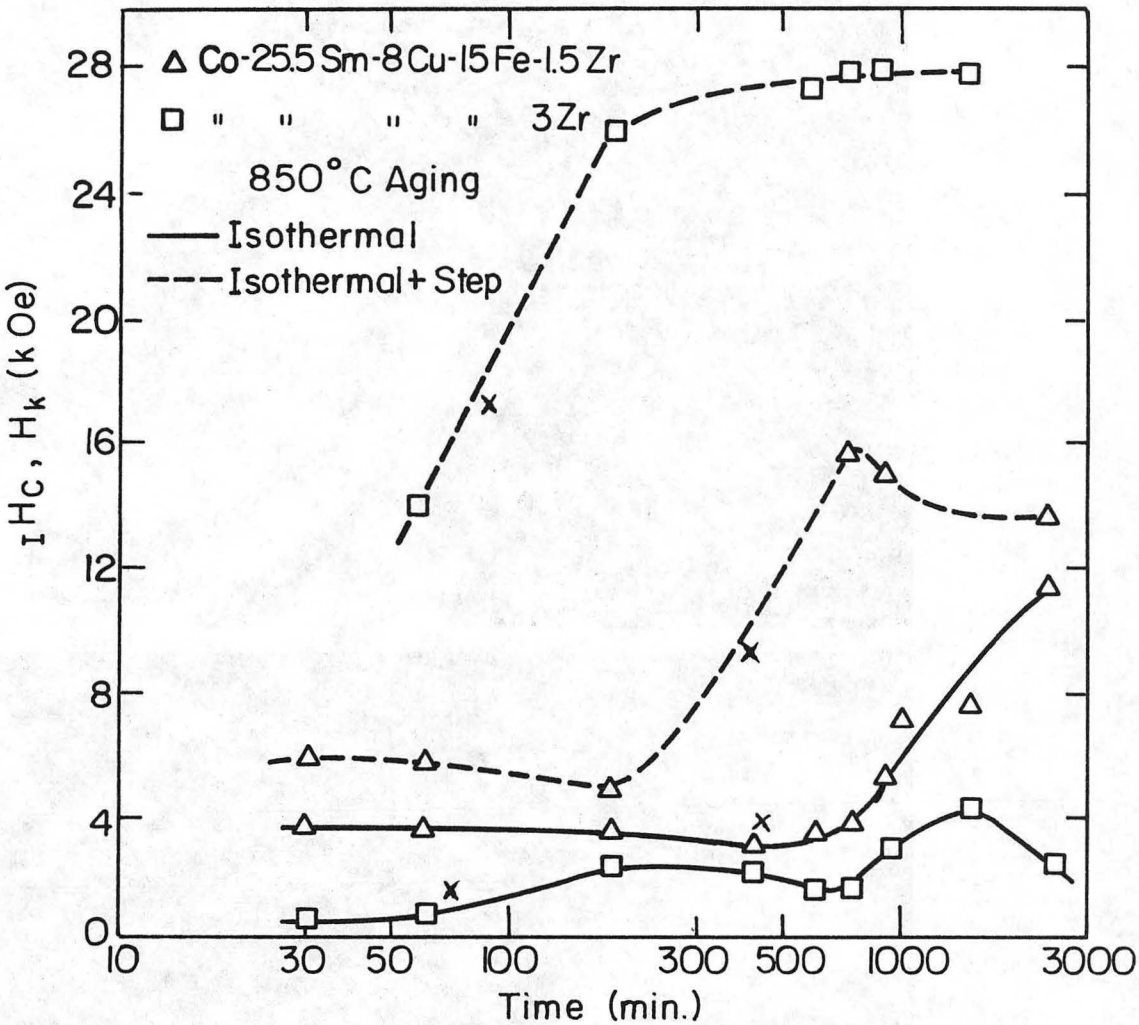

XBL 809-5787

FIGURE 38

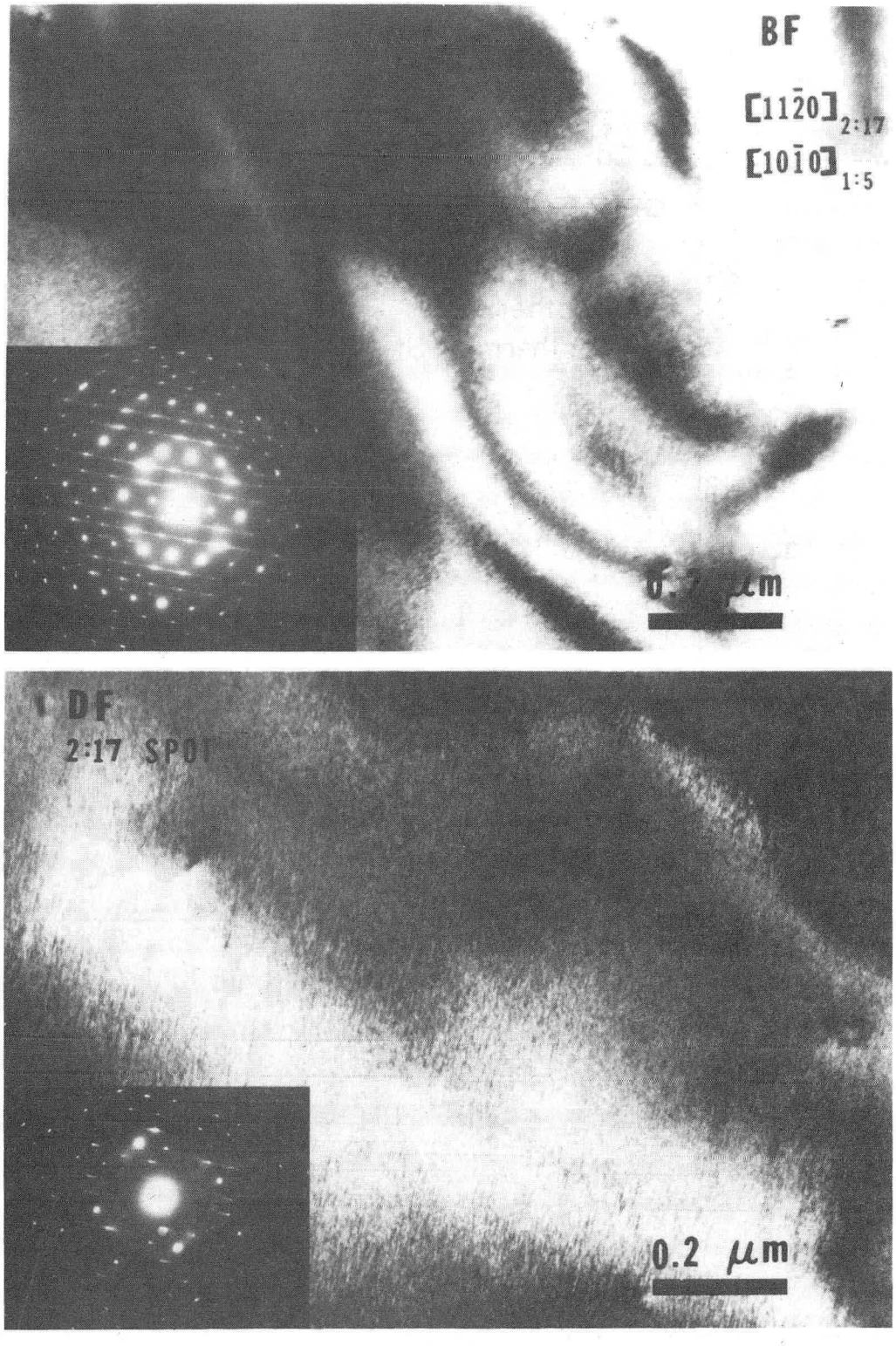

XBB 820-10201

FIGURE 39

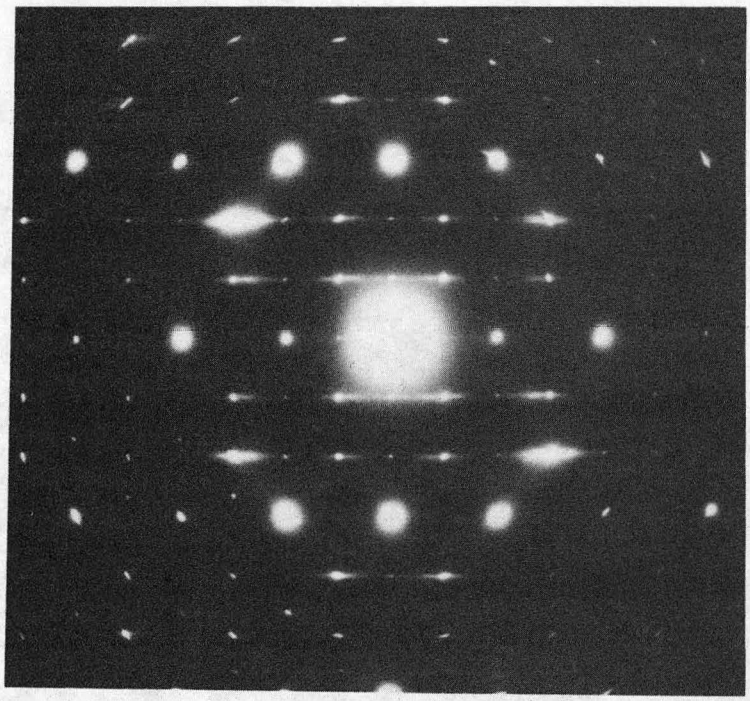

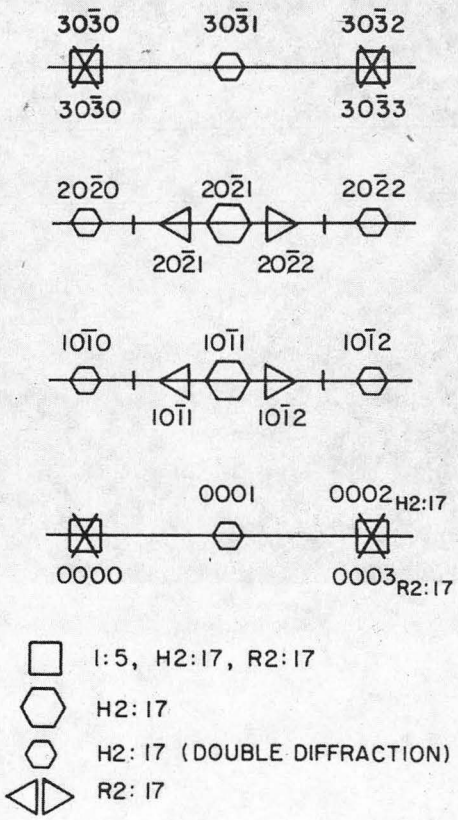

XBB 834-3274

FIGURE 40

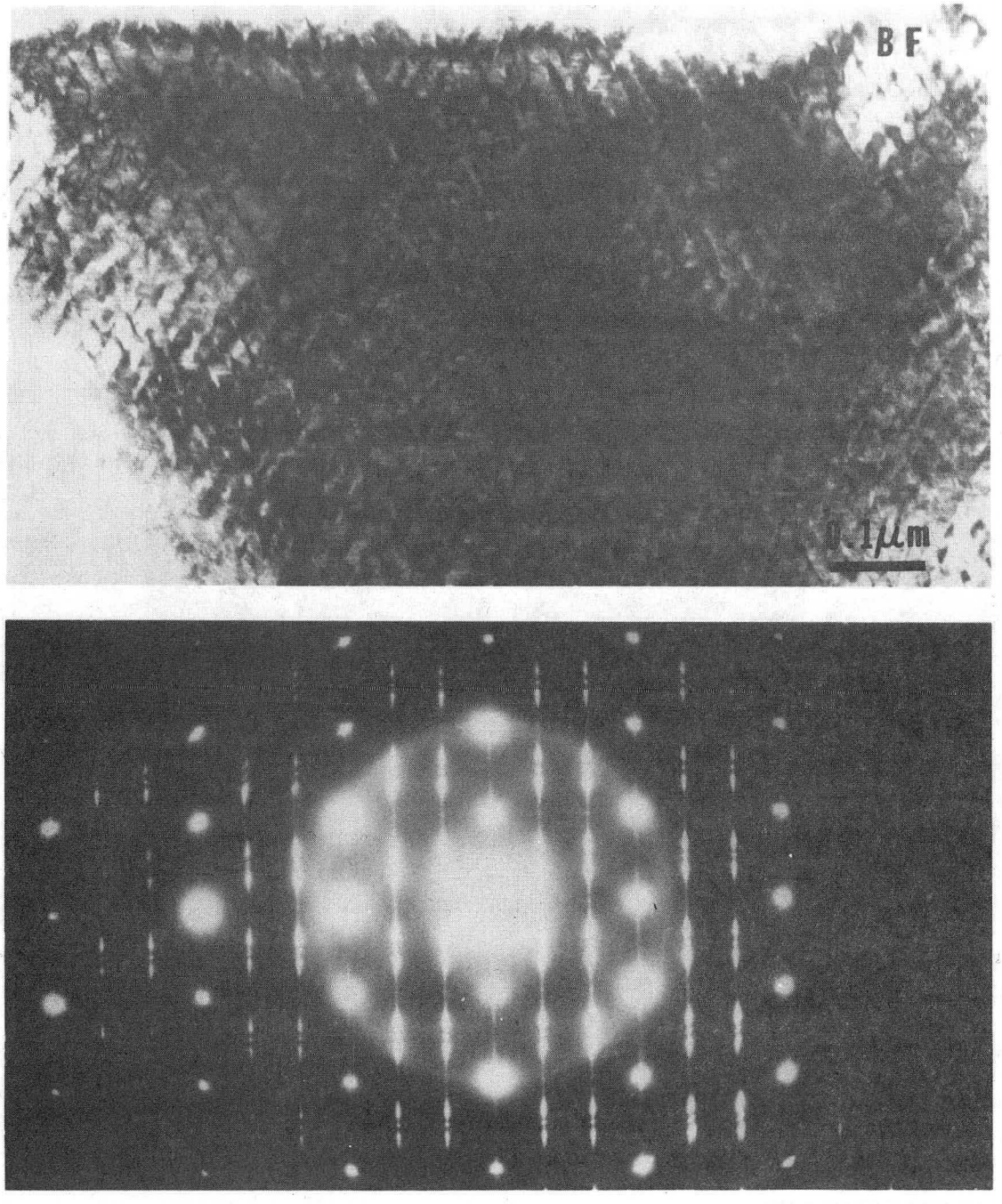

XBB 820-10198

FIGURE 41

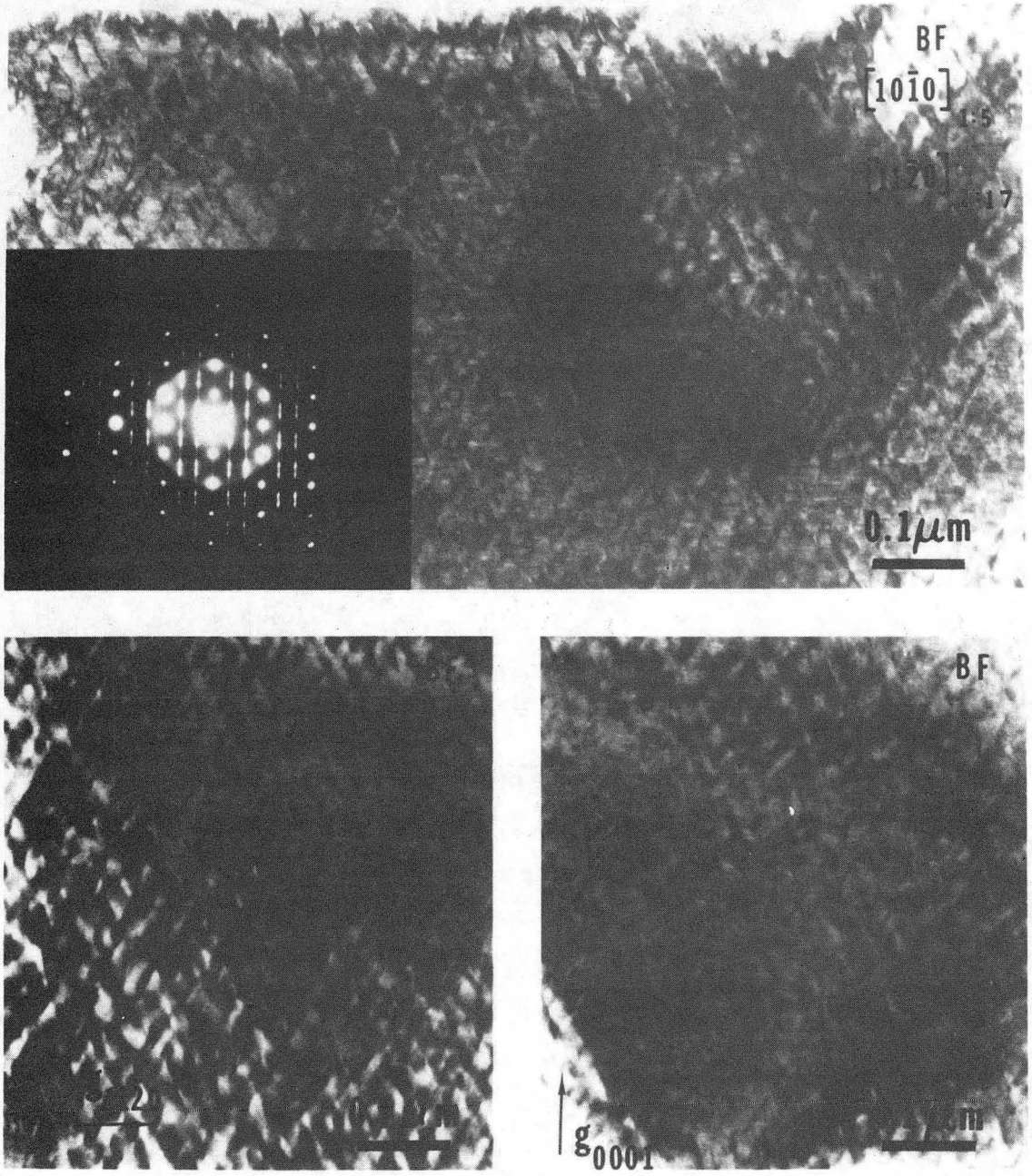

XBB 820-10197

FIGURE 42

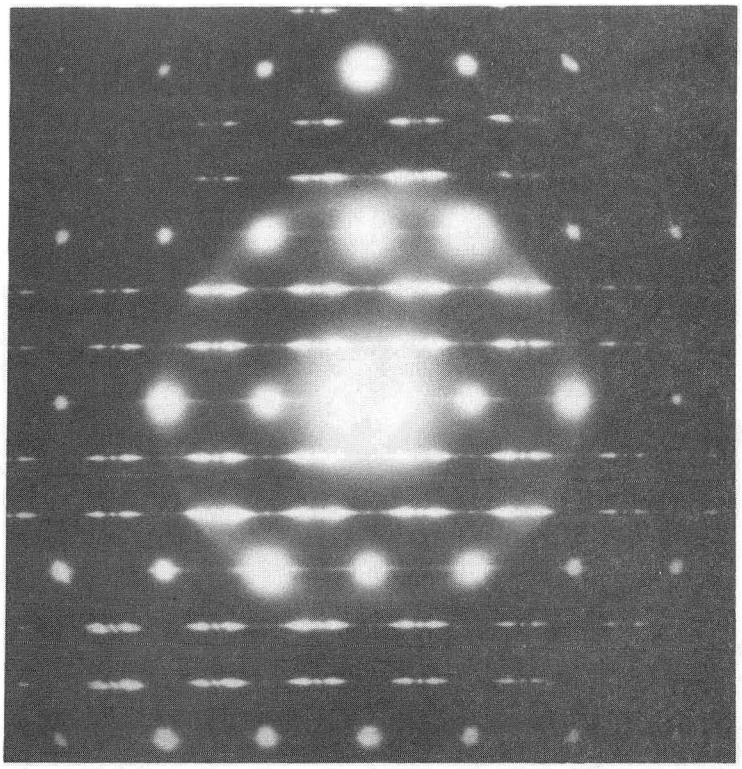

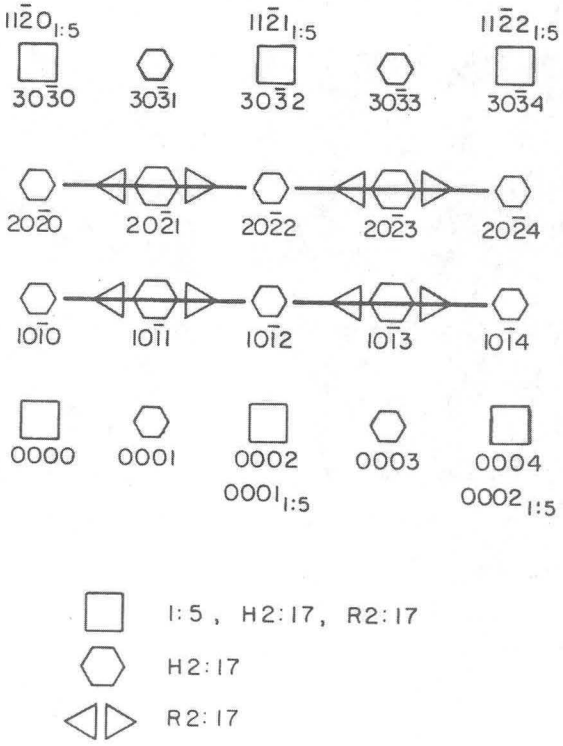

XBB 834-3272

FIGURE 43

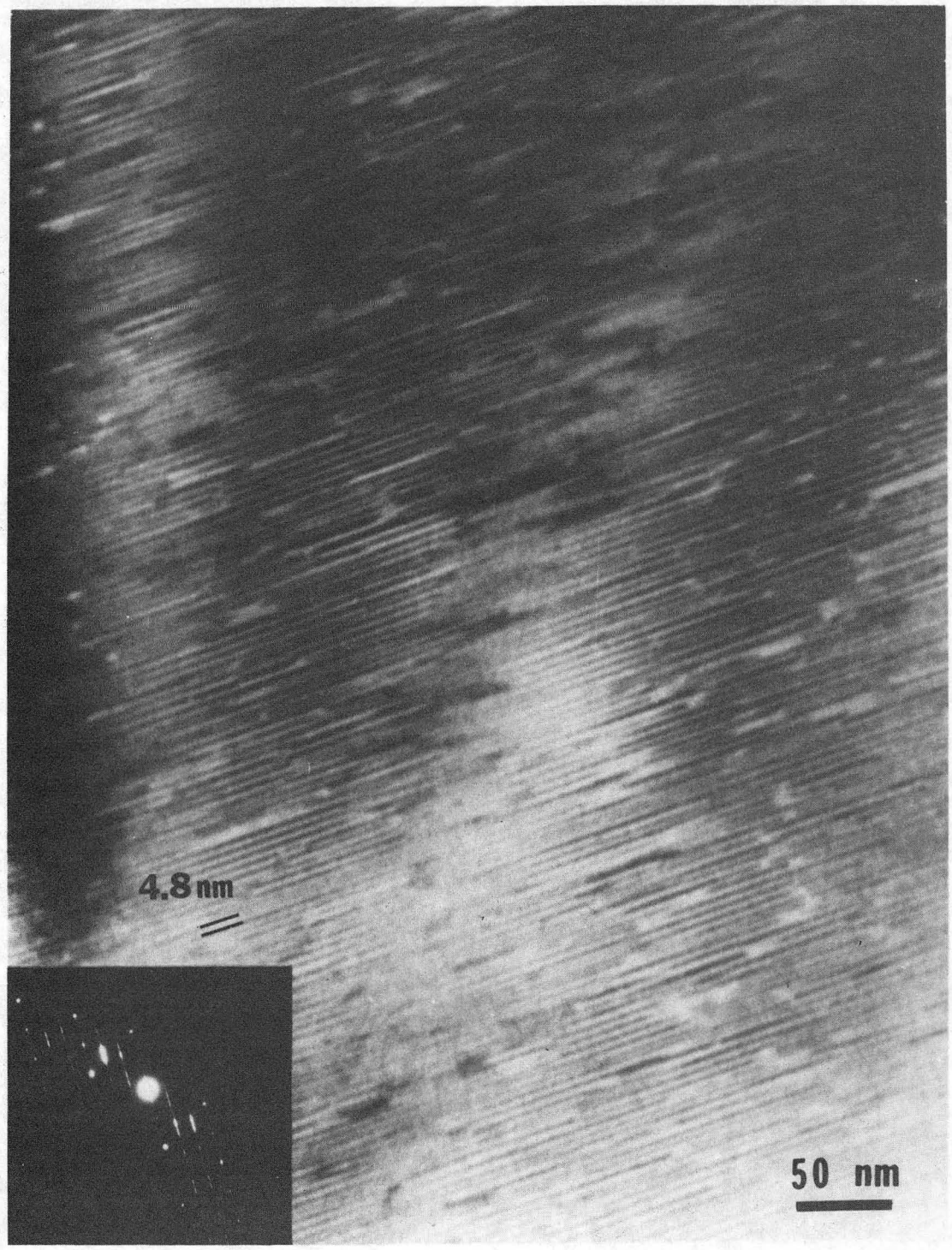

XBB 820-10199

FIGURE 44

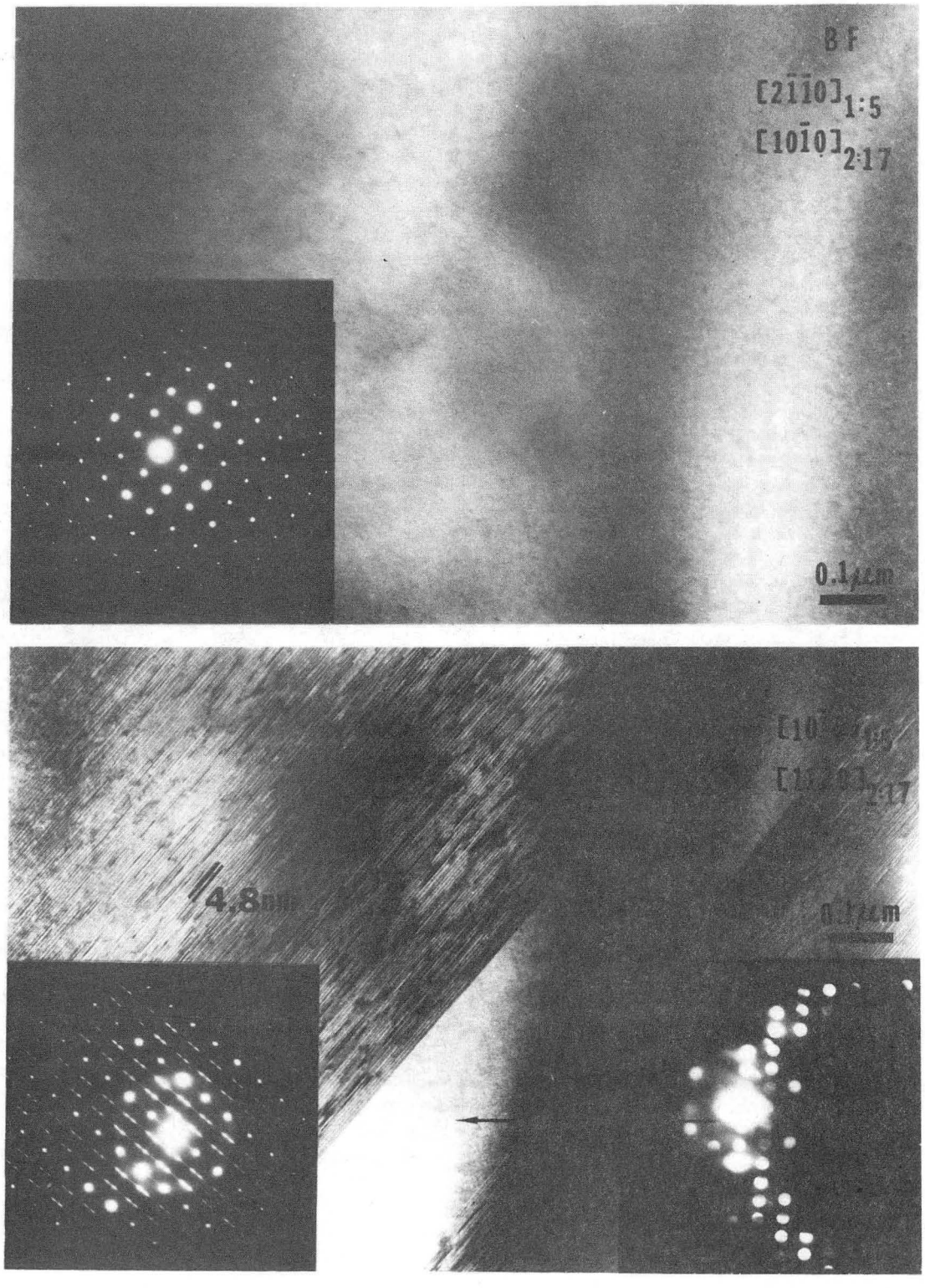

XBB 820-10200

FIGURE 45

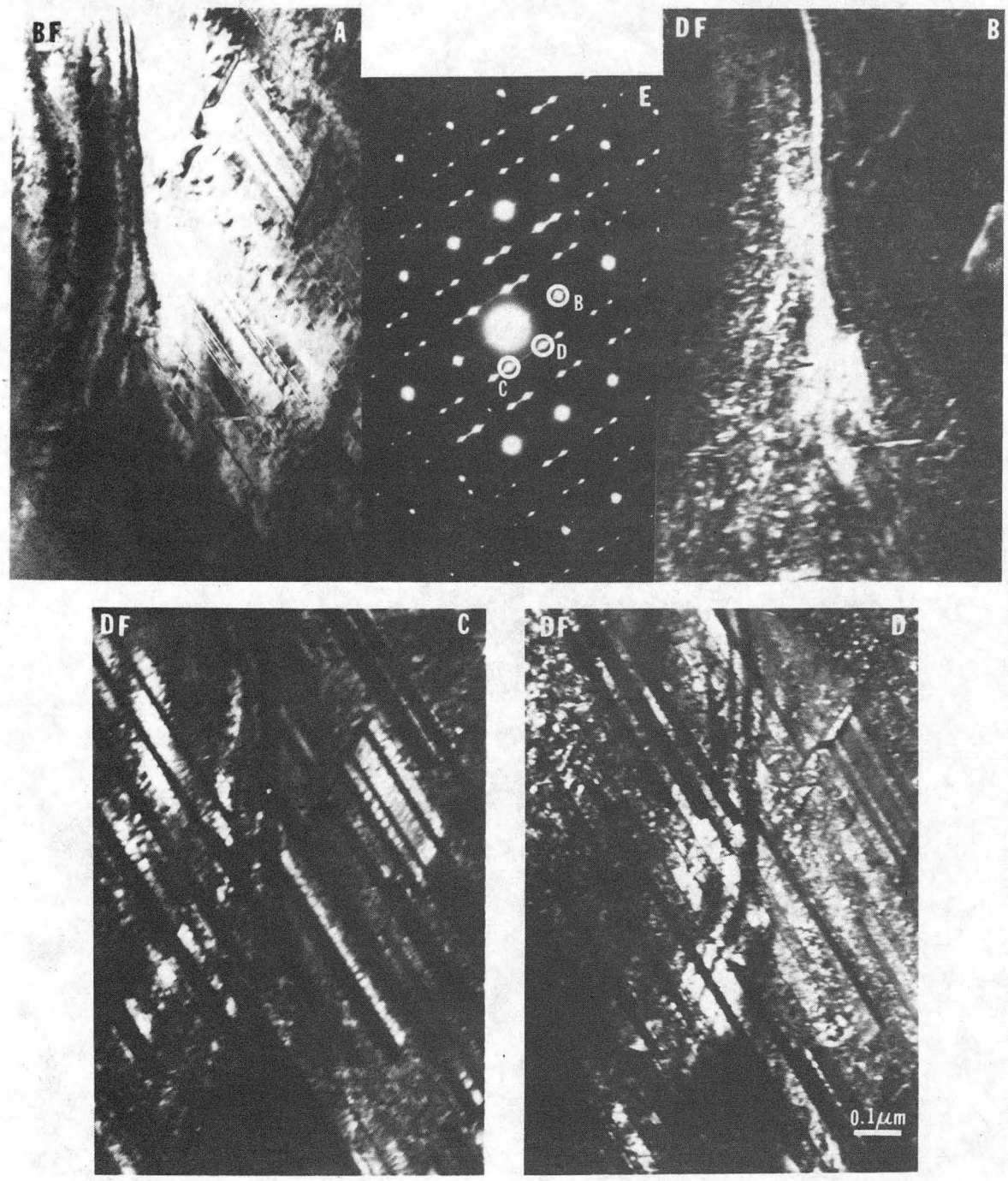

XBB 836-5066

FIGURE 46

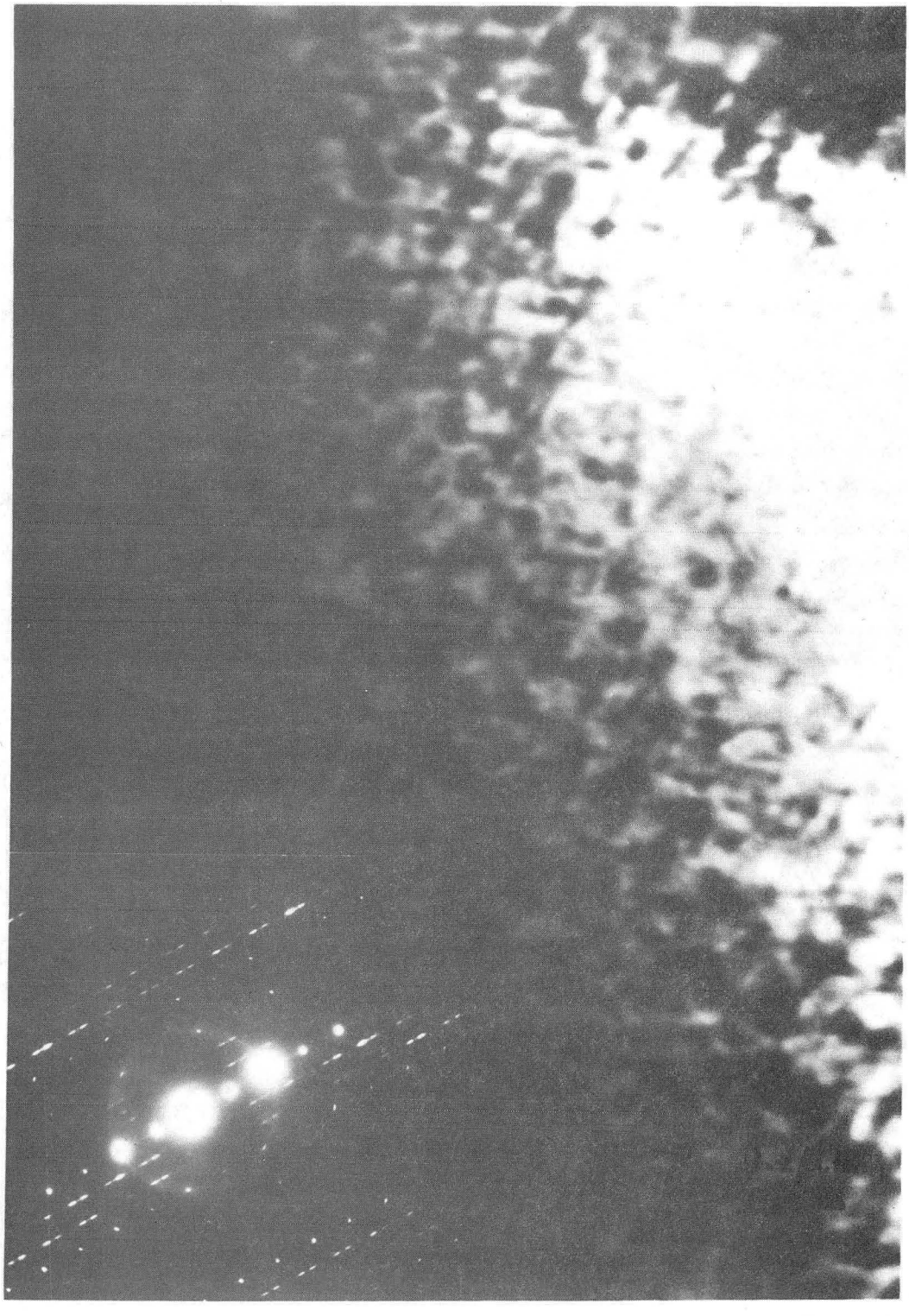

XBB 836-5063

FIGURE 47

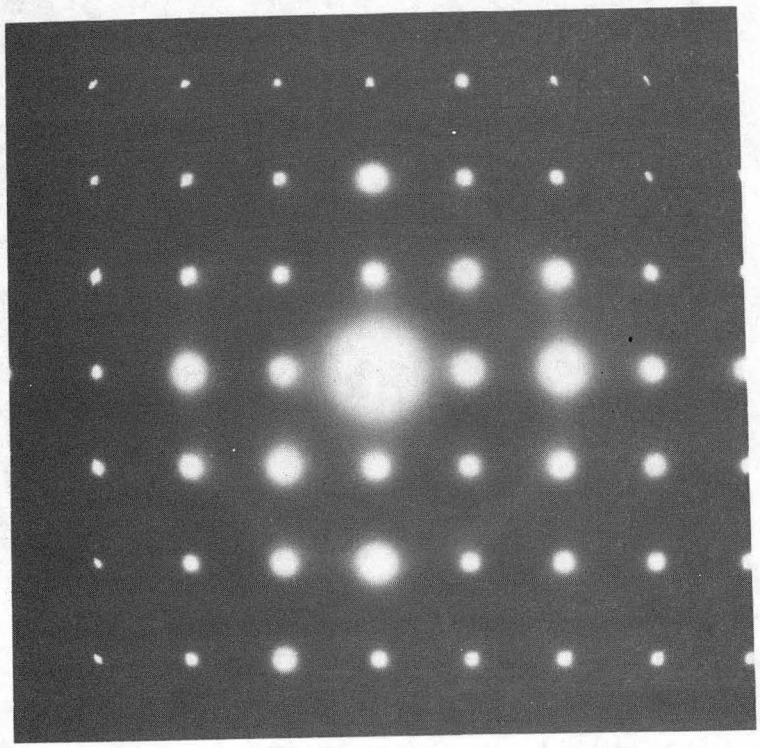

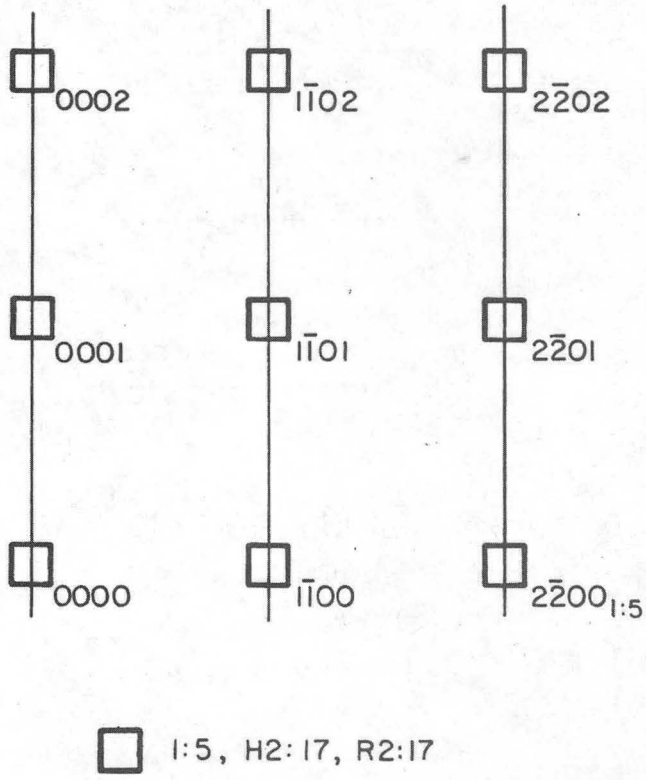

XBB 834-3275

FIGURE 48

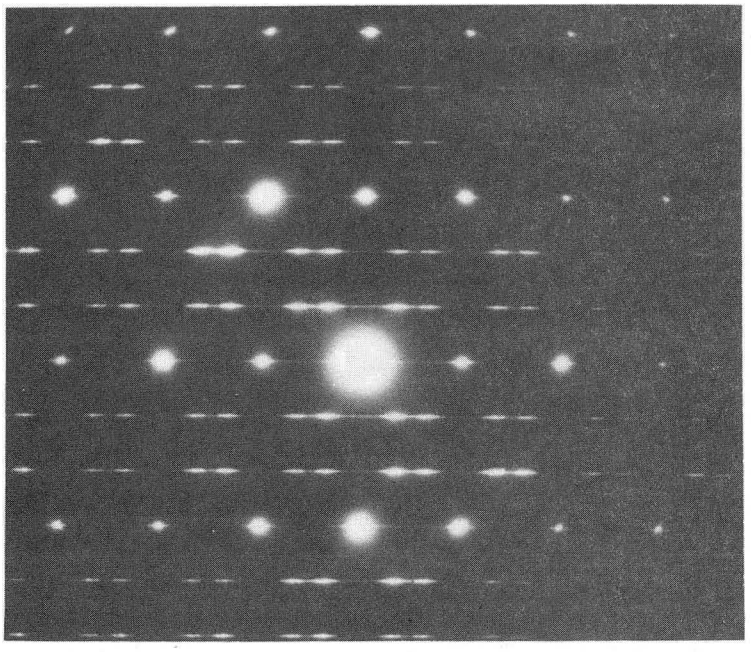

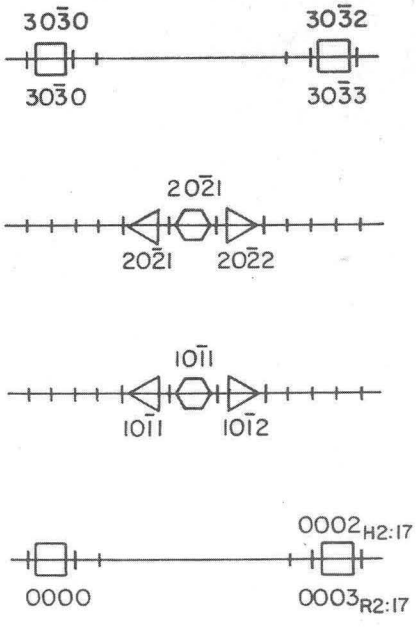

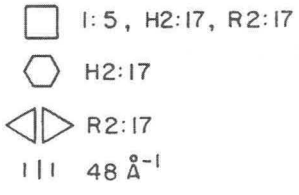

XBB 834-3273

FIGURE 49

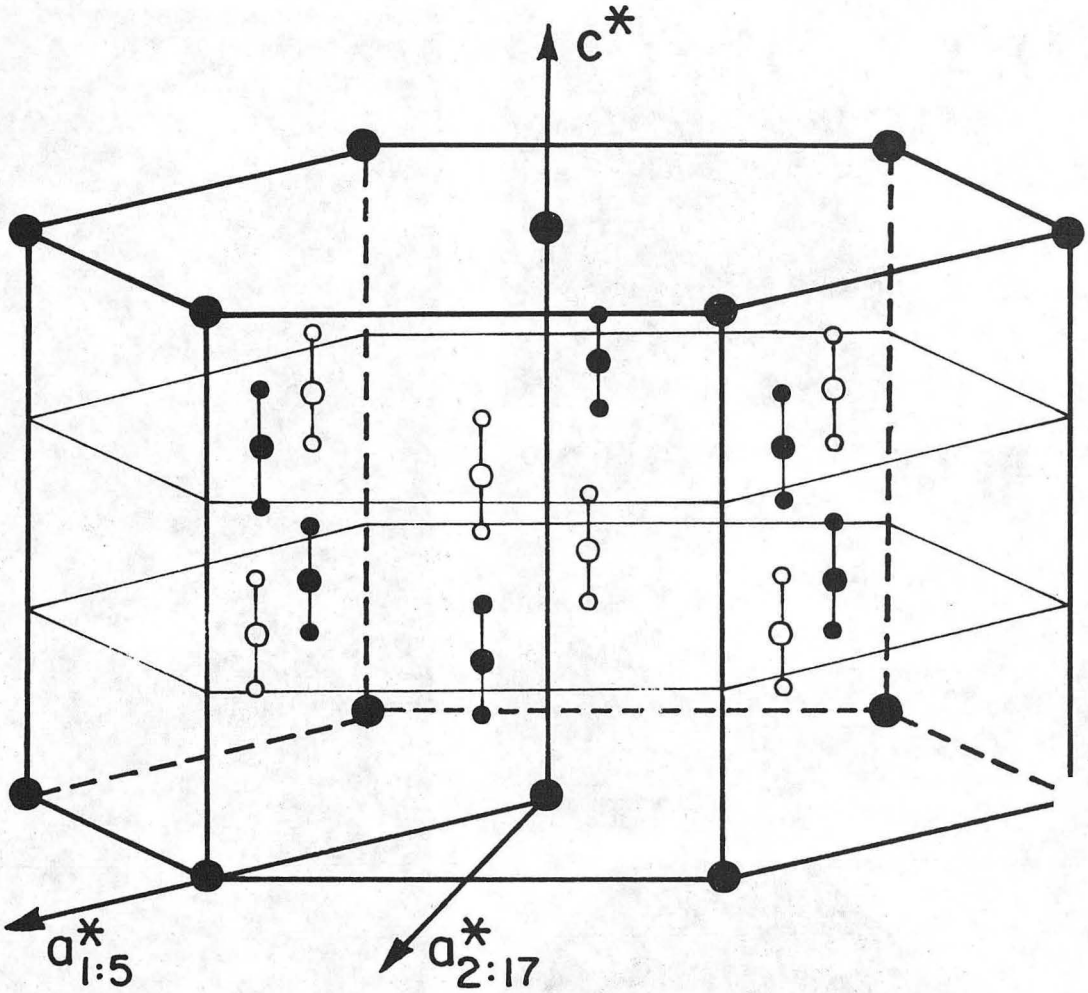

Reciprocal Lattice of Modulated Rhombohedral R_2Co_{17}

● Reflections common to RCo_5 and rhombohedral R_2Co_{17}

○ Reflections and satellites from one R_2Co_{17} variant

● Reflections and satellites from the other R_2Co_{17} variant

XBL 832-5190

FIGURE 50

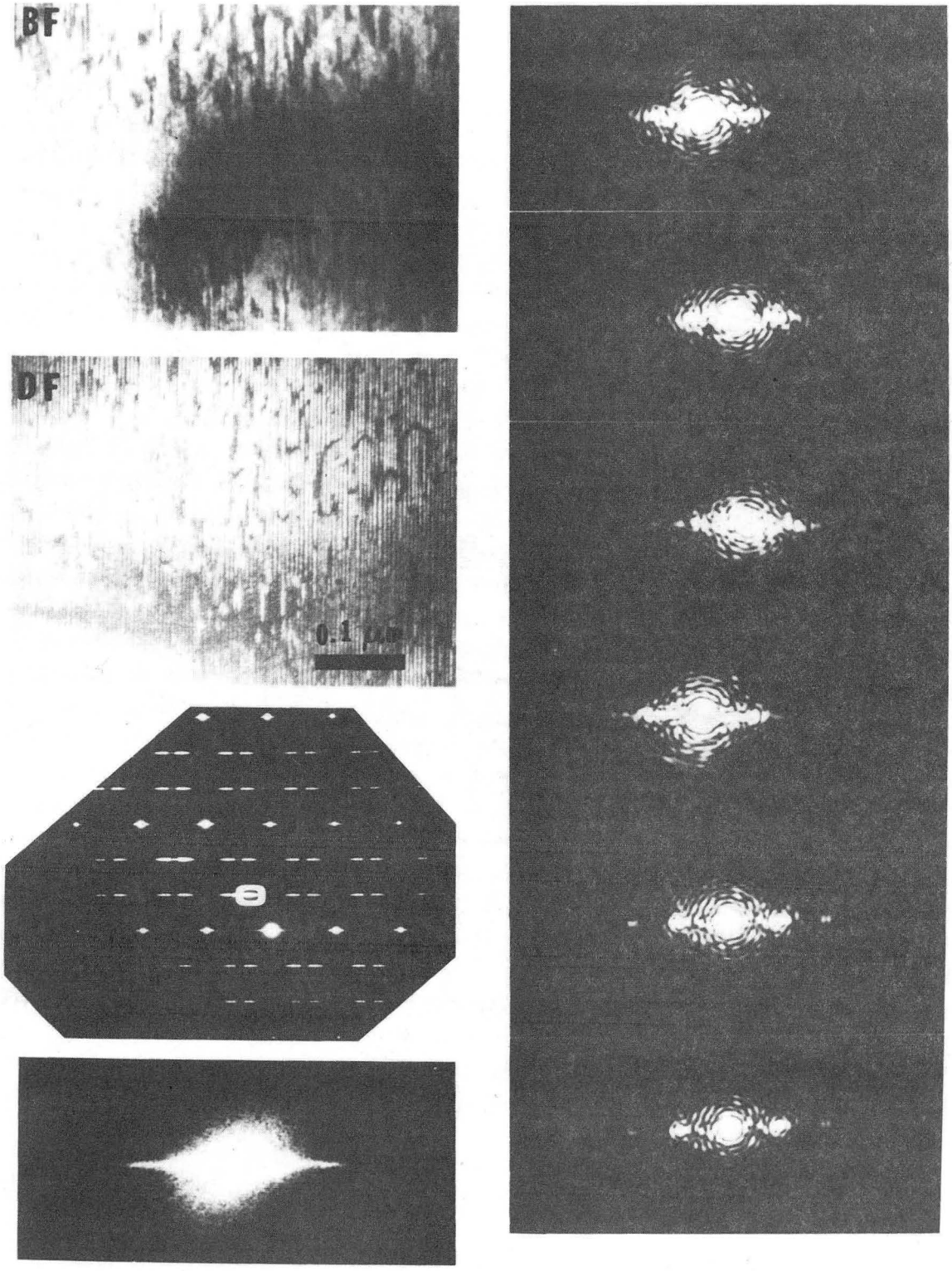

XBB 836-5065

FIGURE 51

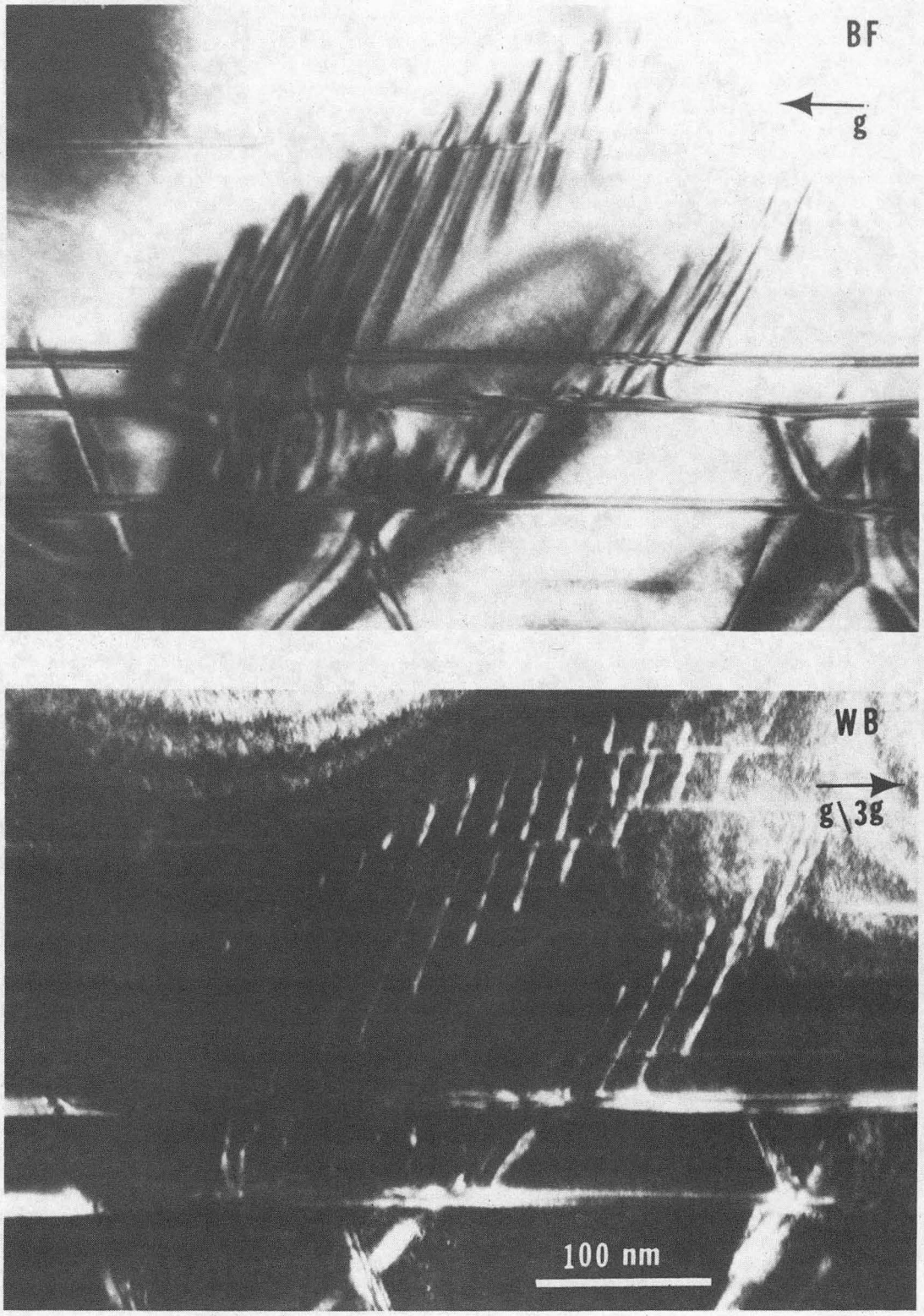

XBB 835-4362

FIGURE 52

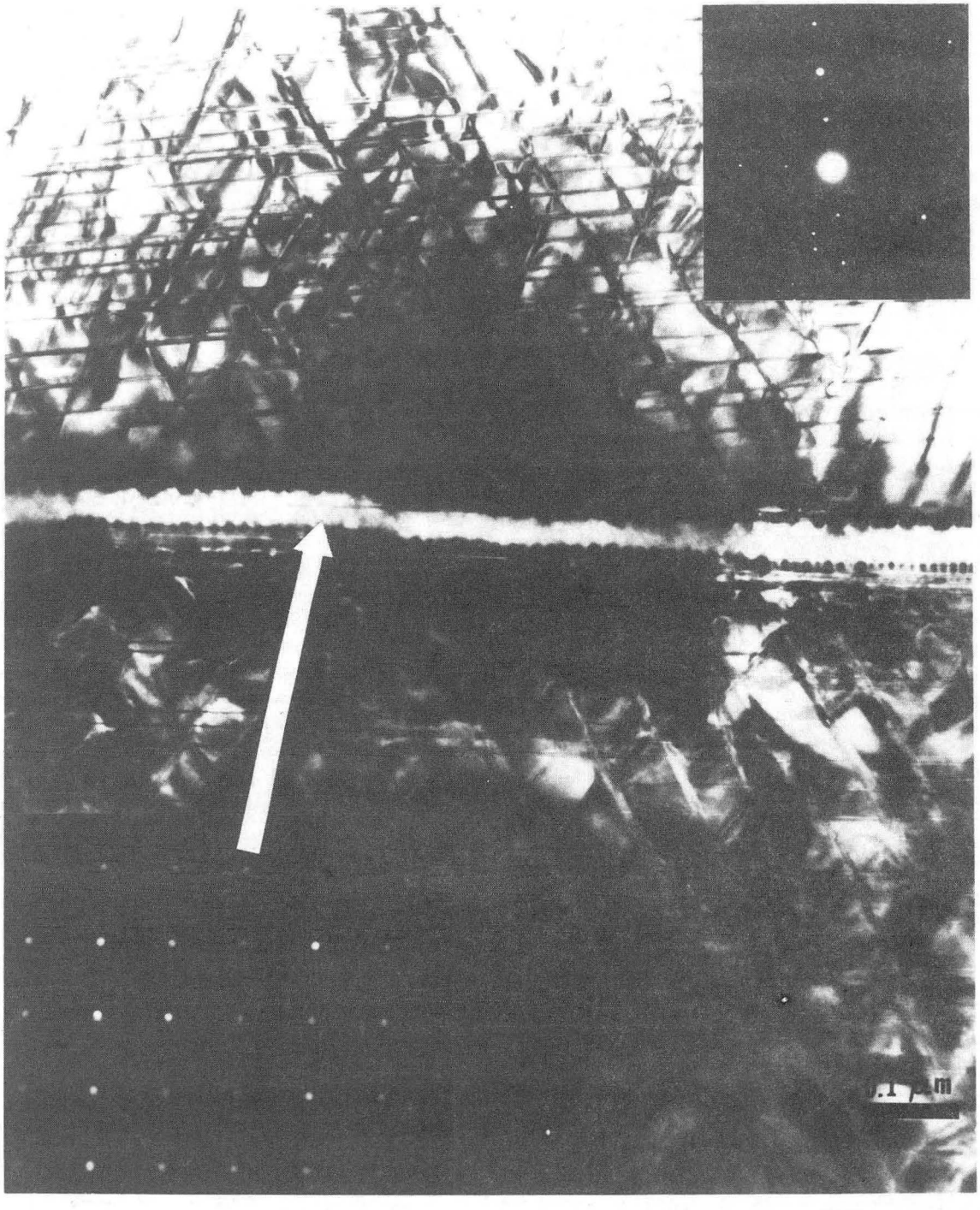

XBB 835-4364

FIGURE 53

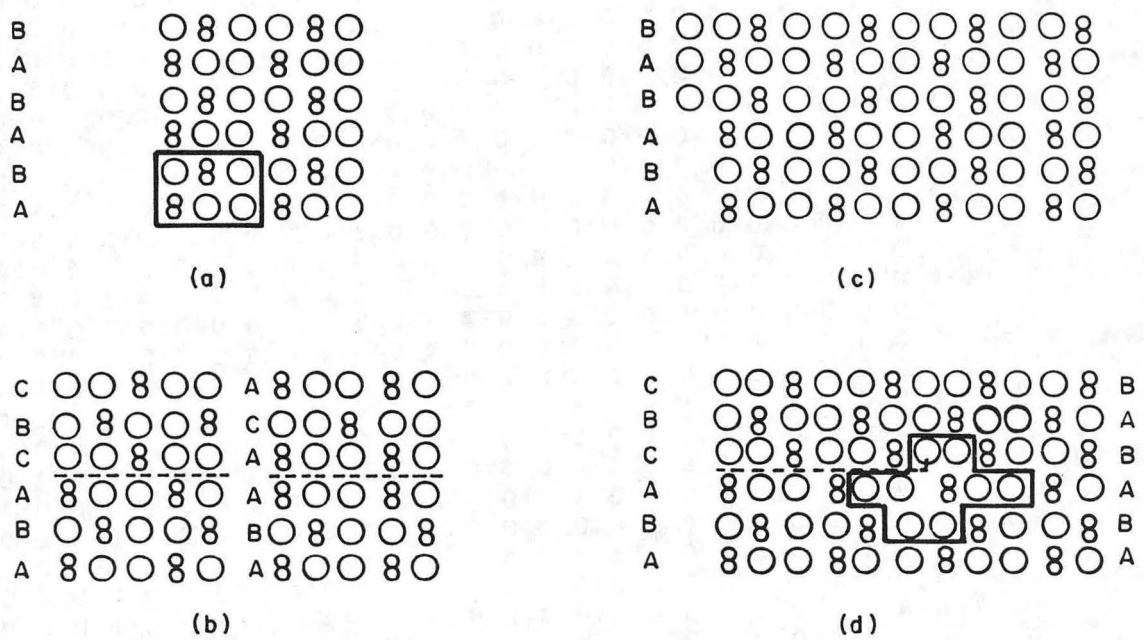

XBL 826-5878

FIGURE 54

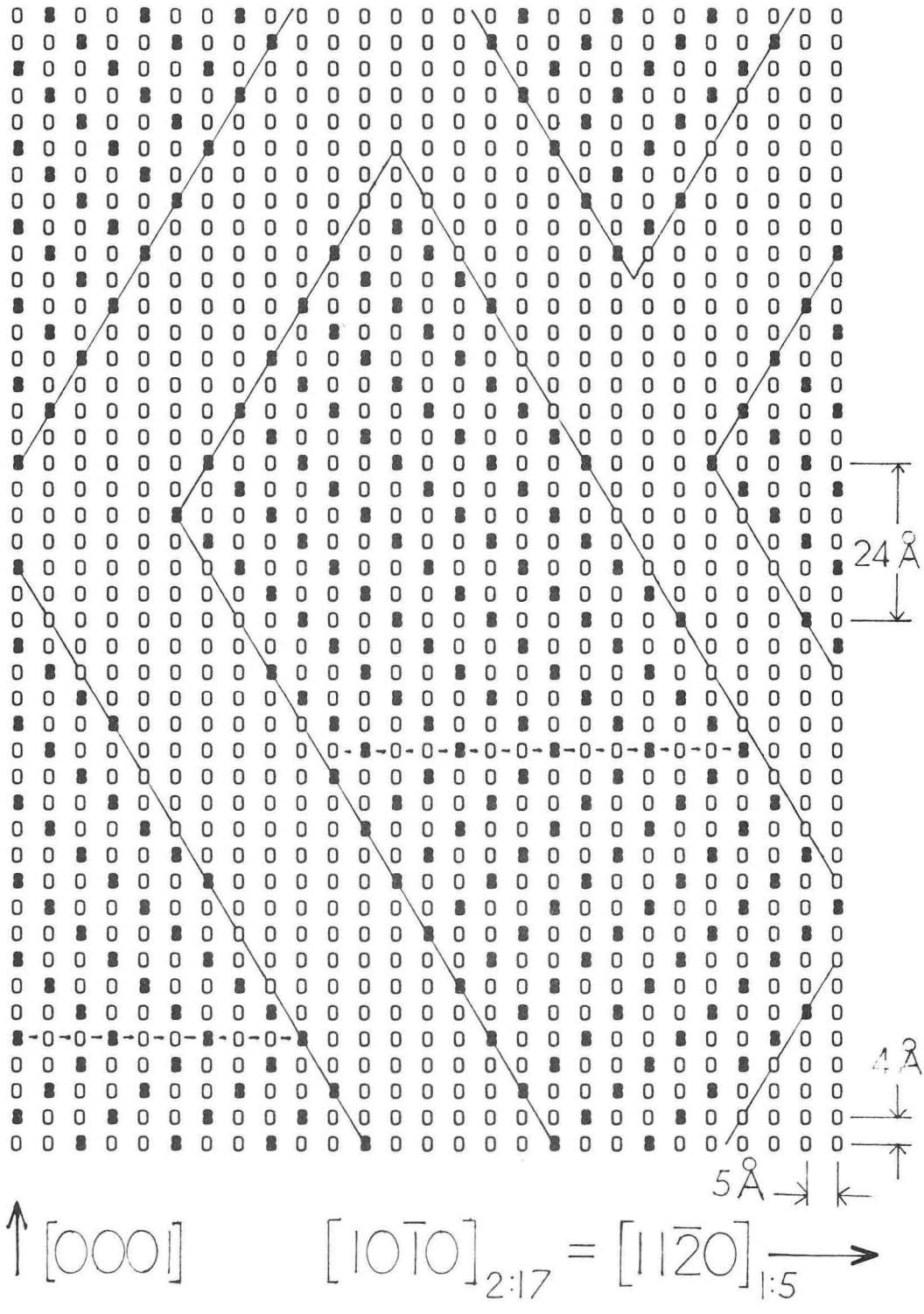

XBL 834-9246

FIGURE 55

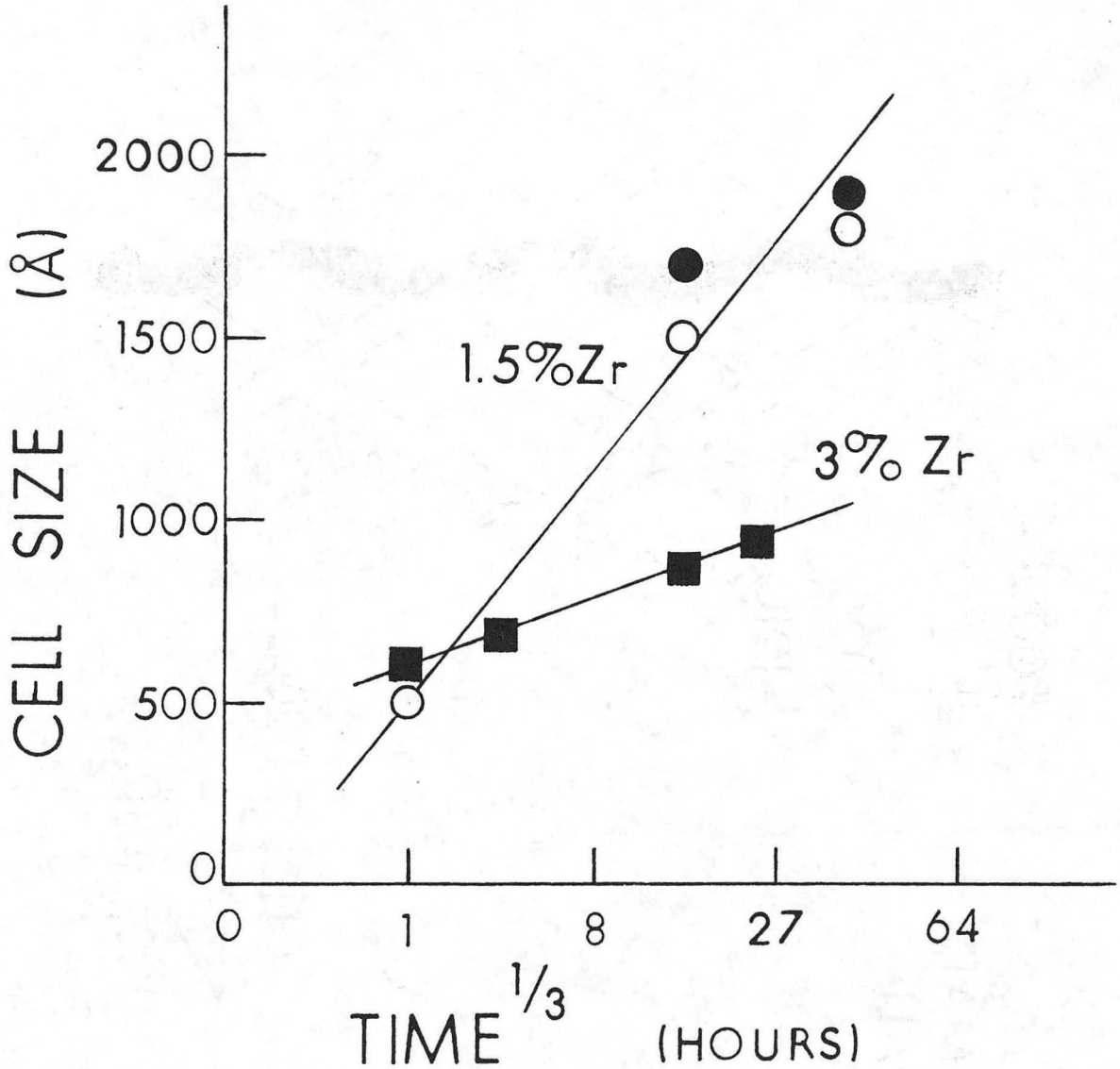

XBL 836-10122

FIGURE 56

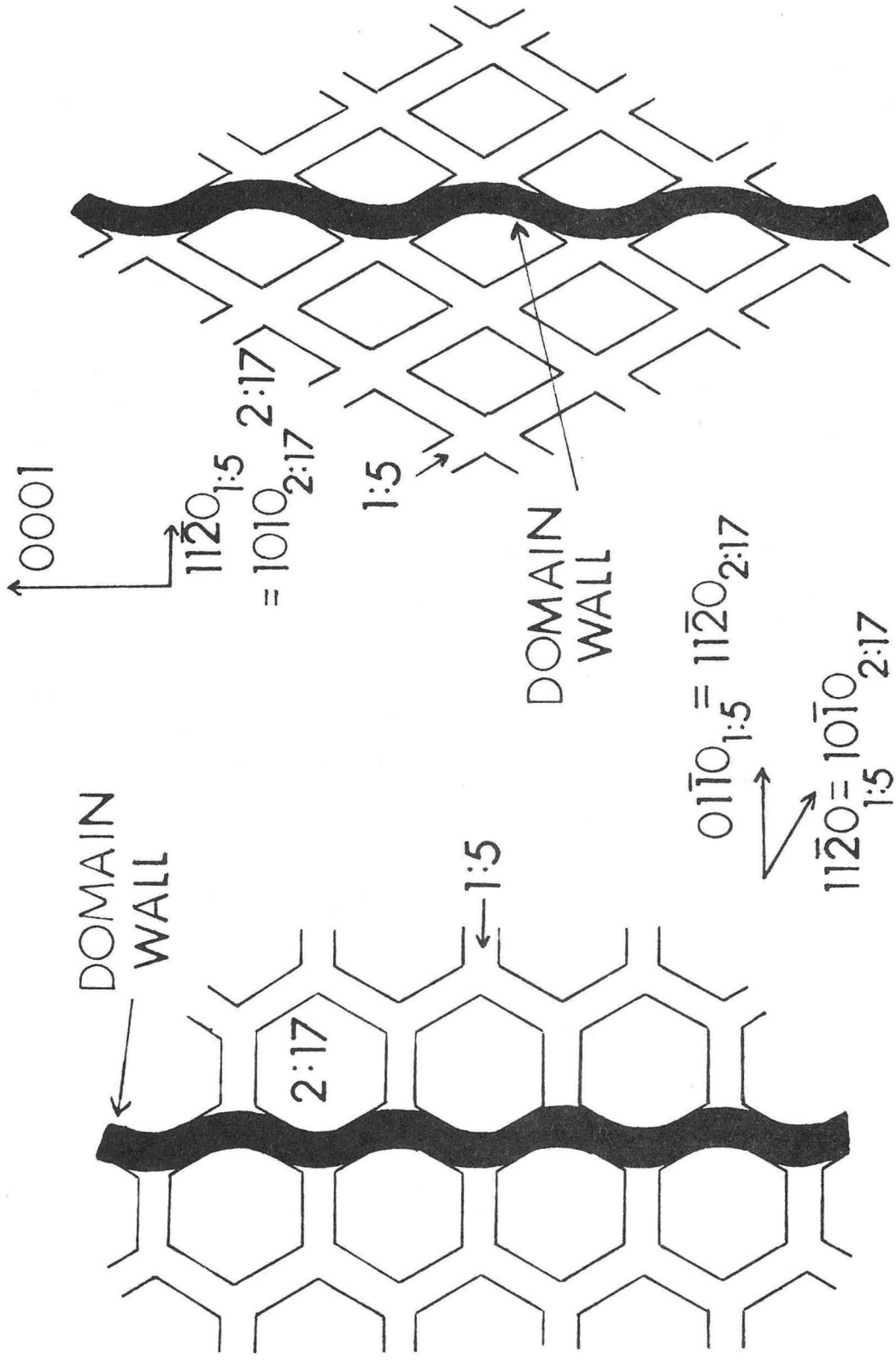

XBL 836-10121

FIGURE 57

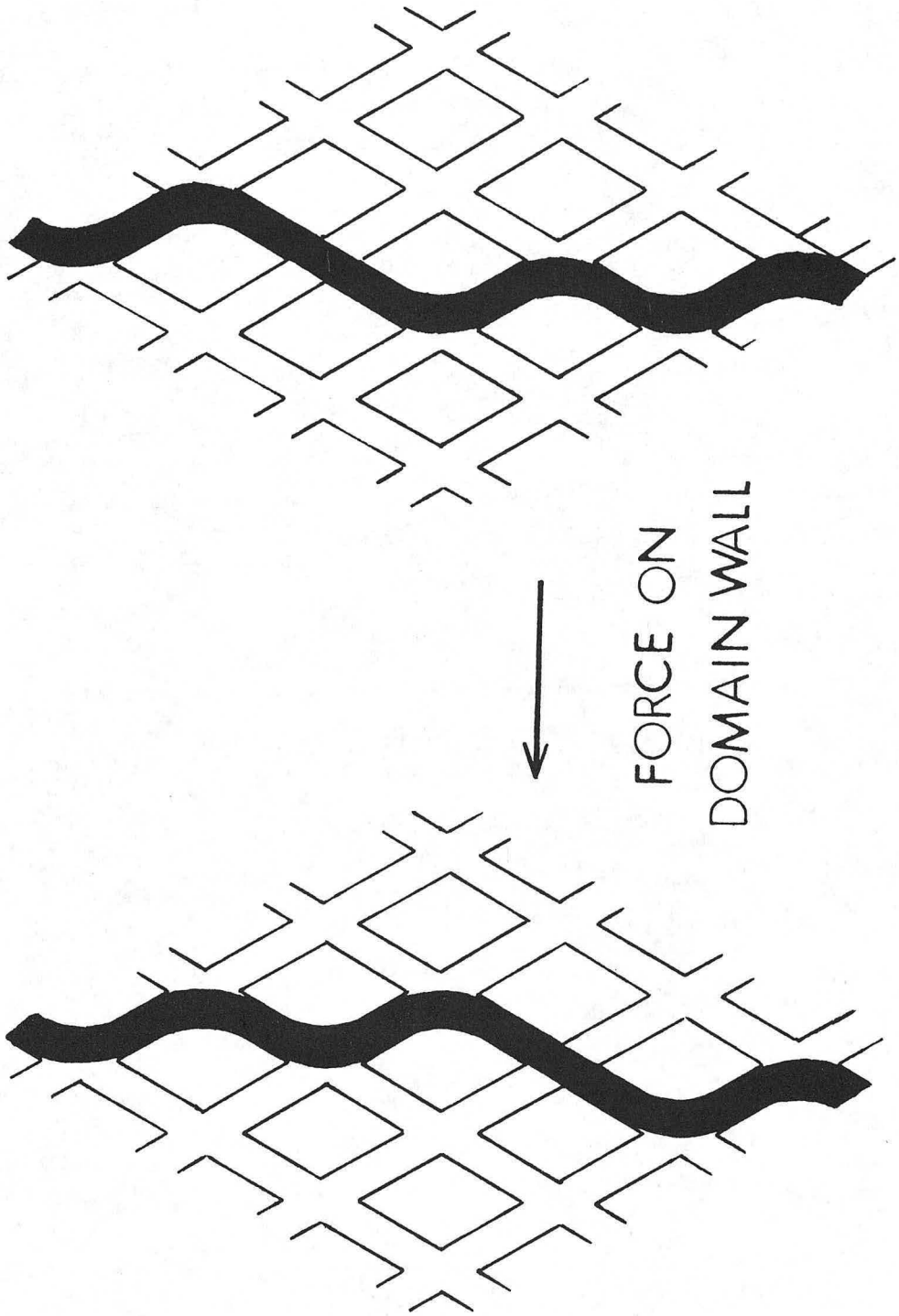

XBL 836-10120

FIGURE 58

This report was done with support from the Department of Energy. Any conclusions or opinions expressed in this report represent solely those of the author(s) and not necessarily those of The Regents of the University of California, the Lawrence Berkeley Laboratory or the Department of Energy.

Reference to a company or product name does not imply approval or recommendation of the product by the University of California or the U.S. Department of Energy to the exclusion of others that may be suitable.

TECHNICAL INFORMATION DEPARTMENT
LAWRENCE BERKELEY LABORATORY
UNIVERSITY OF CALIFORNIA
BERKELEY, CALIFORNIA 94720